Stellar Haloes of Galaxies

Richard D'Souza

München 2016

Stellar Haloes of Galaxies

Richard D'Souza

Dissertation
an der Fakultät für Physik
der Ludwig–Maximilians–Universität
München

vorgelegt von
Richard D'Souza
aus Indien

München, den 19 Februar 2016

Erstgutachter: Guinevere Kauffmann
Zweitgutachter: Hans Böhringer
Tag der mündlichen Prüfung: 21.04.2016

Contents

List of Figures

List of Tables

Zusammenfassung

Im Rahmen der vorliegenden Arbeit werden die durchschnittlichen Eigenschaften stellarer Halos von Galaxien parametrisiert, um die physikalischen Abläufe bei der Bildung von Galaxien zu verstehen und zu modellieren. Durch Stacken von Mosaiken einer großen Zahl von "face-on" Galaxien des Sloan Digital Sky Survey (SDSS) studieren wir die Eigenschaften der stellaren Halos als Funktion der stellaren Masse (MPA-JHU Catalogue), der Halomasse (Yang et al. 2007 Group Catalogue) und der Morphologie.

Anhand von Stacks simulierter Beobachtungen aus den Illustris-Simulationen zeigen wir, dass der äußere Lichtanteil, der aus zweikomponentigen Sérsic-Modell-Fits an die 2-D Oberflächenintensitätsverteilung abgeleitet wird, eine Obergrenze (innerhalb von 0.1 dex) des akkretierten stellaren Massenanteils darstellt. Für die SDSS-Stacks wird gezeigt, dass der äußere Lichtanteil eine Funktion der stellaren Masse und des Galaxientyps ist, und für early-type Galaxien von 30% auf 70% und für late-type Galaxien von 2% auf 25% anwächst. Oberhalb der charakteristischen Masse von $\log M_{halo} \sim 12.5$ ist der äußere Lichtanteil eine stärkere Funktion der Halomasse als der stellaren Masse. Unterhalb der charakteristischen Masse ist der äußere Lichtanteil eine starke Funktion der Konzentration der Galaxie (R_{90}/R_{50}).

Die äußere Steigung des Oberflächenintensitätsverteilung ist ein positive Funktion der Halomasse und Konzentration. Die äußere Elliptizität ist eine positive Funktion der stellaren Galaxienmasse und Konzentration. Die g-r Farben der stellaren Population des Halos sind blauer als die der zentralen Galaxien, und die Farbe der stellaren Halos ist um so röter, je schwerer die Galaxien sind.

Die aus den Beobachtungen abgeleiteten Ergebnisse stimmen gut mit den Illustris-Simulationen oberhalb der charakteristischen Masse überein. Unterhalb der charakteristischen Masse jedoch, wo der akkretierte stellare Massenanteil eine steigende Funktion der stellaren Galaxienmasse ist, können die Simulationen diese Ergebnisse nicht reproduzieren.

Schließlich werden durch die SDSS-Stacks mittlere Flusskorrekturen zu den `Model` Magnituden der SDSS Galaxien hergeleitet. Dies führt zu Korrekturen im Bereich von 0.05 bis 0.35 Magnituden für die Galaxien mit den höchsten stellaren Massen. Diese Korrekturen werden für ein vollständiges Set von 500000 SDSS-Galaxien auf die MPA-JHU stellaren Massen angewandt, um eine korrigierte stellare Galaxienmassenfunktion bei $z = 0.1$ im stellaren Massenbereich $9.5 < \log(M_*/M_\odot) < 12.0$ herzuleiten. Die Flusskorrekturen und die Verwendung der MPA-JHU stellaren Massen haben signifikante Auswirkung im hohen Massenbereich der stellaren Massenfunktion, was zu einer signifikant flacheren Steigung

führt als die von Li & White (2009) hergeleitete, aber zu einer steileren Steigung als die von Bernardi et al. (2013) hergeleitete. Dies entspricht einer mittleren mitbewegten stellaren Massendichte von Galaxien mit stellaren Massen $\log(M_*/M_\odot) \geq 11.0$, was ein Faktor 3.36 höher ist als die Abschätzung von Li & White (2009), aber um 43% geringer als die Abschätzung von Bernardi et al. (2013).

Summary

In this thesis, we observationally parametrize the average properties of the stellar haloes of galaxies in order to constrain the physics of galaxy formation. By stacking aligned mosaics of a large number of face-on central galaxies from the Sloan Digital Sky Survey (SDSS), we study the properties of the stellar haloes of galaxies as a function of stellar mass (from MPA-JHU catalogue), halo mass (from Yang et al. 2007 group catalogue) and morphology.

Using stacks of mock images of galaxies from the Illustris simulations, we show that the outer light fraction derived from fitting double Sérsic models to the 2-D surface brightness distribution of galaxy stacks provides an upper limit (within 0.1 dex) of the mean accreted stellar mass fraction. For the SDSS stacks, we find that the outer light fraction is a function of stellar mass and galaxy type, increasing from 30% to 70% and from 2% to 25% for early and late type galaxies respectively over the mass range between $10^{10.0} M_\odot$ to $10^{11.4} M_\odot$. Above the characteristic mass ($\log M_{halo} \sim 12.5$), we find that the outer light fraction is a stronger function of halo mass than stellar mass. Below the characteristic mass, the outer light fraction is a strong function of a galaxy concentration (R_{90}/R_{50}).

We further parametrize the surface brightness distribution of the stellar halo of the galaxy stack by estimating its outer slope and ellipticity. We find that the outer slope is an increasing function of halo mass and concentration, while the outer ellipticity is a increasing function of stellar mass and concentration. The g-r colour of the stellar population in the stellar halo is bluer than in the main galaxy, and the colour of the stellar halo is redder for higher mass galaxies.

We find that our observational constraints agree well with the Illustris simulations above the characteristic mass. However, the simulations fail to reproduce the data below the characteristic mass where the accreted mass fraction is an increasing function of stellar mass.

Using our SDSS stacks, we derive average flux corrections to the SDSS `Model` magnitudes, finding corrections ranging from 0.05 to 0.32 mag for the highest stellar mass galaxies. We apply these corrections to the MPA-JHU stellar masses for a complete sample of half a million galaxies from the SDSS survey to derive a corrected galaxy stellar mass function at $z = 0.1$ in the stellar mass range $9.5 < \log(M_*/M_\odot) < 12.0$. We find that the flux corrections and the use of the MPA-JHU stellar masses have a significant impact on the massive end of the stellar mass function, making the slope significantly shallower than that estimated by Li & White (2009), but steeper than derived by Bernardi et al. (2013). This corresponds to a mean comoving stellar mass density of galaxies with stellar masses

$\log(M_*/M_\odot) \geq 11.0$ that is a factor of 3.36 larger than the estimate by Li & White (2009), but is 43% smaller than reported by Bernardi et al. (2013).

Chapter 1

Introduction

Deep observations of the night sky reveals many surprises. Most notable of them is that galaxies have a diffuse luminous outer component which extends far beyond their conventional visible boundaries. The first deep observations made in the 80s using photographic plates (Schweizer, 1980; Malin & Carter, 1983) revealed that nearby massive galaxies contained a number of shell-like structures and stellar streams. While these low surface brightness (LSB) features were subsequently observed in a handful of nearby galaxies, it was the uniformity and linear response of the new charge-coupled devices (CCDs) detectors that allowed one to observe streams around all types of galaxies (Martinez-Delgado et al., 2010; Duc et al., 2015). These outer low surface brightness features around galaxies make up its stellar halo and is the main subject of this thesis.

Stellar haloes are conventionally defined as the extremely faint outer luminous component of the galaxy, extending out to nearly 100-200 kpc around a typical Milky Way size galaxy. Despite containing only a tiny fraction of the total light of the galaxy (1-15%), they are arguably the component that contains the most useful information about the evolutionary history of a galaxy. This is because stars in the halo provide a fossil record of the assembly history of the galaxy through their chemical abundances and motions. The stars in the stellar haloes retain in their atmospheres a record of the chemical elements of the environment in which they were born. Additionally, the long relaxation time of stars in the halo allows them to retain some record of their origins in phase-space. In 1962, Eggen, Lynden-Bell & Sandage in their seminal work on the stellar halo of our Galaxy wrote: *"It is now recognized that a study of these subsystems allows us partially to reconstruct the Galactic past because the time required for stars in the Galactic system to exchange their energies and momenta is very long compared with the age of the Galaxy. Hence knowledge of the present energy and momenta of individual objects tells us something of the initial dynamic conditions under which they were formed."* (Eggen, Lynden-Bell & Sandage, 1962)

1.1   Testing Theories of Galaxy Formation

Observational constraints on stellar haloes can be used to test theories of galaxy formation and evolution. Eggen, Lynden-Bell & Sandage (1962) analyzed the properties and motion of 221 dwarf stars in the vicinity of the Sun and showed that those with lower metallicity (measured through an ultra-violet excess) tend to move on more highly eccentric orbits. They interpreted these observational trends as a signature of the formation of lower metallicity stars during a rapid radial collapse, which later proceeded to form the stellar disk. A decade later, Searle & Zinn (1978) measured for the first time the metallicities in a sample of globular clusters and found no significant abundance gradient as a function of the galactocentric distance, which would be expected from a collapsing model. These observations led Searle & Zinn to formulate the hypothesis that the stellar halo formed over a longer time-scale through the agglomeration of many subgalactic fragments that may be similar to the surviving dwarf spheroidal galaxies today observed as satellites of the Milky Way. Over the years, the Searle & Zinn picture has grown in currency as more and more observations pointed to the lumpy build up of the Galaxy in the form of clumps of stars in phase space (Rodgers et al., 1981; Rodgers & Paltoglou, 1984; Ratnatunga & Freeman, 1985; Sommer-Larsen & Christensen, 1987; Doinidis & Beers, 1989; Arnold & Gilmore, 1992; Preston et al. , 1994; Majewski et al., 1994, 1996; Ibata et al., 1994).

The Searle & Zinn picture resembles more closely the current theories of structure formation in the universe, and provides a direct link between cold dark matter (CDM) cosmology and the hierarchical formation of the stellar halo of the galaxy (Johnston et al., 1995; Helmi & White, 1999; Bullock et al., 2001). In this picture, the stellar halo of a galaxy is built up through the accretion of satellites over its cosmic history. This follows from the theory of heirarichal structure and galaxy formation (White & Rees, 1978; Frenk & White, 1991): dark matter haloes form first through hierarchical clustering, where smaller structures coalesce to form larger ones; the luminous content of galaxies then results from cooling and condensation of gas within the potential well provided by these dark matter haloes. Within such a framework, stars form only in the collapsed, high-density regions near the center of dark matter haloes by the cooling and condensation of gas. On the other hand, stars found at large galactocentric distances (> 30 kpc) have been accreted from proto-galaxies during the merger events that characterized the assembly of galaxies in a hierarchically clustering universe. These outer halo stars originate in satellites whose orbital apocentre was about that large before they spiraled in and merged with the main galaxy. Following Abadi et al. (2006), we call stars formed within the galaxy as the "insitu" stellar component, while stars which were born in satellite galaxies and later on accreted by the galaxy as the "accreted" stellar component.

Substructure: Observational constraints on the substructure within the stellar halo allows one to predict the progenitors of a galaxy (Helmi & White, 1999) as well as the shape and potential of its dark matter halo. Constraints on the Milky Way's dark matter halo can be achieved by modelling the streams observed across the greater part of the night sky (Bonaca et al., 2014; Ibata et al., 2013). Similar modelling of stellar streams around neigh-

boring galaxies allows one to infer the mass of the progenitor as well as the virial mass, concentration and shape of the halo (Amorisco et al., 2015). Phase-space information from upcoming surveys like PanSTARRs, DES, LSST (Large Synoptic Survey Telescope) and GAIA combined with chemical tracers from spectroscopic surveys like CoRoT, RAVE, APOGEE and 4MOST[1] will allow for a detailed modeling of the stellar halo of the Milky Way and a prediction of its progenitors (for example Lee et al., 2015).

Radial Profiles: Studying the radial stellar mass density profiles of a large population of galaxies can also constrain galaxy formation models. In particular, the shape of the surface brightness profile of a galaxy encodes important information of its formation history (Hubble, 1936; de Vaucouleurs, 1948; Freeman, 1970; Sérsic, 1968).[2]

The surface brightness profile of a galaxy directly reflects the stellar population of infalling galaxies, the rate at which haloes coalesce as well as the gravitational dynamics of the accretion process. For example, since galaxies accrete the majority of their stellar mass from subhaloes of mass $M_{sat} \sim 0.05 - 0.1\, M_{host}$ (Purcell et al., 2007), changes to the M/L ratio in the form of reduced star formation efficiency can change the amount of stellar material accreted. This has been borne out in numerical simulations where changes in the star formation efficiency and feedback prescriptions increase the fraction of accreted stellar material in a galaxy by a factor of 2 (Lackner et al., 2012). Large accretion events can also leave a direct imprint on the stellar halo in the form of a radial surface brightness "break", as is found in the Milky Way (Watkins et al., 2009; Deason et al., 2011; Sesar, 2011). Moreover as we will discuss later, accreted progenitors contribute differently to the radial profile depending on its merger fraction as well as the time it was accreted (Amorisco et al., 2015).

Using numerical simulations, Pillepich et al. (2014) parametrized the stellar halo of galaxies by calculating the outer slope of the surface brightness profile and showed that it directly correlates with the accretion history of the galaxy. Furthermore, Abadi et al. (2006) predicted that there would be an abrupt change in the surface brightness profile of the galaxy at the radius (R_{acc}) where the accreted stellar component begins to dominate over the insitu stellar component. This was later corroborated by Cooper et al. (2013), who further showed that the radial profile of each component could be approximated by Sérsic models. The accreted stellar fraction of a galaxy could potentially be constrained by fitting multi-component Sérsic models to its surface brightness distribution (See Figure 1.1).

Since the stellar halo lies in the dark-matter dominated region of the galaxy, information about the shape of the stellar halo helps constrain the shape and orientation of the dark matter halo. Further more, kinematic information of the stellar halo can be used to constrain the total mass-density profile of the galaxy (Cappellari et al., 2015).

---

[1]COnvection ROtation and planetary Transits (CoRoT), Radial Velocity Experiment (RAVE), APO Galaxy Evolution Experiment (APOGEE), 4-meter Multi-Object Spectroscopic Telescope (4MOST)

[2]For example, deviations of the surface brightness from simple laws (de Vaucouleurs, exponential or Séric $\log I(R) \propto R^{1/n}$ law) lead to the discovery of bulges and helped distinguish pseudo-bulges ($n \sim 1$) from classical bulges ($n \sim 4$) (Kormendy et al., 2009).

Stellar population gradients obtained from colour, metallicity and abundance profiles (Monachesi et al., 2013, 2015; Rejkuba, 2014; Greene et al., 2012, 2013, 2015; Pastorello et al., 2015) of the stellar halo can further constrain galaxy formation models (Font et al., 2006, 2011). Colour and metallicity gradients formed in minor mergers are significantly steep, while galaxies with major mergers have relatively flat gradients (Navarro-Gonzalez et al., 2013). Hirschmann et al. (2015) demonstrated that the current observational metallicity and colour gradients are consistent with theoretical models which include galactic winds. Such models give rise to galaxies with lower accreted mass fractions and steeper metallicity gradients. Furthermore, chemical abundances of the stellar halo can set constraints on the environment in which these stars were born.

Quantifying the outer stellar mass: Finally, quantifying the contribution of stars in the halo to the total stellar mass of massive galaxies ($M_{star} \geq 10^{11.5} M_\odot$) gives us important constraints on how these galaxies grow through accretion over cosmic time.

There is increasing observational evidence that massive galaxies grow inside out through dry mergers, with the addition of stellar material in their outer parts (van Dokkum et al., 2010; Patel et al., 2013). Lidman et al. (2012) and Lin et al. (2013) found that the stellar mass of BCGs increases by a factor of 2 since $z \sim 1$. However, there still exists considerable debate about the assembly history of these massive galaxies (Zhang et al., 2016; Vulcani et al., 2016). In theoretical models, this growth occurs through the accretion of satellite galaxies through minor mergers leading to a size increase of the galaxy (Naab, Johansson & Ostriker, 2009). On the other hand, a number of observational works point to major mergers as a possible channel of mass growth (e.g. Lidman et al., 2013). Each of these formation mechanisms will leave a distinctive imprint on the stellar material in the outer part of massive galaxies. Studying the stellar haloes of these massive galaxies can help quantify the contribution from major and minor mergers to the overall growth of massive galaxies

The growth of massive galaxies can also be studied statistically by estimating the evolution of their space density over time. While existing studies indicate only a little or mild evolution in the galaxy stellar mass function at the massive end since $z \sim 1$ (Maraston et al., 2013; Moustakas et al., 2013; Davidzon et al., 2013), a significant fraction of the stellar material in the LSB outer component may be systematically missed in shallow all-sky surveys. Estimating accurately the contribution of the stellar halo to the total stellar mass of a galaxy will help constrain the evolution at the massive end of the stellar mass function.

1.2 Observing Stellar Haloes

Although they contain a wealth of information, stellar haloes of galaxies are extremely difficult to observe. These LSB features require a depth of nearly $30\,\text{mag arcsec}^{-2}$ to detect, which is typically 9-10 magnitudes (0.05%) below the surface brightness of the night sky.
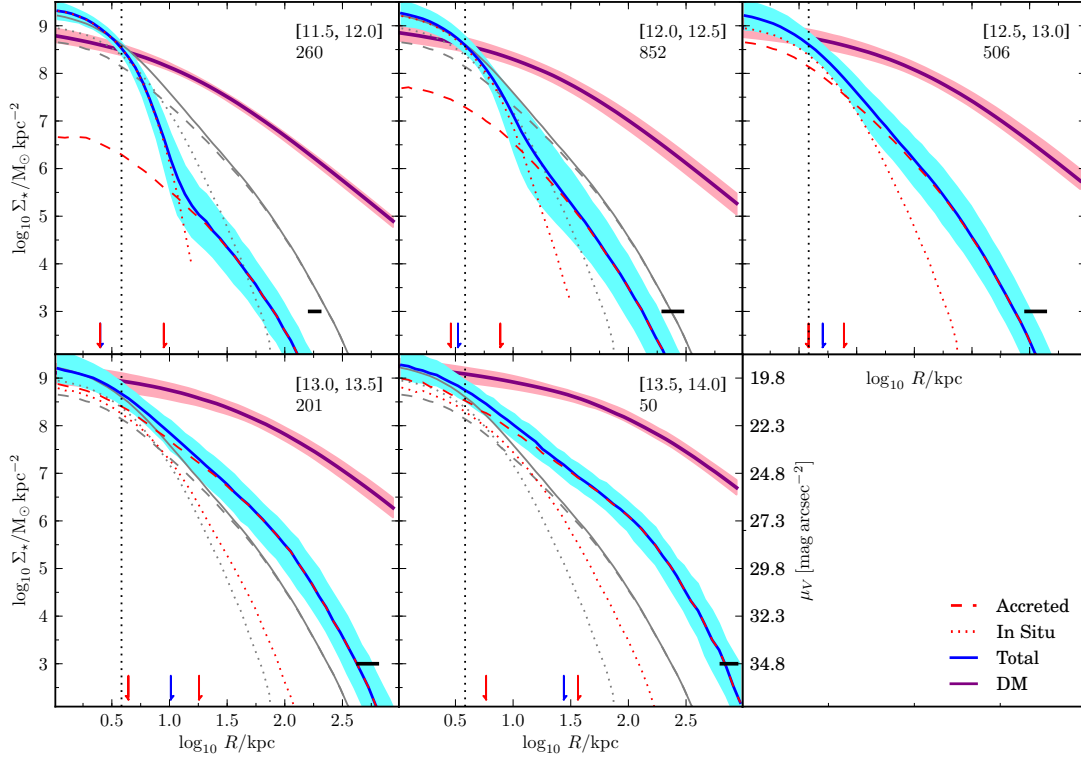
Figure 1.1: **Stellar mass surface density profiles from models of Cooper et al. (2013)**: Median profiles of circularly averaged stellar mass surface density $\Sigma_\star$ for all stars (blue solid lines), accreted stars (red dashed lines), in-situ stars (red dotted lines) and dark matter (purple solid lines) in logarithmic bins of dark halo virial mass (range of $\log_{10} M_{200}/M_\odot$) for $f_{mb} = 1\%$. Shaded regions shows 10-90 per cent scatter of the median profile. Arrows indicate half-mass radii of the median profiles (from left to right, in situ stars, all stars and accreted stars). Grey lines (dotted, dashed and solid) reproduce the corresponding red and blue lines from the $12.5 < \log_{10} M_{200}/M_\odot < 13.0$ panel. The scale on the right of the lower central panel gives an approximate conversion from $\Sigma_\star$ to surface brightness (in Vega magnitudes per square arcsecond) for the Johnson-Cousins V band, assuming $\Upsilon_V = M_\star/L_V = 2.5$ (Cooper et al., 2013).
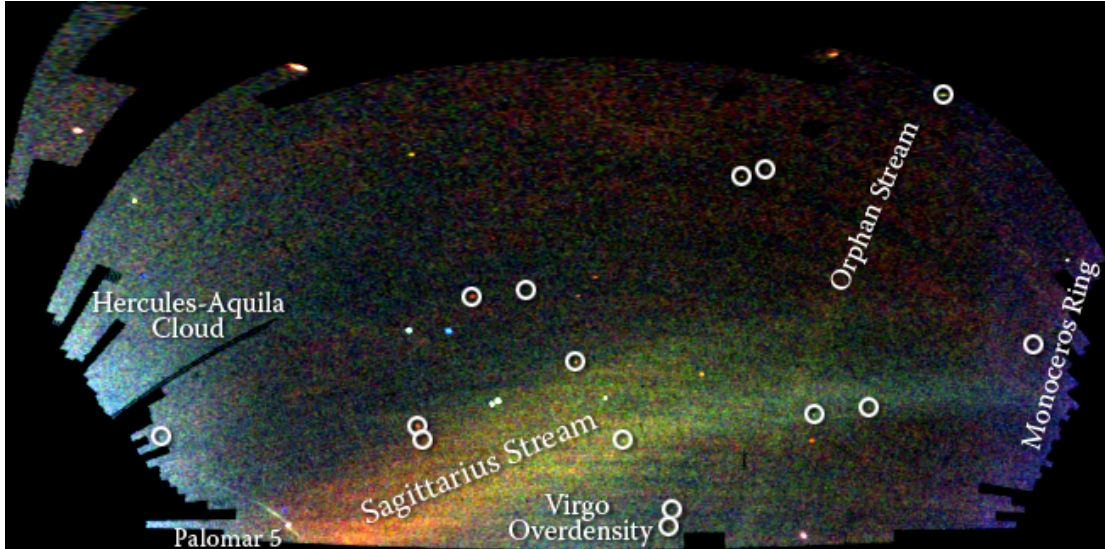
Figure 1.2:   A map of stars in the outer regions of the Milky Way Galaxy, derived from the SDSS images of the northern sky, shown in a Mercator-like projection.   The color indicates the distance of the stars, while the intensity indicates the density of stars on the sky. Structures visible in this map include streams of stars torn from the Sagittarius dwarf galaxy, a smaller 'orphan' stream crossing the Sagittarius streams, the 'Monoceros Ring' that encircles the Milky Way disk, trails of stars being stripped from the globular cluster Palomar 5, and excesses of stars found towards the constellations Virgo and Hercules. Circles enclose new Milky Way companions discovered by the SDSS; two of these are faint globular star clusters, while the others are faint dwarf galaxies (Belokurov et al., 2006).

They can be observed either through deep number counts of resolved stars or through deep integrated observations of nearby galaxies.

Resolved Stellar Populations: The earliest studies of the stellar halo of our own Galaxy was done by observing individual RR Lyrae stars out to 20 kpc.   Their distribution was found to follow a decreasing power law (Kinman et al., 1966, 1982), which was consistent with the distribution of globular clusters in the Milky Way (Harris, 1976). However, it was the advent of all sky surveys (Two Micron All Sky Survey-2MASS and Sloan Digital Sky Survey - SDSS) which revealed that the Milky Way stellar halo was far more complex than originally thought, possessing asymmetries and showing evidence of streams and clumps in phase space (Majewski et al., 1996; Helmi et al., 1999; Ivezic et al., 2000; Newberg & Yanny, 2006; Juric et al., 2008). The most striking example was the discovery of the Sagittarius dwarf galaxy (Ibata et al., 1994, 1995) and its associated trails of debris which have now been traced entirely around the Galaxy (Ibata et al., 2001; Majewski et al., 2003).   In Figure 1.2, we show a map of stars in the outer region of the Milky Way Galaxy derived from the SDSS survey, where the Sagittarius stream is clearly visible as an overdensity.
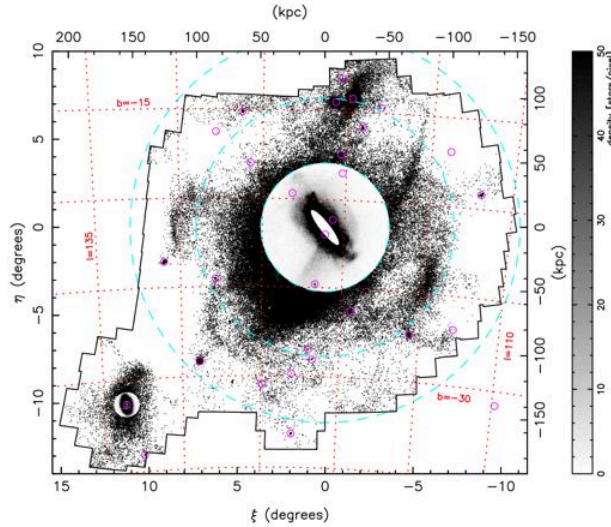
Figure 1.3: Map of halo stars of M31 from the PAnDAS survey. Stars were selected such that $(gi)_0 < 1.8$, $2.5 < [Fe/H] < 0$ and $i_0 < 23.5$. The contamination from the foreground Milky Way as well as that from unresolved background galaxies has been removed in a statistical manner. The dense regions around M31 (radius 50 kpc) and M33 (radius 10 kpc) are shown as grayscale density images, while the outer data are shown with points. The pink circles indicate the positions of the known satellites dwarf galaxies of M31 (Ibata et al., 2014)

The stellar haloes of nearby galaxies can also be studied by observing their individual stars. The Pan-Andromeda Archaeological Survey (PAndDAS) by mapping the sky around M31 revealed its extensive stellar halo (McConnachie et al., 2009). In Figure 1.3, we show the 2D image of the stellar halo of M31 along with the presence of copious substructures. Ibata et al. (2014) found that the global halo populations of M31 follow closely power law profiles that becomes steeper with increasing metallicity. Further out, the GHOSTS (Galaxy Haloes, Outer disks, Substructure, Thick disks and Star clusters) survey (Radburn-Smith et al., 2011; Monachesi et al., 2013) was able to map the stellar haloes of nearby disk galxies using space-based HST (Hubble Space Telescope) imaging. The stellar haloes of a few nearby elliptical galaxies have also been studied through HST imaging (Rejkuba, 2014; Bird et al., 2014).

Deep Integrated Observations: The stellar haloes of galaxies further away can be studied through their integrated light. Critical to such studies are long integration times, very accurate flat fielding, and a good background subtraction. Scattering and internal reflections can be minimized in small aperture telescopes allowing for very good flat fielding and reaching a low surface brightness of $\mu_V \sim 28.5\,\mathrm{mag\,arcsec^{-2}}$ (Martinez-Delgado et al., 2010, 2012, 2015). Particularly remarkable is the custom-built Dragonfly telescope van Dokkum et al. (2014), built from an array of commercial telephoto lenses with nano-fabricated coatings which suppress internal reflection. It is reported to reach a limiting

Figure 1.4: The stellar halo of early-type galaxy NGC0474 taken from the Canadian French Hawaiian Telescope (CFHT) with an integration time of 40 mins reaching down to a depth of $\mu_g \sim 29 \, \mathrm{mag \, arcsec^{-2}}$. The scale of the image is 70 kpc x 70 kpc (Duc et al., 2015).

depth of $\mu_g \sim 31 \, \mathrm{mag \, arcsec^{-2}}$.

Reaching such low surface brightness is more difficult with larger telescopes due to the reflections and scattering of the supporting structures. Nevertheless, the ATLAS3D project (Cappellari et al., 2011) was able to study the surface brightness of nearby early type galaxies down to $\mu_V \sim 28.5 \, \mathrm{mag \, arcsec^{-2}}$ with the 3.6 meter Canadian French Hawaiian Telescope (CFHT) using an innovative flat fielding technique (Duc et al., 2015). In Figure 1.4, we see a combined g+r+i deep image of an early-type galaxy NGC0474, showing numerous shells and streams around the galaxy. Similarly, Trujillo & Fliri (2015) demonstrated that it was possible to detect optical surface brightness structures down to $\mu_r \sim 33 \, \mathrm{mag \, arcsec^{-2}}$ using a 10 meter class telescope (*Gran Telescopio de Canarias*).

Stacking Galaxies: With the above two techniques, it is still presently unfeasable to study the stellar haloes of a large statistical sample of galaxies. The stacking of similar galaxies together from all sky surveys (like SDSS, Panoramic Survey Telescope and Rapid Response System - PanSTARRS, Canada-France-Hawaii Telescope Legacy Survey - CFHTLS, Dark Energy Survey - DES) is an alternative and viable method to study the average properties of the stellar haloes of galaxies. In particular, galaxy images from SDSS are well suited for this task. SDSS has imaged nearly one-third of the sky in multiple bands and obtained spectra for more than three million astronomical objects, creating one of the most detailed 3D maps of the Universe. In addition, its unique drift scan approach for imaging has provided a uniform and remarkably flat data set. The stacking of SDSS galaxies has been successfully used to study the average stellar haloes around edge-on disk galaxies (Zibetti et al., 2004) and massive red galaxies (Tal & van Dokkum, 2011) as

well as the inter-cluster light of BCGs (Zibetti et al., 2005) reaching down to a depth of $\mu_r \sim 31\,\mathrm{mag\,arcsec}^{-2}$. Stacking of large number of images of galaxies from all-sky surveys has a lot of potential to study the stellar haloes of galaxies over a range of stellar masses, galaxy types and environment.

1.3   Modeling Stellar Haloes

In order to further our understanding of the processes involved in the formation of stellar haloes through accretion, we need to confront our theoretical models of the spatial distribution of the stellar halo particles, as well as the their properties such as age and chemical abundance, with the results from observations. A number of such theoretical models of the stellar halo were mentioned earlier. These can be broadly classified in two main categories: cosmological hydrodnamical simulations and hybrid methods.

In the former, galaxies are simulated in N-body cosmological simulations codes while directly accounting for the baryonic content (gas, stars, supermassive black holes) and dark matter (Abadi et al., 2006; Sales et al., 2007; McCarthy et al., 2012; Font et al., 2011; Lackner et al., 2012; Oser et al., 2010; Pillepich et al., 2014). The relevant baryonic physics which cannot be resolved (star formation, stellar evolution and ISM enrichment, stellar and AGN feedback, etc) is included through a number of prescriptions commonly labeled as sub-grid physics. The advantage of this technique from the perspective of modeling stellar haloes is that it self-consistently models the insitu stars and those accreted from other progenitors. Disadvantages include the long time frame to run such simulations. It is for this reason that the recent public availability of large-scale hydrodynamical simulations (Vogelsberger et al., 2014; Schaye et al., 2014), which for the first time can create disk and elliptical galaxies in the same way, is game-changing and exciting.

Hybrid techniques, on the other hand, offer a less computationally expensive alternative to study the stellar haloes of galaxies (Bullock & Johnston, 2005; Font et al., 2006; Purcell et al., 2007; Cooper et al., 2010, 2013). It does so by coupling N-body dark matter only simulations with the results of semi-analytical models (Frenk & White, 1991; Kauffmann et al., 1993). In semi-analytical models, the complicated, tightly intertwined astrophysical processes (cooling, star formation, dynamical friction, etc.) associated with the formation and evolution of baryonic component of galaxies are modeled as a set of 'recipes' and 'prescriptions', along with the information of the structure and assembly history of cold dark matter haloes. The free parameters of these recipes are chosen so as to 'normalize' the model using a set of observational constraints.

Hybrid techniques work on the principle of 'particle-tagging' first implemented by Bullock & Johnston (2005) to model the stellar halo of the Milky Way. In practice, at each snapshot, the most bound particles of the dark matter halo are 'tagged' with a stellar population (of a single age and metallicity) predicted by a semi-analytical model. The tagged particles can be used to track the evolution of the associated population in phase space, from the time when the star forms to the present day. The model galaxies at $z = 0$ is a superposition of many such populations, including accreted stars formed in their hier-

archical progenitors. Cooper et al. (2013) modeled the stellar haloes of a wide variety of galaxies by coupling the Guo et al. (2010) semi-analytical model with the Millennium II N-body simulations (Boylan-Kolchin et al., 2009). They predicted the stellar mass surface density profiles as a function of halo mass.

Although hybrid techniques like that of Cooper et al. can produce the full phase-space information of the stellar halo of the galaxy, it does not self-consistently model the surface density profile of the insitu stellar distribution of the galaxy, particularly where the surface density of the stellar component exceeds that of the dark matter. Neglecting to model the baryonic physics self-consistently with the dark matter reduces the stellar halo concentration and internal structure while making the stellar halo more prolate (Bailin et al., 2014).

We summarize below the main results from modelling the stellar haloes of galaxies:

1. Stellar haloes of galaxies are assembled inside out by the accretion of smaller galaxies. The outer stellar halo is built more recently than the inner stellar halo (Bullock & Johnston, 2005).

2. For massive galaxies ($M_{vir} > 10^{13}\mathrm{M}_\odot$), the majority of the accreted stellar mass ($\sim 60-80\%$) comes from the tidal disruption of 10-15 most massive galaxies accreted 9-10 Gyrs ago (Cooper et al., 2013). These massive satellite galaxies suffer the most dynamical friction and deposit their stars deep in the gravitational potential of the main galaxy (Sales et al., 2007). Earlier accretion events contribute more to the inner regions of the stellar halo of the galaxy (≤ 5 kpc) (Amorisco, 2015).

3. For less massive galaxies ($M_{vir} < 10^{13}\mathrm{M}_\odot$), the accreted stellar material is dominated by fewer progenitors ($\sim 1-5$) with a great diversity in their stellar haloes. The scatter in the number of significant progenitors of stellar haloes is larger at lower M_{vir} (Bullock & Johnston, 2005; Cooper et al., 2010, 2013).

4. The bright tidal features generally observed in the outer regions of the galaxy are from more recent accretion events ($\sim$ 4-5 Gyrs ago) from less massive systems (Bullock & Johnston, 2005; Sales et al., 2007). However, stars stripped from these surviving satellites contribute only to $\sim 6\%$ to the total mass of the stellar halo (Sales et al., 2007). There are substantial differences in both the population and kinematics between the stellar halo and the surviving satellite population in a galaxy.

5. A small fraction of the stellar halo can also be from stars formed in the disk but heated through accretion events (Purcell et al., 2010; McCarthy et al., 2012; Cooper et al., 2015).

6. Negative metallicity gradients in Milky Way-like galaxies may originate from the transition between the insitu and accreted stellar components of the galaxy (Font et al., 2011).

7. The stellar haloes of galaxies are oblate and are supported by a substantial velocity dispersion tensor and a radially increasing velocity anisotropy due to dynamical friction (Abadi et al., 2006). Simulated Milky Way-like galaxies show a large variation with both rotation and anisotropy contributing to the flattening of the halo McCarthy et al. (2012).

8. The fraction of accreted mass of the galaxy increases strongly with halo mass (Purcell et al., 2007; Cooper et al., 2013). The accreted stellar material can be nearly 60-80% of the total stellar mass of large elliptical galaxies. Galaxies with a higher bulge-to-total mass ratio have a higher accreted fraction than those with a lower bulge-to-total mass ratio (Cooper et al., 2013).

9. Massive galaxies increase both in stellar mass and size by the accretion of smaller satellite galaxies from their initial compact progenitors (Naab, Khochfar & Burkert, 2006; Naab et al., 2007; Naab, Johansson & Ostriker, 2009; Oser et al., 2010; Hilz et al., 2012; Hilz, Naab & Ostriker, 2013).

1.4   This Thesis

In this thesis, we use the potential of stacking SDSS galaxy images to study the average properties of the stellar haloes of central galaxies over a range of stellar masses, galaxy types and environment. For this purpose, in Chapter 2, we stack aligned r and g band images from a sample of 45508 galaxies from SDSS DR9 in the redshift range $0.06 \leq z \leq 0.1$ and in the mass range $10^{10.0} M_\odot < M_* < 10^{11.4} M_\odot$ as a function of stellar mass and galaxy type. We can thus study the average properties of the stellar haloes of these galaxies out to 70-100 kpc and we reach a surface brightness depth of almost $\mu_r \sim 32 \, \mathrm{mag \, arcsec^{-2}}$. We study the ellipticity and colour profiles of the stellar halo as a function of galaxy stellar mass and galaxy type.

We systematically characterize the 2D surface brightness distribution of the stacked images of galaxies by fitting multi-component Sérsic models. In Chapter 3, using mock images from simulations, we also demonstrate that the fraction of light contained in the outer Sérsic component is a good proxy for the accreted stellar mass fraction. Using this outer light fraction and a larger volume limited sample, we provide the first observational constraints on the accreted stellar mass fraction as a function of galaxy stellar mass, type and environment.

In Chapter 3, we further study the stellar haloes of galaxies through stacking as a function of their halo mass as estimated from the Yang et al. (2007) galaxy group catalogue. We study the correlation between the outer light fraction and various galaxy properties. We further compare our results with those from the Illustris simulations.

Finally, in Chapter 4, we try to obtain better constraints on the stellar masses of the largest viralized structures in the Universe so to improve our estimates of their number density. We do this by using the increased S/N of our galaxy stacks to measure the mass of the systems that may be "hiding" in the outer low surface brightness components of

galaxies that are systematically missed by conventional photometric extraction software: we derive average flux corrections to the `Model` magnitudes of SDSS galaxies by stacking together mosaics of similar galaxies in bins of stellar mass and concentration. Using this information, we re-estimate the galaxy stellar mass function at $z = 0.1$ using the SDSS data set, and provide improved constraints on the massive end of the stellar mass function.

Chapter 2

The Stellar Haloes of Galaxies

Note: This chapter has been published in Monthly Notices of the Royal Astronomical Society *(D'Souza et al., 2014).*

2.1 Introduction

Traditionally, galaxies have been studied through their surface brightness profiles (Hubble, 1936; de Vaucouleurs, 1948). This has not only revealed a wealth of information about their different morphologies but also hints about their formation processes. De Vaucouleurs (1948) first characterised the surface brightness profiles of giant elliptical galaxies as a simple $\log I(R) \propto R^{1/4}$ law, which was later also found to fit the bulges of disk galaxies. On the other hand, the disks of spiral galaxies have been traditionally fit with exponential profiles (Freeman, 1970). Sérsic (1968) showed that all these profiles are specific cases of a more general $\log I(R) \propto R^{1/n}$ function, which fits the surface brightness profile of a large number of galaxies from disks to spheroidals, dwarfs, ellipticals and bulges. The shape of the surface brightness profile provides valuable clues about the way in which different galaxies formed.

As deeper and more resolved surface brightness data became available, deviations from these simple laws became clearly evident, indicating that galaxy formation was a more complex process than previously believed (Kormendy et al., 2009). This discovery motivated the use of multiple components to model the surface brightness profiles of galaxies (Kormendy, 1977; Simard et al., 2011; Lackner & Gunn, 2012). Bulge-disk decompositions helped distinguish pseudo-bulges ($n \sim 1$) from classical bulges ($n \sim 4$). Pseudo-bulges are dense central components of disk galaxies that are flattened and rotationally supported and believed to be built out of disk gas. Classical bulges lie on the fundamental plane linking galaxy size, luminosity and velocity dispersion (Bender, Burstein & Faber, 1992).

With the advent of deeper imaging (through Hubble Space Telescope and medium-sized, ground-based telescopes), it has become possible to detect additional fainter stellar structures around both normal galaxies and brightest cluster galaxies, and to study their surface brightness profiles through number counts and integrated light (Bell et al., 2008;

Ibata et al., 2014; Monachesi et al., 2013; Martinez-Delgado et al., 2010; Tal et al., 2009; van Dokkum et al., 2014). Stacking the images of a large number of similar galaxies (e.g. Zibetti et al. 2004,Zibetti et al. 2005, Tal & van Dokkum 2011 and Cooper et al. 2013) from all sky surveys enables one to study the average stellar haloes of statistical samples of more distant galaxies. Zibetti et al. (2004) used stacking techniques to study the stellar haloes of edge-on disk galaxies; Tal & van Dokkum (2011) studied the stellar haloes of luminous red galaxies out to $z \sim 0.34$. Such observational studies help constrain theoretical models for the formation of the stellar haloes of galaxies.

In this Chapter, we stack a large number of galaxy images from the SDSS imaging data and study them as a function of stellar mass and galaxy type (late-type or early-type). Although the SDSS imaging data are relatively shallow, they provide a large number of images with reasonable good quality and consistent calibration, and hence are well-suited for stacking to study the faint stellar haloes of galaxies (Zibetti et al., 2004, 2005; Tal & van Dokkum, 2011). The systematics of stacking many SDSS images to produce a very deep image have been also well understood and quantified. This is important because studying low-surface brightness structures is highly dependent on a proper estimation and removal of the sky background. We pay particular attention to the residual sky background obtained after stacking the sky-subtracted images from SDSS DR9. We then model the surface brightness profile of the stacked galaxy including the stellar halo through multi-component fits. We then parametrise the contribution of the stellar halo by deriving the fraction of light in the outer component of the galaxy.

In Section 2.2, we describe how we select and prepare our galaxy images for stacking. In Section 2.3, we describe in detail the stacking procedure, our error analysis, PSF analysis and the methodology we employ to derive the ellipticity, surface brightness and the colour profiles for each galaxy stack. In Section 2.4, we present the surface brightness and colour as a function of the stellar mass of the galaxy and of galaxy type. In Section 2.5, we fit models to these surface brightness profiles and determine the fraction of light in the outer faint stellar component. In Section 2.6, we summarise and in Section 2.7, we discuss our results in light of our theoretical understanding of the formation of stellar haloes of galaxies. Throughout this paper, we assume a flat ΛCDM cosmology, $\Omega_{\mathrm{m}} = 0.25$, $\Omega_{\Lambda} = 0.75$ and Hubble parameter $h = 0.73$.

2.2   Sample Selection and Image Preparation

We select isolated central galaxies from the MPA-JHU SDSS spectroscopic 'value-added' catalogue in the stellar mass range $10^{10.0} M_{\odot} < M_* < 10^{11.4} M_{\odot}$ and in the redshift range $0.06 \leq z \leq 0.1$.[1] We apply the isolation criterion outlined in Wang & White (2012): a galaxy of apparent r-band magnitude $m_{central}$ is considered isolated if there are no galaxies

---

[1]The stellar masses used here are as defined by the MPA-JHU catalogue (using a methodology similar to that described in Kauffmann et al. 2003) and corrected for the Hubble parameter $h = 0.73$. The stellar mass estimates in the MPA-JHU catalogue were derived from fits to the SDSS fibre photometry and the total `ModelMag` photometry.

in the spectroscopic catalogue at a projected radius $R < 0.5\,\mathrm{Mpc}$ and velocity offset $|\delta z| < 1000\,\mathrm{km\,s^{-1}}$ with magnitude $m < m_{central} + 1$, and none within $R < 1\,\mathrm{Mpc}$ and $|\delta z| < 1000\,\mathrm{km\,s^{-1}}$ with $m < m_{central}$. We remove all edge-on disk galaxies to avoid adverse PSF effects along the minor axis (de Jong, 2008) by choosing only those galaxies with isophotal minor-to-major axis ratio $b/a > 0.3$.

We construct mosaics (1200 x 1200 pixels) in the g, r and i bands centred on each galaxy using the sky-subtracted SDSS Data Release 9 images and `SWarp` (Bertin et al., 2002). Galaxies were removed if found unsuitable for stacking. First, galaxy images with a bright source with an r-band petrosian magnitude greater than 12.0 and within a distance of 1 Mpc from the centre of the galaxy were removed. Secondly, if the masking algorithm (outlined later) failed due to crowded fields, the galaxy image was discarded. Finally, we calculated a histogram of the difference between each galaxy mosaic after masking and transformation (see later) and the stacked image. Galaxy mosaics lying more than $5\,\sigma$ from the mean were discarded. The final sample contains a total of 45508 galaxies.

For our later analysis, we will stack according to stellar mass and concentration. For the stellar mass stacks, we stack galaxies in stellar mass bins of 0.1 dex. For the highest mass bin we stack in a bin size of 0.4 dex. Each stack contains both early and late-type galaxies: late-type galaxies dominate the stacks of lower stellar mass whereas early-type galaxies are predominant at high stellar masses. We can parametrise the shape of the galaxy by using the concentration index $C = R90/R50$ (where $R90$ and $R50$ are the radii containing 90 and 50 per cent of the Petrosian r-band luminosity of the galaxy). It has been demonstrated that $C \sim 2.6$ marks the transition from late-type to early-type morphologies (Strateva et al., 2001). In order to study the stellar halo separately for late-type and early-type galaxy morphologies, we divide our sample into stellar mass bins of 0.2 dex with a further separation of each stack into high concentration ($C > 2.6$) and low concentration galaxies ($C < 2.6$). The number of galaxies in each stack is displayed visually in Figure 2.1.

Conservative masking was employed by using multiple runs of `SExtractor` (Bertin & Arnouts, 1996) to create segmentation maps. For this purpose, the mosaics of three bands were stacked together to make a 'master image', from which several segmentation masks were created to deal with various types of background and overlapping objects. We used a minimum detection area of 5 pixels, a Gaussian filter for detection and a detection threshold of $1.5\,\sigma$ to create all the masks. For the background detection, we use three variations. We first calculated the mask with a global background. We then calculate the mask with a local background size of 256 pixels with a filter of 20 pixels. Later we calculated a mask with a smaller background size of 128 pixels with a similar filter size. To deal with extended faint objects, a mask was also created by convolving the master image with an 8×8 pixel top hat kernel before running `SExtractor`. Each of these masks were successively applied to individual g and r-band mosaics. The i-band mosaics were only used for creating the master images for the masking procedure.

The masked mosaics were then transformed to $z = 0.1$ with the flux-conserving IRAF task `GEOTRAN`. This involves both a cosmological surface brightness dimming $(1 + z)^4$ and an image rescaling. For the final transformed mosaic at $z = 0.1$, $1\,\mathrm{pixel} = 0.71\,\mathrm{kpc}$. The mosaics were further cropped to a uniform size of 950×950 pixels (550×550 kpc at
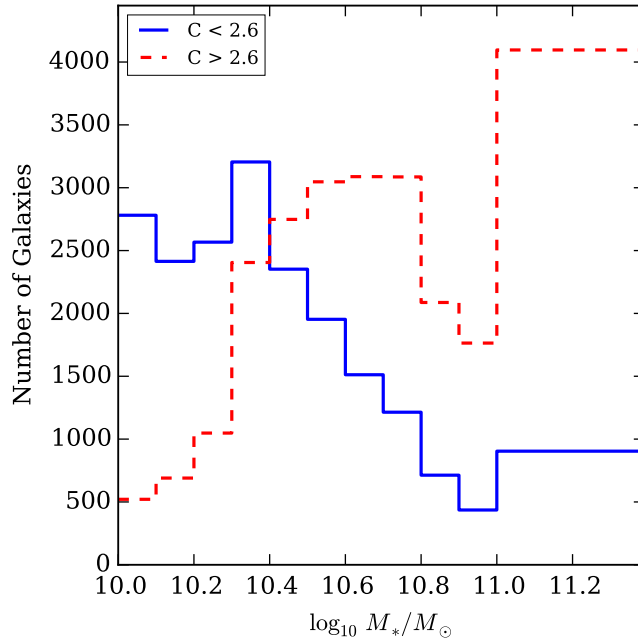
Figure 2.1: The number of galaxies in each mass bin (0.1 dex in width) split according to low concentration ($C < 2.6$ blue solid line) and high concentration ($C > 2.6$ red dashed line) galaxies. The highest mass bin is 0.4 dex in width.

$z \sim 0.1$) and corrected for Galactic extinction following Schlegel et al. (1998). We ignored K-corrections in scaling the images as they tend to be minimal at $z < 0.1$.

A sizable number of the final transformed images are oversampled. However, for the redshift shift range chosen for our sample $z = 0.06 - 0.1$, this does not significantly affect the noise characteristics of our final transformed images. A final run of SExtractor was used to determine the position angle of the galaxy in the r-band mosaic. This position angle is measured by calculating the second-order moments of the intensity distribution and corresponds to surface brightness threshhold $\mu_r \sim 24\,\mathrm{mag\,arcsec^{-2}}$, or a radius of $\sim$10 kpc. Each mosaic was then rotated using `GEOTRAN` such that the major axis of each galaxy was aligned.

We note that combining galaxy images into mosaics may introduce additional systematics. Blanton et al. (2011) compared the mosaics created from the sky-subtracted images of DR9 and those created directly from the raw images and found that they yield equivalent results.

The sky subtraction in DR9 (Blanton et al., 2011) is a remarkable improvement from early data releases especially for the extended low surface brightness regions around low-redshift galaxies. Blanton et al. (2011) calculate the residual sky background by measuring the mean surface brightness in random patches of size 13 x 13 native SDSS pixels marked as "sky" in the SDSS pipeline across all imaging runs (see Figure 5 of Blanton et al. 2011. These residuals become significant at depths beyond $\mu_r \sim 26\,\mathrm{mag\,arcsec^{-2}}$. We will discuss

this further in the next section.

2.3 Image Stacking and Methodology

2.3.1 Stacking Procedure

Each stack contains between 1000 and 5000 galaxies with an average of 3000 galaxies. The mosaic images in the g and r bands were stacked using the IRAF task `IMCOMBINE`, by taking the mean value of each pixel after clipping at the 10th and 90th percentiles.[2] The images were not weighted in the stacking process so as not to bias the sample. The masked parts of the images were not used when calculating the mean value in `IMCOMBINE`. To make the stacking computationally easier, the final stacks were built by combining equal stacks of around ~ 100 galaxy images each. By working in narrow mass bin ranges, we avoid the difficult problem of normalising the size of images in each bin prior to stacking.

2.3.2 Estimation of Background for Stacked Galaxies

The background "sky" for individual DR9 images consists of the 'residual' sky background and light from undetected (unmasked) galaxies. In the Appendix A.1, we quantify the level of light from undetected sources. This tends to be minimal due to the strict masking procedures employed and the fact that we only select isolated galaxies.

To estimate the residual sky background for the stacked image, we calculate the mean intensity in an annulus between 280 and 320 kpc (400-450 pixels) from the centre of the stacked image. We assume that this background is constant over the whole image. To calculate the uncertainty in this background estimation, we calculate the standard deviation of the mean calculated in patches of 16 x 16 pixels within this annulus.

With the standard SDSS imaging, it is possible to extract radial surface brightness profiles down to $\mu_r \sim 27 \, \mathrm{mag \, arcsec}^{-2}$ (Pohlen & Trujillo, 2006). With a better residual background estimation of high S/N stacked DR9 images, it is possible to go significantly deeper. In Figure 2.2, we plot the uncertainty in the residual background estimation and the corresponding limiting depth in the r-band as a function of the number of co-added objects. The uncertainty in the residual background estimation can be fit by the function $0.00442/\sqrt{N_{Images}} \mathrm{nanomaggies \, arcsec}^{-2}$.

2.3.3 Error Estimation

For stacks of a few thousand galaxies, the formal uncertainty in the stacked surface brightness profiles at larger radii is dominated by the uncertainty in subtracting the background sky, which consists of camera noise plus extragalactic background radiation originating in the stellar populations of galaxies at moderate to high redshift. These uncertainties calculated as described in the previous section are depicted as solid error bars in the plots

---

[2]Percentile clipping also helps prune any close satellite galaxies which escape the masking procedure.
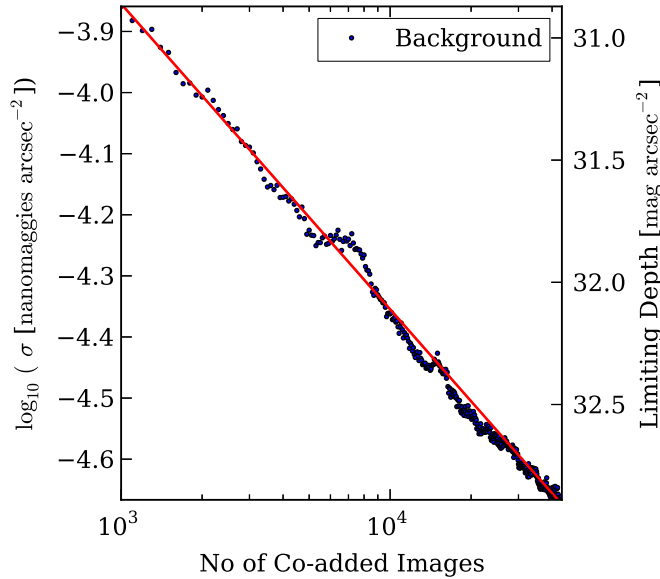
Figure 2.2: The logarithm of the uncertainty in background removal as a function of the number of co-added images. The right axis depicts the limiting surface brightness depth. The red line indicates the function $0.00442/\sqrt{N}_{Images}$ nanomaggies arcsec^{-2}.

discussed in the next section. In addition to the uncertainty that arises from the sky subtraction, it is interesting to consider the variance that arises from the fact that similar galaxies may have stellar haloes with quite different masses and sizes. This can be quantified for each pixel in our final g and r band stacks through a bootstrapping procedure. For each bin, 3000 stacks were created with repetition and the variance in each pixel is calculated for each band. This gives the total uncertainty of each pixel. After accounting for the formal uncertainty, the variance in the surface brightness profiles can be calculated and is depicted as shaded regions in the plots.

To verify that the faint outer stellar halo visible in our stacks between $30-32\,\mathrm{mag\,arcsec^{-2}}$ is not a product of systematics in the data or due to our stacking procedure, we created equivalent background stacks (nearly 3000 images) for each bin by choosing a location 5 Mpc away from the centre of the galaxy in a random direction where no large galaxies were found within a distance of 1 x 1 Mpc. We found that evaluating the background at these very large distances made no difference to our results.

2.3.4 PSF Effects

The PSF flattens the ellipticity and the surface brightness profiles at the centre of the galaxy at radii less than ~ 10 kpc. For deep images, the light in the faint outskirts of the stack can be dominated by the scattered light from the centre of the galaxy. Failure to
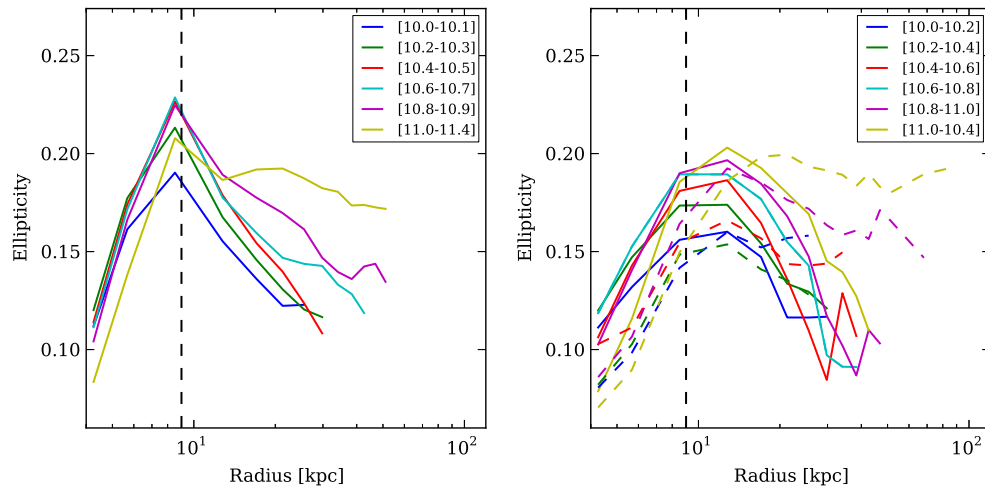
Figure 2.3: (a) Ellipticity profiles for successive stellar mass bins. (b) Ellipticity profiles for each of the stellar mass bins divided according to concentration. Solid lines and dashed lines indicated low ($C < 2.6$) and high ($C > 2.6$) concentration galaxies respectively. The vertical dashed line indicates the maximum radius affected by the PSF.
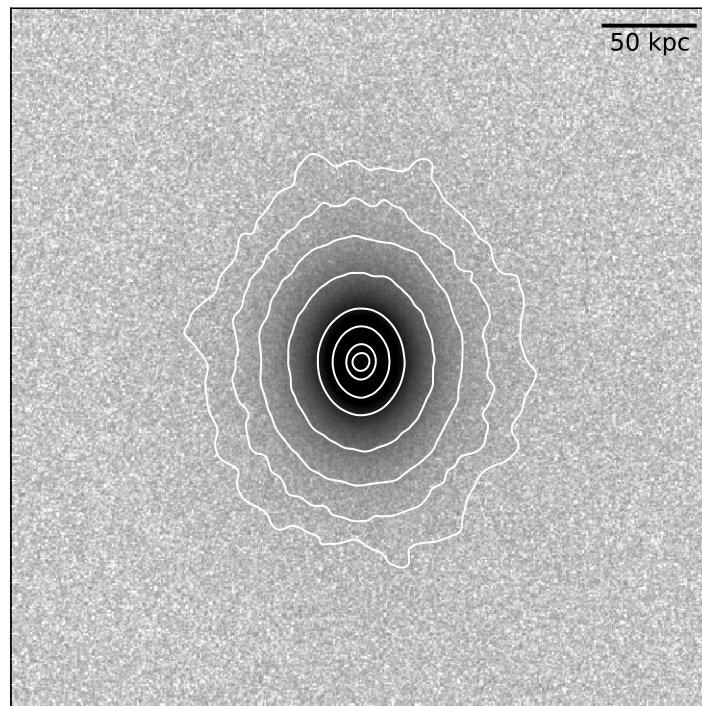
Figure 2.4: The stacked image consisting of 4040 images in the mass range $10^{11.0} M_\odot < M_* < 10^{11.4} M_\odot$ and $C > 2.6$. Elliptical contours are drawn at 5, 10, 20, 30, 50, 70, 90 and 110 kpc.
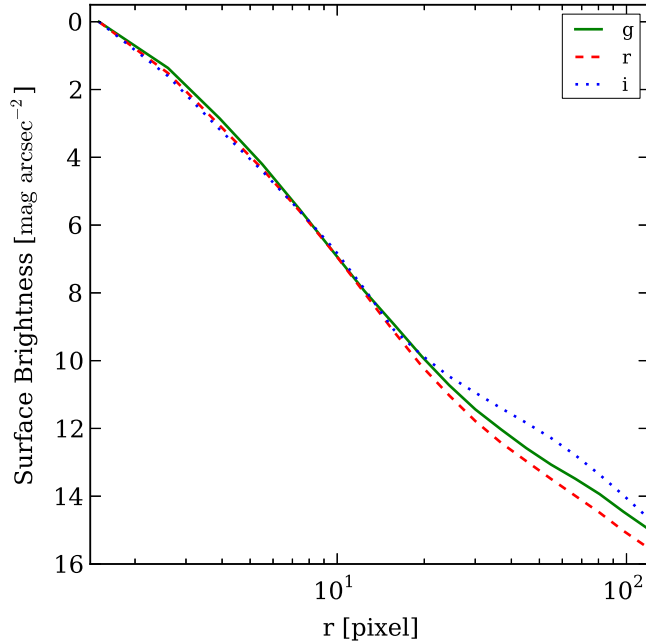
Figure 2.5: SDSS Point Spread Functions colour coded for the g, r and i bands as indicated by the legend.

account for the difference in the extended wings of the PSF, especially in the i-band, can lead to a reddening of the colour of the stellar halo (de Jong, 2008). This is very visible along the minor axis of edge-on disk galaxies where the surface brightness decreases faster than the profile of the wings of the PSF.

We choose not to deconvolve the stacked galaxy profiles. The effect of the PSF is much smaller in our work than that of Tal & van Dokkum (2011) due to the fact that the galaxies are much closer in redshift. For data interpretation purposes, we will model the two-dimensional stacked image of the galaxy convolved with the average PSF. We have thus constructed average PSF stacks in the g, r and i bands by combining the synthetic PSFs created using Robert Lupton's Read Atlas Images code[3] and stacked bright star images according to the procedure outlined in Tal & van Dokkum (2011). The PSF profiles for the g, r and i bands are shown in Figure 2.5.

Due to the fact that the PSFs in the g and in the r bands are similar (see also Fig 2 of de Jong 2008 as well as Fig 6 of Bergvall et al. 2010), our g-r colour profiles are not significantly affected by PSF effects, especially in the outer parts of the profiles. We investigate this further in Appendix A.3. However, the i-band PSF does differ significantly (see Figure 2.5) in having wings that extend to much larger distances. We therefore avoid the use of the SDSS i-band.

---

[3]http://www.sdss.org/DR7/products/images/read_psf.html

2.3.5   Ellipticity, Surface Brightness and Colour Profiles

Measuring the ellipticity can help quantify the shape of the average stellar halo. The standard `ELLIPSE` task from the `STSDAS` package in `IRAF` performs poorly at low S/N regions especially in the outer parts of the stellar halo. For this reason, the ellipticity profiles $(1-b/a)$ for each of the aligned galaxy stacks are determined by generating intensity contours at various distances from the centre of the stacked image of the galaxies in the r-band after appropriate smoothing. For deriving contours which were greater than 20 pixels away from the centre of the galaxy stack, we smooth the image with a Gaussian filter with a width of 3 pixels. For contours beyond 60 pixels from the centre of the galaxy stack, we smooth the image with a larger Gaussian filter (width of 5 pixels).

In Figure 2.3, we plot ellipticity profiles out to radii of 30-50 kpc for our stacks divided according to stellar mass and concentration. Information on the shape of stellar haloes can be inferred from the average ellipticity profiles for each stack. Only the inner part $(< 10 \, \text{kpc})$ of the ellipticity profile is significantly affected by the PSF. The outer parts of the ellipticity profile show a gradual change in ellipticity with radius. The ellipticity profile of the stacks of lower stellar mass decreases as the radius increases, i.e. for these galaxies the outer part of the stellar halo is more circular than the inner part of the galaxy. The ellipticity of the outer part of the stellar halo increases as a function of M_*. The highest stellar mass bins have a maximum outer ellipticity of ~ 0.17, which remains approximately constant from 30 to 50 kpc.

In Figure 2.4, we show the stacked image of high concentration galaxies stacked in the mass range $10^{11.0} M_\odot < M_* < 10^{11.4} M_\odot$ along with elliptical contours drawn at various radii.

We find that the stellar haloes of low concentration galaxies tend to be spherical, while the stellar haloes of high concentration galaxies tend to be elliptical. The peak in the ellipticity profiles of low-concentration galaxies at ~ 15 kpc may be due to the combined effect of stacking disk galaxies at varying inclinations. At fixed mass, the ellipticity of the highest stellar mass, high concentration galaxies reaches values of 0.2 and is approximately constant from 20 to 100 kpc. By contrast, the measured ellipticity $(1 - b/a)$ of low concentration galaxies is around 0.1.

Are these results consistent with other measurements? The stellar halo of M31 can easily be measured out to large distances and is found to be nearly spherical (Ibata et al., 2014). At 80 kpc for high concentration high stellar mass galaxies, the measured ellipticity is 0.21 ± 0.08. This is also consistent with the ellipticity of the stellar halo of LRGs measured by Tal & van Dokkum (2011) which lies around $\sim 0.25 - 0.3$. On the other hand, Sesar (2011) measured the axial ratio of the Milky Way stellar halo out to a distance of 35 kpc and estimated it as $q \sim 0.7$, i.e. an ellipticity of 0.3, which lies outside the range spanned by our estimates. This may imply that the Milky Way's halo is unusual. Huang et al. (2013) have also found that the outer parts of nearby elliptical galaxies is higher than the inner parts of the galaxy.

We note, however, that when stacking aligned galaxies together, we assume that the outer stellar halo is also aligned with the shape of the galaxy. If this were not the case, it

would lead to a systematic uncertainty in the intrinsic ellipticity which would increase with radius. As a result, the ellipticity measured is a lower limit on the true average intrinsic ellipticities of the stellar haloes of the galaxies which make up the stack. Convolving the stacked images creates additional measurement uncertainties.

Using these ellipticity profiles, we derive surface brightness in the r band and g-r colour profiles in elliptical annuli after background subtraction.

At radii where the ellipticity estimates are no longer reliable, we assume that the ellipticity profile flattens out at the furthermost determined value of the ellipticity.

2.4   Analysis of Stacked Images

2.4.1   Profiles in Stellar Mass Bins

In Figure 2.6, we show the average surface brightness profiles and the average g-r colour profiles for our galaxy stacks in stellar mass bins. The surface brightness profiles extend reliably to a depth of $\mu_r \sim 32$ mag arcsec^{-2}. The profiles of highest mass bins reach out to 100-150 kpc, while the lower mass bins extend up to 60-100 kpc. The surface brightness profile of the stellar halo show variations with stellar mass. As discussed in Cooper et al. (2013), the trend in the surface brightness profiles in the stellar mass range $10^{10.7} M_\odot < M_* < 10^{11.4} M_\odot$ is consistent with the theoretical predictions. In this paper, we extend the analysis down to $10^{10} M_\odot$; comparison with model predictions will form the subject of a future paper.

The triangle markers in the colour profiles indicate the average $R50$ (the radius enclosing 50 per cent of the Petrosian r-band luminosity of the galaxy) for each mass bin. For each mass bin, there is a flattening in the colour profile and a hint of an upturn beyond the average $R50$ indicating that we may be seeing the effects of an older accreted component. We will quantify this in more detail in the next section.

2.4.2   Profiles in Stellar Mass Bins divided by Concentration

In Figure 2.7, we show the average surface brightness profile and the average g-r colour profiles for our galaxy stacks separated into high ($C > 2.6$) and low ($C < 2.6$) concentration galaxies.

The surface brightness profiles reveal a clear difference in the shapes of the stellar haloes of high concentration and low concentration galaxies. We can parametrise the shape of the stellar halo by measuring its outer slope. The outer slope is measured through a Bayesian methodology that takes into consideration the scatter due to the variance of the shape of the surface brightness profile of the galaxy. The details are outlined in Appendix A.2.

In Figure 2.8, we plot the slope $\Gamma = d(\log_{10} I)/d(\log_{10} R)$ beyond 25 kpc of the surface brightness profile as a function of stellar mass and galaxy type. At these radii, the surface brightness profiles are not significantly affected by the PSF. The error bars include the variance of the shape of the surface brightness profile of the galaxies in the stack estimated
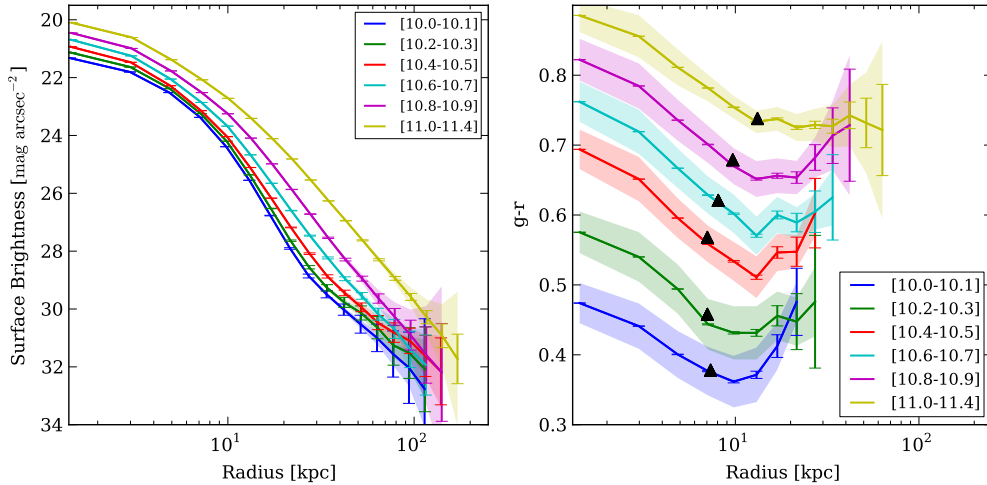
Figure 2.6:   Surface brightness profiles and *g-r* colour profiles of stacks for successive stellar mass bins. The error-bars show the sum of instrumental errors and uncertainty in background subtraction, while the shaded regions show the spread due to the variation in the shape of the stellar halo. The triangles in the colour profiles mark the average R50 of galaxies in the respective bin.

through bootstrapping. For low concentration galaxies, the outer slope steepens from $\Gamma \sim -2.5$ at low stellar masses to $\Gamma \sim -4.4$ at higher stellar masses. For high concentration galaxies, the outer slope steepens from $\Gamma \sim -2.3$ at low stellar masses to $\Gamma \sim -3$ at higher stellar masses. At fixed mass, the outer slopes of the profiles of low concentration galaxies are steeper than those of high concentration galaxies. The variance in the slope is much larger for low concentration than high concentration galaxies. Similarly the variance in the slope is much larger for low-mass than high-mass galaxies.

Ibata et al. (2014) analyze the power-law slope of the two-dimensional projected distribution of star counts in M31 and find $\Gamma = -2.30 \pm 0.02$. We again caution the reader that in stacking large number of galaxies together with different concentrations, the resulting outer slope is a linear combination of the outer slopes of the individual galaxies which go into the stack, so our results are not directly comparable to those obtained for individual galaxies.

2.4.3   Colour Profiles as a function of Stellar Mass and Concentration

The *g-r* colour profiles extend out to 15-35 kpc for low concentration galaxies and up to 40-70 kpc for high concentration galaxies. There also appears to be a clear separation between the inner ($R < 10\,\mathrm{kpc}$) colour profiles, where *g-r* decreases as a function of radius, to a region where colour remains more constant. This is seen for both low and high concentration galaxies. Low concentration galaxies show steeper inner colour gradients
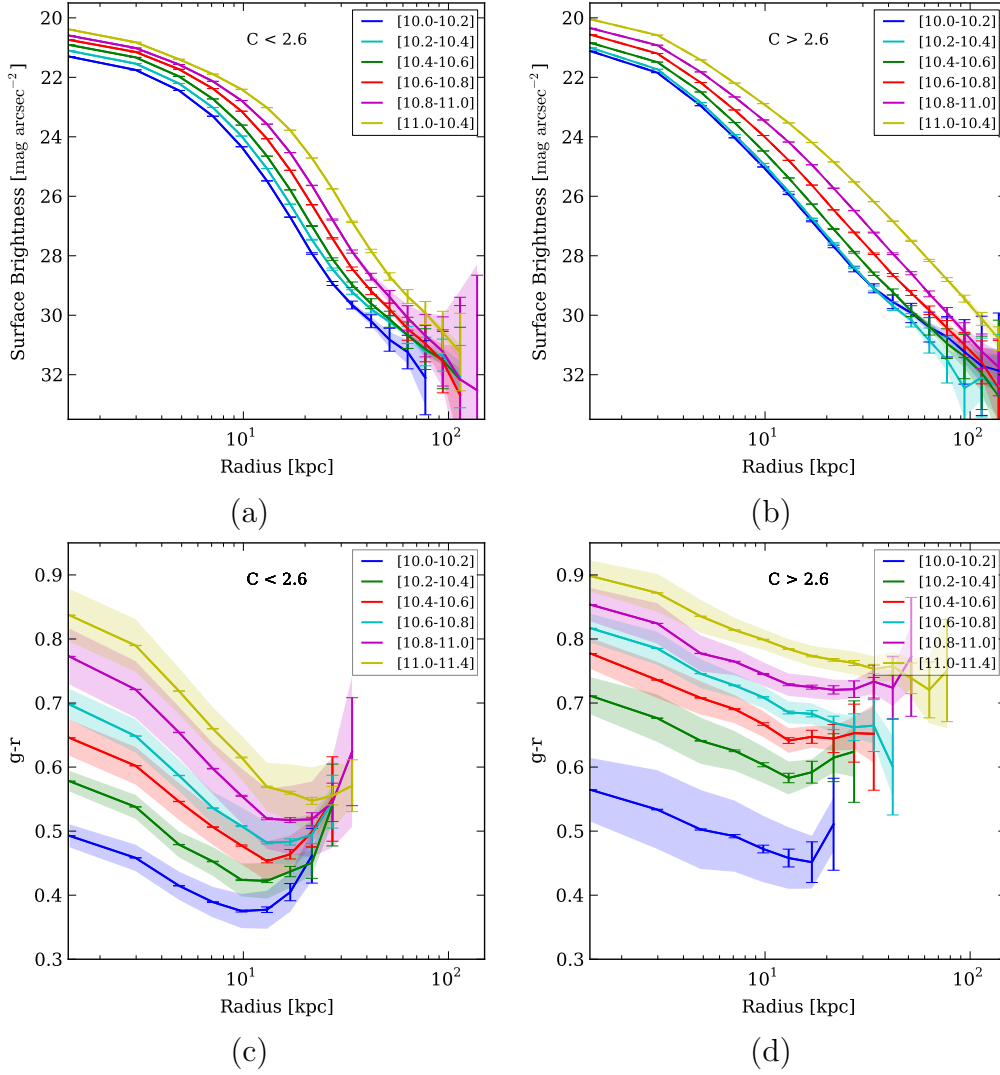
Figure 2.7:   Surface brightness and *g-r* colour profiles of the stellar mass bins divided according to concentration. The error-bars show the sum of the instrumental errors and the uncertainty in background subtraction, while the shaded regions show the spread due to the variation in the shape of the stellar halo.
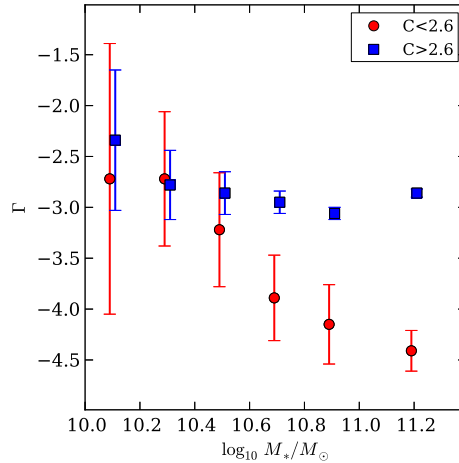
Figure 2.8: The slope $\Gamma = d(\log_{10} I)/d(\log_{10} R)$ of the surface brightness profile beyond 25 kpc. Blue represents high concentration galaxies, while red represents low concentration galaxies. The errors represent the total variance in the slope of the surface brightness profile estimated from bootsrapping the samples in the stack.

than high concentration galaxies. The colour gradient is also steeper in low concentration galaxies with high stellar masses than in low concentration galaxies with low masses (See also Gonzalez-Perez, Castander & Kauffmann 2011, Tortora et al. 2010 and Suh et al. 2010).

For low concentration galaxies, there appears to be a minimum in the g-r colour beyond which the colour profiles redden. This minimum occurs between 10 kpc for low mass galaxies and 20 kpc for higher mass systems. For high concentration galaxies, the colour profiles flatten, but do not exhibit a pronounced upturn. This is consistent with the flattening in colour profiles detected in LRGs (Tal & van Dokkum, 2011). Reddening of the colour profile at large radii cannot be attributed either to the difference in the PSF in the g and r bands or due to the errors in the background subtraction. We investigate this further in Appendix A.3.

La Barbera et al. (2012) have derived median-stacked colour profiles of early-type galaxies from SDSS. In particular, their g-r colour profile can be directly compared to our g-r colour profile for high mass high concentration galaxies. Both the colour profiles are consistent with each other within error bars. In particular there is excellent agreement in the outer part. Our g-r colour profiles are redder by 0.05 mag at the center of the galaxy stack. This can be attributed to the effect of the PSF at the center of the galaxy stack (See Appendix A.3).

The colour profiles of low concentration galaxies do not probe the area where the stellar halo becomes dominant. Bakos et al. (2008) have shown that 90% of the light profiles of the disks of late-type galaxies exhibit deviations from a pure exponential either as truncations (60%) or as anti-truncations (30%). The colour profiles of disks with truncations are "U-shaped". Disks with anti-truncations exhibit a plateau in g-r colour at large radii.
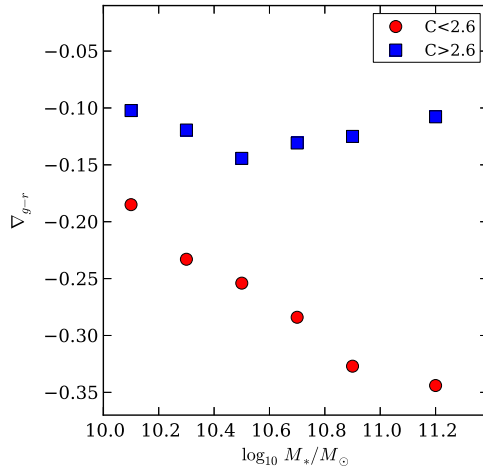
Figure 2.9: The gradient in the g-r colour profile, $\nabla_{g-r} = \frac{\Delta(g-r)}{\Delta(\log_{10} R)}$, measured along the path of the steepest descent for low concentration galaxies interior to the radius where the profile exhbits an upturn, and for high concentration galaxies interior radius where the colour profile flattens.

When stacking a large number of low concentration galaxies together containing with a minimum or a flattening in the g-r colour profile, the combined effect results in behaviour intermediate between the two. Deeper data is required to probe the colours of stellar populations in the stellar halo. Monachesi et al. (2013) detect a flattening of the colour profile of the stellar halo of M81.

The presence of bluer colours in the outer end of both low and high concentration galaxies as compared to the centre of the galaxy may indicate the presence of stars with significantly younger populations in these outer parts. However, it will be difficult to confirm this without being able to break the degeneracy between age and metallicity by using colours that involve either the i or z bands.

We plot the g-r colour gradient $\nabla_{g-r} = \frac{\Delta(g-r)}{\Delta(\log R)}$ for our galaxy stacks in Figure 2.9. For low concentration galaxies, we evaluate the slope for the path of the steepest descent interior to the minimum in the g-r colour profile. For high concentration galaxies, the slope is derived for the steepest descent interior to the point where the g-r colour profile flattens. Since the colour profile is affected by the PSF at the centre of the galaxy stack, the analysis is restricted to radii beyond 3 kpc. The gradient is first evaluated from 3 kpc right up to the minimum in the g-r colour profile, and the path length over which the gradient is calculated is decreased step-by-step until the gradient reaches its maximum. Figure 2.9 shows that colour gradients are stronger in late-type galaxies than in early-type galaxies. In early-type galaxies, the gradients do not depend on stellar mass, but in late-type galaxies, high mass galaxies have much steeper gradients than low mass galaxies.

2.5   Multi-Component Modelling of the Galaxy Stacks

For each stacked image, we model the full two dimensional r-band intensity distribution of the galaxy stack using multi-component Sérsic models. We are particularly interested in modelling the outer stellar halo light of the galaxy and in placing constraints on the amount of accreted stellar material. We are confident that the depth of our stacked images means that we can reach out into the extended stellar halo of the galaxy. Theoretical considerations indicate that there should be an inflexion or a change in the surface brightness profile of the galaxy where the accreted stellar component begins to dominate (Cooper et al., 2013).

The Sérsic (1968) profile $\log I(r) \propto r^{1/n}$ is the most versatile among the models and is traditionally used to fit the surface brightness profile of galaxies. The Sérsic profile reduces to an exponential ($n = 1$) profile for disk galaxies, while $n = 4$ profiles (de Vaucouleurs, 1948) has been used to model bulges and ellipticals. Kormendy et al. (2009) have demonstrated that the Sérsic profile fits elliptical galaxies and spheroidals very well over a large dynamic range in radius. They also suggested that departures from these profiles could provide new insights into galaxy formation. In this paper, we leave aside the issue of departures from the Sérsic profile at small radii in our galaxy stacks. Our aim is to explore our ansatz that the excess light (deviations from the single Sérsic profile) detected at large radii ($R > 20\,\mathrm{kpc}$) is indicative of additional components in the galaxy, which may be attributed to accreted stellar material. Our second ansatz is that the radial variation of ellipticity can also be indicative of various galaxy formation processes. In particular, the difference in ellipticity between the inner part of the galaxy and the outer stellar halo of the galaxy may yield clues to the origin of these components.

Deviations from simple profiles at large radii and the radial variation in ellipticity can be adequately modelled through multi-component modelling, where each component can be represented by a Sérsic profile with a fixed ellipticity. The flexibility of the Sérsic profile helps us model a large variety of possible profiles. The real challenge of modelling galaxies is in assigning a physical significance to each of these components. In fitting multiple components to our galaxy stacks, we are motivated by the results of Cooper et al. (2013) who have demonstrated theoretically from particle-tagging methods that the in-situ and the accreted surface density profiles are well fit by Sérsic (1968) functions, while the total profile is best fit by a sum of these two functions.

Such an approach have been attempted previously for nearby galaxies. In particular, Huang et al. (2013) and Mosleh et al. (2013) have recently showed for nearby galaxies that multi-component Sérsic models are needed to model the two dimensional intensity distribution of galaxies. Huang et al. (2013) decomposed nearby elliptical galaxies into three sub-components: a compact ($R_e < 1\,\mathrm{kpc}$) inner component, an intermediate-scale ($R_e \sim 2.5\,\mathrm{kpc}$) middle component, and a dominant extended ($R_e \sim 10\,\mathrm{kpc}$) outer envelope.

We seek to model the two-dimensional intensity profile of the galaxy with a minimum number of components through a Bayesian technique following Yoon et al. (2011). In the following subsections, we model separately the stacks of high concentration and low concentration galaxies. We first show that a single component is not sufficient to model

the surface brightness profile of high concentration galaxies. We demonstrate how the surface brightness profile of high concentration galaxies can be successfully modelled by two components. For low concentration galaxies, we show that we may need three components to model the disk breaks of galaxies in addition to the stellar halo. For all our fitting procedures, we use the full two-dimensional information in the stacked image. We also test our modelling on mock images of high and low concentration galaxies.

2.5.1 High Concentration Galaxy Stacks

High concentration galaxies are simpler to model than low concentration galaxies. Motivated by this, we first fit a single two-dimensional Sérsic model with a fixed ellipticity to our high concentration galaxy stack:

$$I(R) = I_e \exp\left\{-b_n\left(\left(\frac{R(q)}{R_e}\right)^{1/n} - 1\right)\right\}, \qquad (2.1)$$

where I_e is the intensity at the effective radius R_e that encloses half of the total light from the model and n is the Sérsic index. The constant b_n is defined in terms of the Sérsic index. The radial distance, R, is a function of the Cartesian coordinates and the ellipticity q of the model. We also model an additional constant sky component. A single Sérsic model so defined has a total of 4 free parameters.

We compare this with a double Sérsic model with a common centre and with different ellipticities for each Sérsic component. Sérsic profiles extend out to infinity. In order to ensure that the outer stellar halo is determined by only one component, we smoothly cut off the inner Sérsic profile at large radii: the surface brightness profile is suppressed beyond $7\,R_{eff}$ and drops to zero outside $8\,R_{eff}$.[4] With an additional constant sky component (c), the double Sérsic model has a total of 9 free parameters. There are two additional free parameters for the centre of each model. To reduce the number of free parameters, we determine and fix the centre of the galaxy stack by fitting a single Sérsic model with variable parameters for the centre. All the models considered are symmetric along the major axis and the minor axis. The asymmetries in the image (in the form of bars, bulges, disks, pseudo-bulges, etc.) are not explicitly modelled and appear as residuals. The parameters of the double Sérsic model are summarized in 2.1.

For the fitting procedure, each model was convolved with the average stacked SDSS PSF before fitting (see section 2.3.4). We employ a Bayesian technique with uniform and physical priors for all the parameters θ (I_e : 0–1 nanomaggies arcsec^{-2}; R_e : 1–100 pixels; n : 0–10; c : 0–1 nanomaggies arcsec^{-2}; q : $0 - 10$).

Applying Bayes' theorem, we can find the posterior probability distribution over the parameters θ as

$$p(\theta \mid \mathbf{D}) = \frac{p(\mathbf{D} \mid \theta)}{\int_\theta p(\mathbf{D} \mid \theta)p(\theta)\,d\theta} \cdot p(\theta), \qquad (2.2)$$

---

[4]The same procedure is followed in SDSS for pure de Vaucouleurs profile to calculate `ModelMag`.

where $\int_\theta p(\mathbf{D} \mid \theta) p(\theta) \, d\theta$ is the model evidence and $\mathbf{D}$ is the data.

$p(\mathbf{D} \mid \theta)$ is the likelihood which can be constructed as follows:

$$\log(L) = -\frac{1}{2}\log((2\pi)^k \Sigma) - \frac{1}{2}(\mathbf{D} - \mu(\theta))^\mathrm{T} \Sigma^{-1}(\mathbf{D} - \mu(\theta)), \tag{2.3}$$

where Σ is the covariance matrix (which is diagonal in this case), $\mathbf{D}$ is the stacked data, μ is the model as a function of the parameters θ and k is the number of independent pixels.

We use MULTINEST (Feroz, Hobson & Bridges, 2008; Feroz et al., 2013), a Bayesian inference tool on the full stacked image. This has the advantage over Galfit (Peng et al., 2010) in that it can explore the complete parameter space. We use the full image 950×950 pixels for the fitting procedure. This is essential for a proper determination of the residual sky component in the stacked images. In general, the determination of the outer Sérsic index is correlated with the sky component.

We generate a full posterior probability distribution function (PDF) of all the parameters using MULTINEST. This allows us to evaluate the degeneracies in the parameters. If the posterior PDF is double modal (i.e., contains two maxima), we choose the most physical model such that the effective intensity (I_e) / effective radius (R_e) of the inner most component should be larger/smaller than that of the outer component. For the final parameters of the model, we use the mean values of the posterior PDF. These mean values automatically encode information on the parameter degeneracies.

To compare the various models with each other, we can use two approaches. The first involves using the Bayesian "evidence" marginalised over the model parameters for model comparison. This compares models on a global scale. On the other hand, comparing residuals (or the reduced chi-square) in specific regions of the stacked image allows one to judge the goodness of fit for specific components of the galaxy stack including the stellar halo.

To compare models globally, we construct the Bayes factor (B_{10} - hypothesis 1 over hypothesis 0). Kass and Raferty (1995, Journal of American Statistical Association) suggest comparing $2\log_e(B_{10})$ and note that a factor > 10 is indicative of strong evidence against hypothesis 0. The square root of $2\log_e(B_{10})$ gives us the level of significance between the two models. We compare the factor $2\log_e(B_{D/S})$ which is comparing the double Sérsic model over the single Sérsic model for a range of mass bins in Table 2.2. In Figure 2.12, we show how well the double Sérsic model fits the surface brightness profiles for a range of stellar mass bins.

In Figure 2.10, we compare the single-Sérsic and double-Sérsic models for the high concentration galaxy stack in the highest stellar mass bin $10^{11.0} M_\odot < M_* < 10^{11.4} M_\odot$. The single-Sérsic function fits the symmetric central high S/N part of the surface brightness profile up to a surface brightness of $\mu_r \sim 27\,\mathrm{mag\,arcsec}^{-2}$ reaching out to 30 kpc. Note that all internal galaxy components (e.g. bulges, disks, pseudo-bulges) are averaged out and incorporated into the single-Sérsic fit. Beyond 30 kpc, excess light is detected. The double-Sérsic profile on the other hand provides an excellent fit up to a depth of $\mu_r \sim 32\,\mathrm{mag\,arcsec}^{-2}$ reaching out to 130 kpc. The residuals are shown in the panel below in Figure 2.10. The residuals of the double-Sérsic are less than $0.2\,\mathrm{mag\,arcsec}^{-2}$ across

Table 2.1: Parameters of the Double Sérsic Model

Double Sérsic	
n1	Inner Sérsic Index
r1	Inner Effective Radius
i1	Inner Effective Intensity
q1	Inner Ellipticity
c	Residual Sky value
n2	Outer Sérsic Index
r2	Outer Effective Radius
i2	Outer Effective Intensity
q2	Outer Ellipticity

Table 2.2: We compare the double-Sérsic model with the single-Sérsic model by comparing $2\log_e(B_{D/S})$, where $B_{D/S}$ is the Bayes factor favouring the double-Sérsic model over the single-Sérsic model

Mass bin	$2\log_e(B_{D/S})$
10.0-10.2	3713
10.2-10.4	9779
10.4-10.6	23508
10.6-10.8	30831
10.8-11.0	21730
11.0-11.4	18727
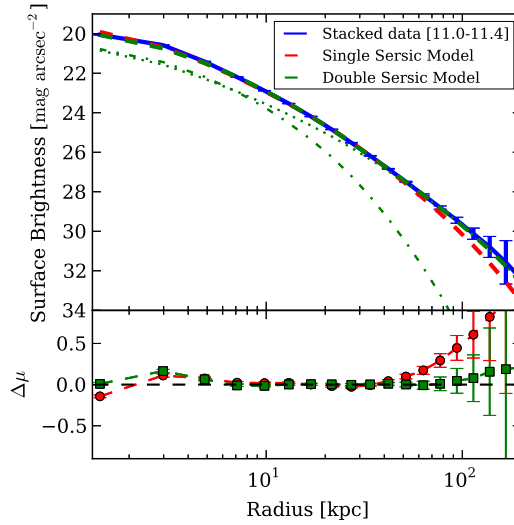
Figure 2.10: Comparison of the the double-Sérsic (dashed green) and the single-Sérsic (dashed red) models with the surface brightness profile of the high concentration highest stellar mass bin stack $C > 2.6, 10^{11.0} M_\odot < M_* < 10^{11.4} M_\odot$). For the double-Sérsic model, the internal component is denoted by the dot-dashed line while the outer component is denoted by the dotted line.

the whole radial range (0-120 kpc) of the galaxy stack. The residuals at the centre are attributed to the asymmetric part of the intensity distribution at centre of the galaxy stack due to the various internal galaxy components mentioned above. The PDFs and the correlations between the various parameters of the double Sérsic model for the high concentration highest stellar mass bin stack $(C > 2.6, 10^{11.0} M_\odot < M_* < 10^{11.4} M_\odot)$ are shown in Figure 2.11.

We find that the double-Sérsic profile provides a much better fit for all high concentration galaxies across all mass bin ranges. This can be seen visually by calculating and comparing the residuals of the image beyond 20 kpc for each model. Significant deviations are only seen in the lower two mass bins. The fits to the lowest mass bin is not perfect due to limited number of galaxy images ($\sim$ 1212) which went into the stack. At first glance, our conclusion that a double-Sérsic profile is *always* required may seem surprising, because the surface brightness profiles of massive galaxies with high concentration do not exhibit a clear inflexion point. We note that a single-Sérsic model has a single fixed ellipticity, while the double-Sérsic model with different ellipticities for each component can in a limited way mimic the varying ellipticity of the stacked galaxy image. We investigated whether the change in ellipticity is the dominant factor that favours a double-Sérsic profile over a single-Sérsic profile. To test this, we compare a single-Sérsic and a double-Sérsic profile fitted to similar stacks of galaxies which are not aligned but are randomly oriented. In all cases, the double-Sérsic is still preferred over the single-Sérsic profile. The factor $2 \log_e(B_{D/S})$ in the randomly oriented case is reduced to one-third of that as calculated in Table 2.2. This indicates that it is both the surface brightness profile and the ellipticity
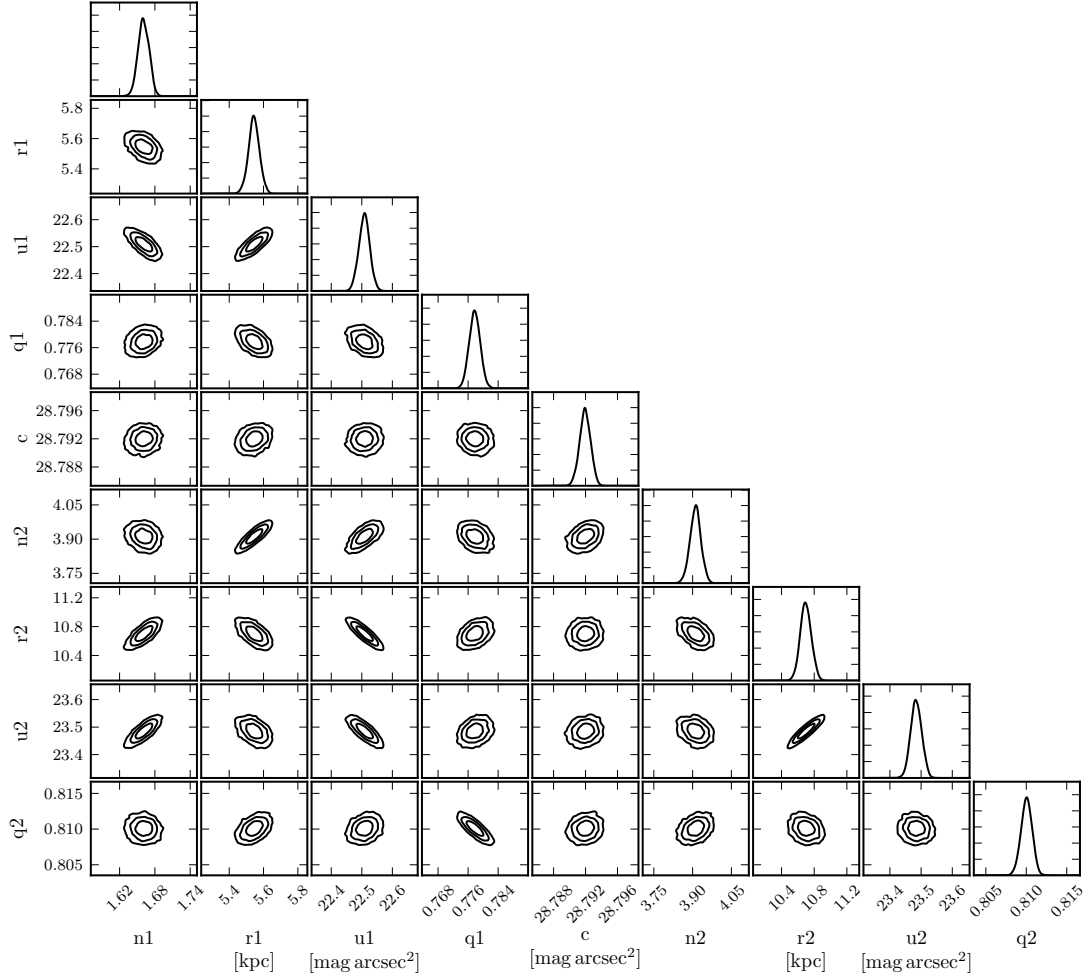
Figure 2.11: The probability density function (PDF) and the correlations between the various parameters of the double Sérsic model (see Table 2.1) for the high concentration highest stellar mass bin stack ($C > 2.6, 10^{11.0} M_\odot < M_* < 10^{11.4} M_\odot$). The effective intensity and the residual sky value are expressed in units of $\mathrm{mag\,arcsec^{-2}}$.
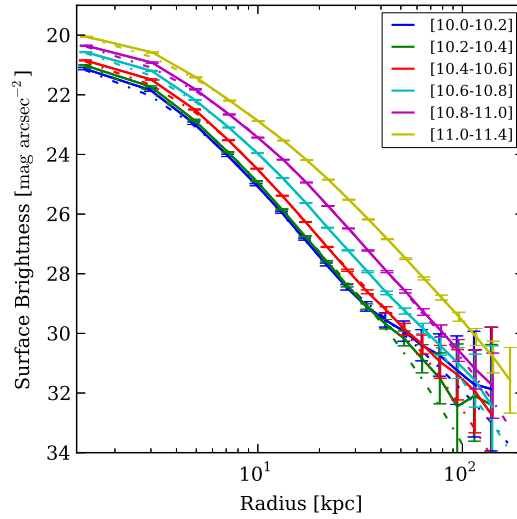
Figure 2.12: We compare the surface brightness profiles of the high-concentration galaxy stacks with their corresponding double-Sérsic models.

which contribute to favour a double-Sérsic profile over a single-Sérsic profile.

Plots of the Sérsic indices of the two components as a function of mass are shown in in Figure 2.13. The outer Sérsic index increases with the mass of the galaxy stack from $n \sim 3$ to $n \sim 4$. The effective radii of each component are also denoted in the Figure 2.13. The effective radius of the outer component scales as $\propto 2.5 \log_{10} M_*$ reaching a maximum of 9 kpc for the highest mass bins. We note that the inner Sérsic component is always more elliptical than the outer Sérsic component. On the other hand, the inner ellipticity profiles derived in Figure 2.3 are significantly affected by the PSF. The ellipticity of the inner component is approximately constant for all mass bins while the ellipticity of the outer component increases as mass increases.

Having separated the light from the galaxy into two components, we study the variation of the light in the two components as a function of stellar mass. We can also calculate the fraction of light in the outer Sérsic component (Figure 2.14). We will discuss this result in Section 2.7.

2.5.2 Low Concentration Galaxy Stacks

Modelling low concentration galaxies along with their stellar halo component remains a challenging task, because of the extremely low fraction of light in the stellar halo in these systems. Estimates of the stellar halo contribution for M31 lie between 0.6 and 1.5 percent (Ibata et al., 2014), while those for the Milky Way lie between 0.3 and 1.0 percent (Bell et al., 2003; McMillan, 2011). Previous modelling and estimates of the stellar halo content of disk galaxies have been made from star counts. In order to detect the stellar halo in face-on disk galaxies, deep imaging is necessary with an accurate determination of the background residuals. Recently van Dokkum et al. (2014) tried to model and determine the stellar halo
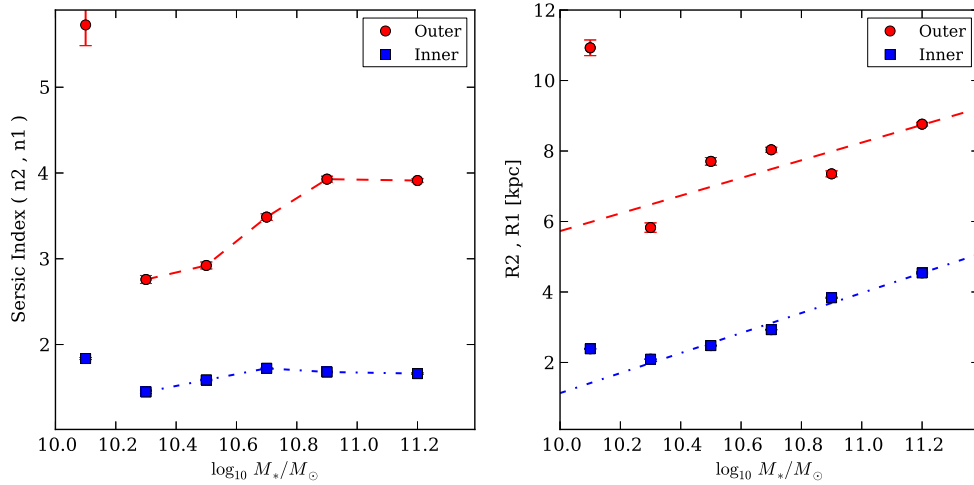
Figure 2.13: (a) The Sérsic indices of the inner(blue) and outer(red) components for high concentration galaxies. (b) The effective radii of the inner(blue) and outer(red) Sérsic components for high concentration galaxies. The outer effective radius scales as $\propto 2.5 \log_{10} M_*$ while the inner effective radius scales as $\propto 2.8 \log_{10} M_*$. The model fails to fit for the lowest mass bin because of insufficient numbers in the stack.
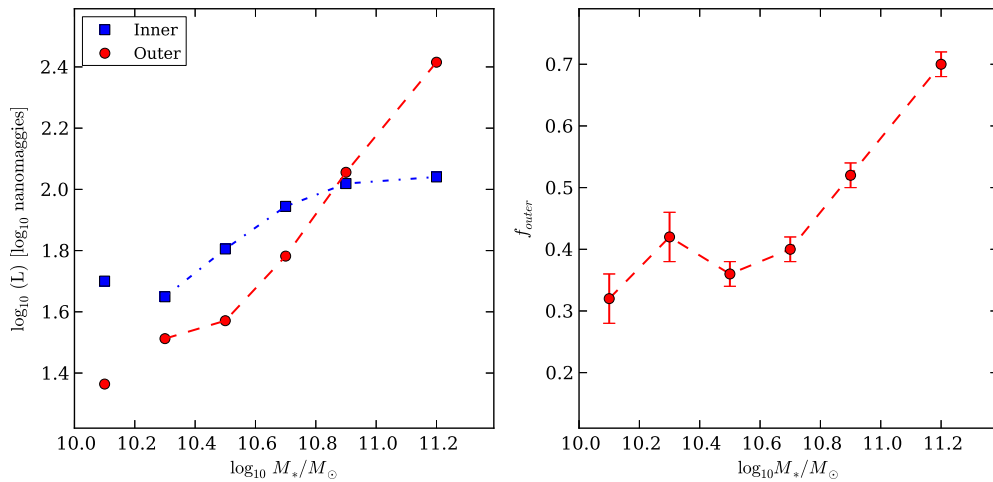
Figure 2.14: (a) The $\log_{10}$ of the r-band total Luminosity (in nanomaggies) in the inner(blue) and outer(red) components as a function of stellar mass for high concentration galaxies. (b) The fraction of light in the outer Sérsic component as function of stellar mass for high concentration galaxies.
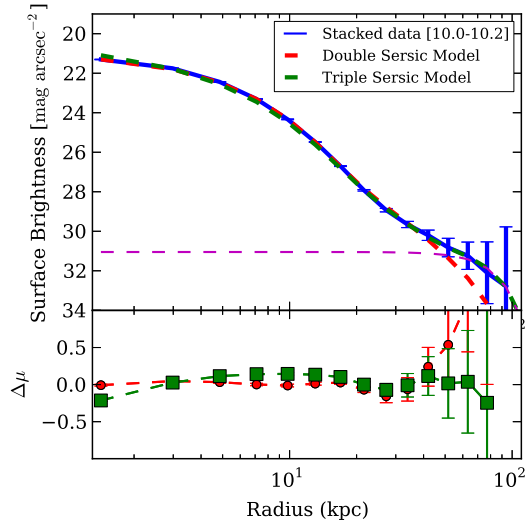
Figure 2.15: The double Sérsic model (shown in red) provides an inadequate fit to low concentration ($C < 2.6$) low mass galaxies ($10^{10.0} M_\odot < M_* < 10^{10.2} M_\odot$) The triple Sérsic model provides a much better fit (shown in green). The third component of the triple Sérsic model is shown in a dashed magenta line. In the bottom panel, the residuals of the double Sérsic model and the triple Sérsic model are shown.

content of the massive spiral galaxy M101 from integrated surface brightness profiles by going to a depth of $\mu_g \sim 32\, \mathrm{mag\, arcsec^{-2}}$. The effective depths of our stacked images are similar to this.

Another important issue is that disk breaks in galaxies (Bakos et al., 2008) also cause inflections in the surface brightness profile of the stacked galaxies and need to be modelled. We find that a double-Sérsic model often fails to fit the stacks of low concentration galaxies, as is shown in Figure 2.15. In these galaxies, the inflection is caused by disk breaks and these breaks can occur very close to where the stellar halo becomes dominant. This inflection cannot be caused

A natural extension of our modelling procedure would be to use a concentric triple Sérsic model. However, the general triple Sérsic model is highly degenerate, especially when trying to separate components which are not easily distinguishable from each other. Face-on disk galaxies with a low stellar-halo mass fraction occupy only a limited parameter space of a three component model. To break these degeneracies, we truncate the inner two components (beyond $7 - 8\, R_e$) and apply restrictions to the third component of the triple Sérsic model. In particular, we look for 3rd component solutions that involve a low Sérsic index ($n3 < 1.5$), lower effective intensity (in comparison to the other 2 components) and a larger effective radius ($R_{eff} > 15\, \mathrm{kpc}$) for the outer-most component. The low Sérsic index ensures that the profile of the third outer component does not rise steeply and dominate the inner central parts of the galaxy. The parameters of the triple Sérsic model are summarized in Table 2.3.

We also modify our fitting algorithm as follows. We do not fit three components at the

Table 2.3: Parameters of the Triple Sérsic Model

Triple Sérsic	
n1	Inner Sérsic Index
r1	Inner Effective Radius
i1	Inner Effective Intensity
q1	Inner Ellipticity
c	Residual Sky value
n2	Middle Sérsic Index
r2	Middle Effective Radius
i2	Middle Effective Intensity
q2	Middle Ellipticity
n3	Outer Sérsic Index
r3	Outer Effective Radius
i3	Outer Effective Intensity
q3	Outer Ellipticity

same time. We first model independently the galactic disk along with the disk break in high S/N part of the stacked image with a truncated double Sérsic model. Later, having fixed the two components describing the internal part of the galaxy, we add a third component to model the outer extra light. This is necessary because the S/N of the light of the outer image is so much lower than that of the inner regions. If the disk break occurs close to the where the stellar halo becomes dominant (i.e., if the stellar halo fraction is not negligible), we first model the internal two components with a truncated double Sérsic model. Then keeping the innermost component fixed, we model the disk break and the extra stellar halo light by fitting two additional Sérsic components. In both methods, we determine the constant sky component at each step. The restriction of a low Sérsic index for the outer component does not significantly affect our results as the fixing of the inner component automatically reduces the value of the outer Sérsic index.

The global Bayes factor is unable to differentiate between models in the low concentration case, since it is dominated by the asymmetric component (bars, pseudo-bulges, etc.) at the centre of the stacked galaxy. In order to judge which fitting method is most appropriate for a given given galaxy stack, we subject every image stack to both methods and calculate the chi-square of the image for each pixel beyond 20 kpc. We compare the reduced chi-square for a double Sérsic model, as well as both methods for determining the third component of the triple Sérsic model, and choose the best fit model. In Figure 2.16, we compare the residuals of the double Sérsic model as well as the two methods for determining the components of the triple Sérsic model for disk galaxies stacked in the mass bin range $10^{10.2} M_\odot < M_* < 10^{10.4} M_\odot$, with concentration index $C < 2.6$. The blue band gives the average uncertainty in background removal for each pixel in nanomaggies arcsec^{-2}. The procedure which keeps the the inner most component fixed and varies the outer two
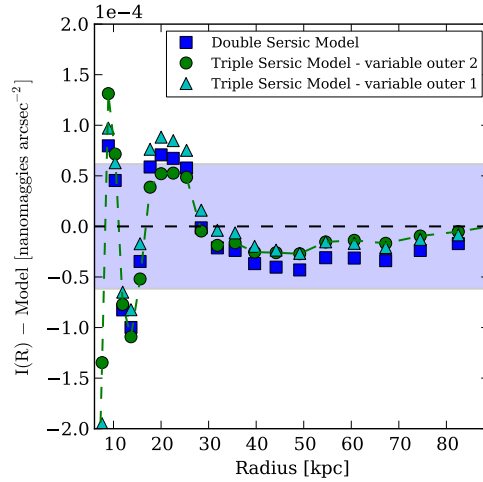
Figure 2.16: The residuals for three models: the double Sérsic, the triple Sérsic by keeping the inner most component fixed (Method A) and the triple Sérsic by keeping the inner two components fixed (Method B) for galaxies stacked in the mass bin range $10^{10.0} M_\odot < M_* < 10^{10.2} M_\odot$ and with concentration $C < 2.6$. The fraction of light of the galaxy in the outermost component by Method A is $2.3 \pm 0.4\%$ and by method B is $1.2 \pm 0.3\%$. The blue band gives the average uncertainty in the background removal for each pixel in nanomaggies arcsec^{-2}.

components fares the best. The best fit triple Sérsic model is shown in Figure 2.15.

The accuracy of modelling the third component depends upon the accuracy of the correct background sky determination. This accuracy is limited by the accuracy of our background removal. For the model fits to the stack of $N \sim 3000$ galaxy images shown in Figure 2.15, if we assume a conservative Sérsic index ($n \sim 0.4$) and an effective radius $R_e \sim 40 \, \mathrm{kpc}$ and an effective magnitude determined by the error of the background residuals ($I_e \sim 6 \times 10^{-5} \, \mathrm{nanomaggies \, arcsec}^{-2}$), the third component can be correctly determined if it is greater than 2% of the total light in the galaxy.

In Figure 2.17, we plot the fraction of the total light and stellar mass of the galaxy in the inner and outermost components. Results are shown as a function of M_* and for low and high concentration systems. For low concentration galaxies, the higher two mass bins are best fit by double Sérsic models, while the lower mass bins are best fit by triple Sérsic models. Most of the low concentration stacks which are modelled successfully by a triple-Sérsic profile are best fit by keeping only the inner-most component fixed. Only one low concentration stack ($10^{10.0} M_\odot < M_* < 10^{10.2} M_\odot$) could be best fit by fixing the inner two Sérsic components. We will discuss these results later in Section 2.7.

Improved accuracy in determining the third component may be obtained by stacking a larger number of low concentration galaxies. We stack 12,423 galaxies in the r-band with random orientations in the mass range $10^{10.0} M_\odot < M_* < 10^{10.8} M_\odot$, with a concentration $C < 2.4$ and with an isophotal axial ratio $>= 0.77$. Using our modelling procedure, we
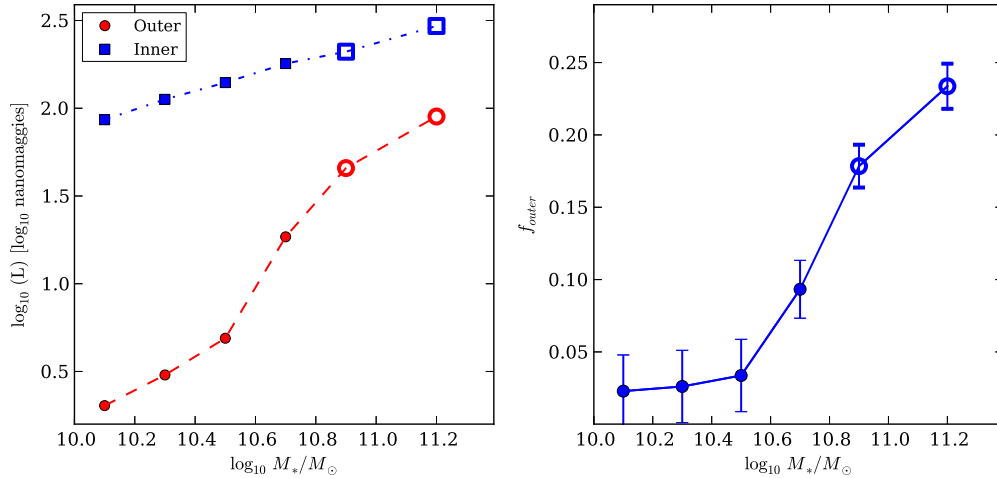
Figure 2.17: (a) The $\log_{10}$ of the r-band total luminosity (in nanomaggies) in the inner(blue) and outer-most (red) components as a function of stellar mass for low concentration galaxies. (b) The fraction of light in the outer-most Sérsic component as a function of stellar mass for low concentration galaxies. The hollow circular markers indicate that a triple Sérsic profile was required to model the outer parts of the stellar halo, while the filled circular markers indicate that a double Sérsic profile was sufficient.

can derive the probability distribution function (PDF) of the fraction of light in the third component (see Figure 2.18). This fraction is about $1.3 \pm 0.5\%$.

Our modelling allows us to identify a radius at which the outer component begins to dominate the integrated stellar light (R_{acc}). In Figure 2.19, the blue squares indicate this radius as a function of M_* for low concentration galaxies. As can be seen, this radius *decreases* as a function of the stellar mass of the galaxy from ~ 50 kpc for galaxies with stellar masses of a few times $10^{10} M_\odot$ to ~ 30 kpc for galaxies with $M_* \sim 10^{11} M_\odot$. For comparison, we also we compare R_{acc} with the radius at which the minimum occurs in the g-r colour profiles of low concentration galaxies ($R_{colour\,min}$; see Figure 2.7). The radius at which the outer material begins to dominate is much larger than the radius at which the minimum in the colour profile occurs. This accords well with suggestions in the literature that this minimum in the g-r colour profile is associated with the break radius in disk galaxies (Bakos et al., 2008).

Also in Figure 2.19, we compare the radius at which the outer material begins to dominate with the radius at which the g-r colour profile flattens for high concentration galaxies. The radius at which the g-r colour profile flattens increases as a function of stellar mass from ~ 20 kpc for galaxies with stellar masses of a few times $10^{10} M_\odot$ to ~ 40 kpc for galaxies with $M_* \sim 10^{11} M_\odot$. The radius at which the outer material begins to dominate is comparatively smaller and decreases as a function of stellar mass. For the highest stellar bin, this radius approaches close to the centre of the galaxy indicating that the outer accreted material is spread all over the galaxy.
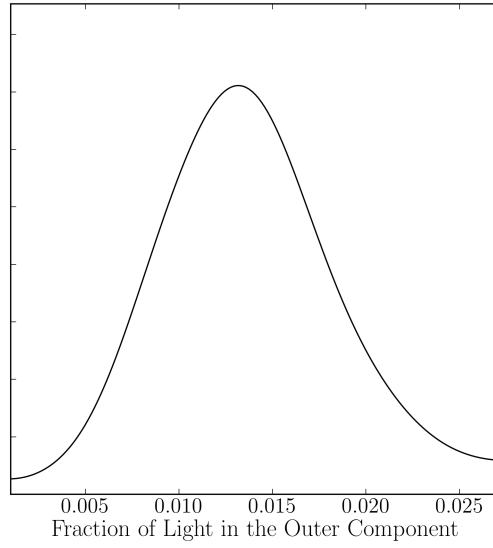
Figure 2.18: The probability distribution function (PDF) of f_{outer} for the stacked image of disk galaxies in the mass range $10^{10.0}M_{\odot} < M_* < 10^{10.8}M_{\odot}$ and with a concentration of $C < 2.6$.
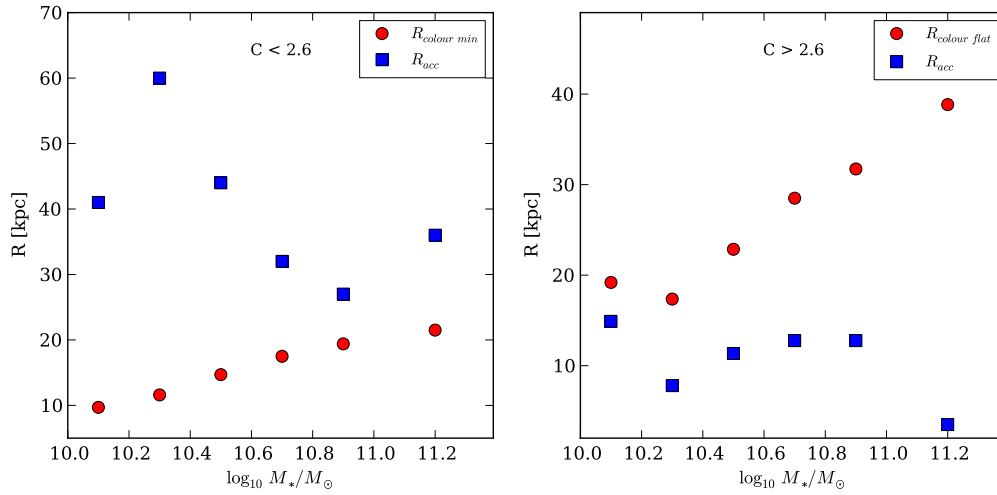
Figure 2.19: (a and b) The radius at which the accreted component begins to dominate over the in-situ component (R_{acc}) for low concentration and high concentration galaxies as a function of stellar mass (blue squares). Also shown is the radius at which there is a minimum in the g-r colour profiles ($R_{colour\,min}$) for low concentration galaxies and the radius at which the g-r colour profile ($R_{colour\,flat}$) flattens for high concentration as a function of stellar mass (red circles).

2.6 Summary

In this work, we have shown that stacking g and r band mosaics of similar galaxies allows us to derive reliable surface brightness profiles upto a depth of $\mu_r \sim 32\,\mathrm{mag\,arcsec^{-2}}$. We study surface brightness, ellipticity and g-r colour profiles as a function of stellar mass and galaxy type. We perform fits to the stacked images using multi-component Sérsic models. This enables us to estimate the fraction of the stellar light/mass in the outermost component, which we hypothesize to be built up from accreted stellar material, and to set constraints on theories for the formation of stellar haloes through hierarchical merging.

The main results of this paper can be summarized as follows.

1. The fraction of accreted stellar material increases with stellar mass. At fixed mass, the fraction of accreted material is higher in early-type than in late-type galaxies.

2. The stellar haloes of high concentration galaxies ($C > 2.6$) tend to be more elliptical than those of low concentration galaxies ($C < 2.6$). The ellipticity of the outer stellar halo increases strongly with stellar mass for high concentration galaxies, and more weakly with stellar mass for low concentration galaxies.

3. Because we stack galaxies that are nearly face-on, we are only able to probe the colour of the outer accreted component in high concentration galaxies. In these systems, the g-r colour of the outer halo light is bluer than than the centre of the galaxy and is an increasing function of stellar mass.

4. We find that a single-Sérsic profile cannot fit the entire two-dimensional surface brightness distribution of any of our stacked images . Multi-component models are needed to model the excess light in the outer parts of the galaxy, especially between $\mu_r \sim 28 - 32\,\mathrm{mag\,arcsec^{-2}}$, and to account for the radial dependence of the ellipticity of the light distribution.

5. Double-Sérsic profiles adequately model the surface brightness distributions of high concentration galaxies ($C > 2.6$), while triple-Sérsic profiles are often needed to model the surface brightness profile of low concentration galaxies ($C < 2.6$).

6. Using the fraction of light in the outer component of our models as a measure of the fraction of the total stellar mass composed of accreted stellar material, we find that this fraction is an increasing function of stellar mass. At fixed stellar mass, it is also a function of concentration. For high concentration galaxies, the fraction of accreted stellar light rises from 30% to 70%, while for low concentration galaxies the fraction of stellar light rises from 2% to 25% for galaxies in the stellar mass range $10^{10.0} M_\odot$ to $10^{11.4} M_\odot$.

2.7 Discussion

We have attempted to characterise the stellar halo of galaxies through modelling their surface brightness. It is the depth, the large dynamic range and the two-dimensional shape information (ellipticity) of our surface brightness profiles which enables us to recognise deviations from a single component profile and to model successfully the stellar halo of our galaxy stacks out to 100 kpc with two or three components.

An important outcome is that a single Sérsic component cannot fit the surface brightness profiles of high concentration galaxies over a large dynamic range in radius and surface brightness, but can only fit the inner parts of galaxies. The inability of a single Sérsic to fit the two-dimensional surface brightness profile of galaxies has also been confirmed by the studies of Bernardi et al. (2013), Simard et al. (2011) and Lackner & Gunn (2012). Multi-component models are needed to model the full two-dimensional surface brightness profiles of galaxies. We have demonstrated that it is both the average shape of the surface brightness profile and the radial variation in ellipticity of the light in a galaxy stacks that constrain such models.

For high concentration galaxies, the effective radius of the outer component is twice as large as the effective radius of the inner component. For low concentration galaxies, the effective radius of the outer component is much larger than the inner components. For high concentration galaxies, the luminosity of the outer component is a significant fraction of the total luminosity of the galaxy and ranges from 30% to 70%. It also dominates over a large radial range of the galaxy. On the other hand, in low concentration galaxies, the outer component occupies a smaller fraction (from 2% to 25%) and is only dominant at radii larger than $20 - 30$ kpc. In both cases, the fraction of light in the outer component increases with stellar mass (see the red line in the top plots of Figure 2.17 and Figure 2.14).

We propose that the fraction of light in the outer component provides a measure of the amount of accreted stellar light in the galaxy. While a direct one-to-one correspondence between the fraction of light in the outer component and the fraction of accreted stellar light cannot be directly proven, the trends in the fraction of light in the outer component agree qualitatively with the trends of the accreted light fraction as a function of mass and galaxy-type in the particle-tagging models of (Cooper et al., 2013). Interestingly, the rate of increase of accreted stellar mass increases dramatically above $M_* \sim 10^{10.6} M_\odot$. This corresponds to the stellar mass where galaxies transition from blue/star-forming to red/passive systems (Kauffmann et al., 2003). A significant jump in the accreted mass fraction may be most simply explained by *in-situ* growth of the galaxy being terminated by feedback processes, such as energy injection from relativistic jets produced by black holes in massive galaxies (Croton et al., 2006). In the two stage model of massive galaxy formation proposed by Oser et al. (2010), an early, rapid *in-situ* star formation period is followed by a late merger-dominated period. In the later phase, galaxies tend to grow predominately through minor mergers. We note that the particle tagging models of Cooper et al. (2013) are directly tied to semi-analytic models that include AGN feedback prescription, and thus also include quenching of *in-situ* growth of galaxies through cooling and star formation.

Measuring the ellipticity of the outer stellar halo of galaxy also provides us with hints

about the formation processes for the stellar halo. A high ellipticity is likely to imply that satellite systems are preferentially accreted along the major axis of the main galaxy (Tal & van Dokkum, 2011). The variance in the outer stellar halo profile between different galaxies can be predicted from our surface brightness profiles. This variance results from the fact that similar galaxies can have stellar haloes with very different masses, sizes and shapes. The physical origin of this variance as predicted by the ΛCDM models, is that galaxies of the same mass have had a range of merger histories, resulting in different accreted stellar mass fractions. This has also been clearly demonstrated using particle-tagging techniques on the Aquarius haloes (Cooper et al., 2010), which show very large halo-to-halo differences.

We also note that the integrated surface brightness of the galaxy, including the stellar halo, includes considerably more light that measured by the SDSS `model` and `cModel` magnitudes. For example, for high concentration galaxies in the stellar mass range $10^{11.0} M_\odot < M_* < 10^{11.4} M_\odot$, there is about 50% more light contained in the stellar halo at surface brightnesses greater than $\mu_r \sim 24.5 \, \mathrm{mag \, arcsec^{-2}}$. This implies that there is considerably more stellar material in the galaxy that one might infer from the SDSS photometry. The stellar masses defined by the MPA-JHU catalogue and used in this work are only used to define the stellar mass bins, and are systematically less than the true stellar mass of the galaxy. We quantify this in Chapter 4.

Chapter 3

Parametrizing the Stellar Haloes of Galaxies

3.1   Introduction

Much progress has been made in recent years in theoretically understanding the build up of stellar haloes of galaxies from the debris of smaller accreted satellites that are tidally disrupted. However, progress in this field has been hampered by a lack of good observed statistical constraints from a large number of galaxies.

In Chapter 2, we demonstrated that by stacking thousands of images of similar isolated galaxies together from the photometric SDSS survey we were able to detect the average stellar halo of galaxies out to 100 kpc from the galaxy centre and study the average properties of the stellar halo as a function of stellar mass and galaxy type. In this Chapter, we seek to study the average properties of the stellar halo of a large complete volume limited sample of central galaxies as a function of halo mass estimated from the Yang et al. (2007) galaxy group catalogue. For this purpose, we optimise our masking algorithm to deal with group and cluster environments.

In Chapter 2, we parametrized the stellar halo by fitting double Sérsic models to 2D surface brightness distribution of the galaxy stack. We found that the inner and the outer components have different radial and ellipticity profiles. Moreover, we found that the average fraction of stellar light in the outer component increases from 30% to 70% and from 2% to 25% for early and late-type galaxies respectively over the mass range $10^{10.0} M_\odot$ to $10^{11.4} M_\odot$. In this Chapter, we test whether the outer light fraction can be used as a measure of the accreted mass fraction using mock images from the Illustris set of simulations.

Moreover, taking advantage of the large sample size used in this work, we explore whether the outer light fraction correlates with the internal structural properties of the galaxy, or whether they are independent. Further, we compare these observational constraints with those expected from theoretical models, namely the Illustris suite of simulations (Vogelsberger et al., 2014).

This chapter is organised as follows: in Section 3.2, we select our sample of galaxies and outline our methodology as to how we process the images of the galaxies, the binning schemes we use for stacking and the methods we use to analyse the stacked images.[1] In Section 3.3, we introduce the `Illustris` cosmological hydrodynamical simulations and test our method to recover the average accreted light fractions from the galaxy stacks. In Section 3.4, we present the results from our analysis of the stacked images. In Section 3.5, we compare our results with predictions from simulations. We discuss our results in Section 3.6. Throughout this chapter, we assume a flat ΛCDM cosmology, $\Omega_{\mathrm{m}} = 0.25$, $\Omega_{\Lambda} = 0.75$ and Hubble parameter $h = 0.72$.

3.2 Observations and Methodology

3.2.1 Sample Selection

We select central galaxies from the Yang et al. (2007) galaxy group catalogue constructed from the NYU-VAGC (New York University - Value Added Catalogue) catalogue updated to DR7. This group catalogue was constructed using a halo group finder which is designed and optimized using numerical simulations to iteratively select galaxies that reside in the same dark matter halo. In particular, we use the `Sample II` catalogue which was built using the `Model` Magnitudes and which utilised additional redshift information available from alternative sources (mainly from 2dFGRS). We select the galaxy which is the most massive in the group as the central galaxy. For each central galaxy, we use the halo mass estimated from the characteristic stellar mass of the group. The characteristic stellar mass of a group is defined as the combined stellar mass of all galaxies in a group whose luminosities are $M_r^{0.1} - 5 \log \leq -19.5$, taking into account completion and edge effects of the survey (Eq. 13 of Yang et al.). They demonstrate that there is a good correlation between the line-of-sight velocity dispersion and the estimated halo mass from the characteristic stellar mass of the group for the more massive groups.

We consider several samples in halo mass and redshift bins as listed in Table 3.1. The higher halo mass sub-samples extend to a higher redshift range ($0.05 < z < 0.2$) to ensure completeness and a sufficient sample for stacking. To avoid the adverse effects of the PSF on edge-on disk galaxies, we removed all galaxies with axial ratio ≤ 0.6. The majority of the galaxies in these samples have at the most one or two spectroscopic members in the group. This implies that the halo masses derived from the characterstic stellar mass will not be very accurate. The estimated uncertainty in the halo mass is aroung 0.2 dex. Limiting the sample to groups with a minimum of 3 spectroscopic members reduces the total sample to ~ 8500 galaxies.

We use the stellar masses as defined in the MPA-JHU catalogue. For the galaxies in our sample, we show the relationship between their MPA-JHU stellar masses and the halo masses from the Yang et al. (2007) catalogue in Figure 3.1. We also overplot the

---

[1]In the Appendix, we detail the masking procedure used in this work which is optimised for group environments.

Table 3.1: Sample of galaxies selected by halo mass and redshift from the Yang et al (2007) group catalogue.

Sample	Halo mass	Redshift	N_{gal}	$N_{gal\,3}$
H1	$11.785 \leq \log(M_{halo}/M_\odot) \leq 12.285$	$0.05 \leq z \leq 0.2$	53992	101
H2	$12.285 \leq \log(M_{halo}/M_\odot) \leq 12.5$	$0.05 \leq z \leq 0.2$	59553	455
H3	$12.5 \leq \log(M_{halo}/M_\odot) \leq 13.285$	$0.05 \leq z \leq 0.2$	48483	1772
H4	$13.285 \leq \log(M_{halo}/M_\odot) \leq 13.785$	$0.05 \leq z \leq 0.2$	25269	3301
H5	$13.785 \leq \log(M_{halo}/M_\odot) \leq 14.285$	$0.05 \leq z \leq 0.2$	6196	2173
H6	$14.285 \leq \log(M_{halo}/M_\odot) \leq 15.785$	$0.05 \leq z \leq 0.2$	1303	981

stellar-halo mass relationship from Moster et al. (2010). For each galaxy, we calculate its concentration ($R90/R50$) and its surface mass density ($\mu_* \sim M_*/[2\pi R50^2(r)]$), where $R50$ and $R90$ are the Petrosian radii containing 50% and 90% of the total light of the galaxy.

3.2.2 Image Processing and Stacking

We construct large mosaics in the g, r and i bands centred on each galaxy from the sky-subtracted SDSS Data Release 9 images using `SWarp` (Bertin et al., 2002). The size of the mosaics were 1 x 1 Mpc for galaxies above halo mass $\log(M_{halo}/M_\odot) > 13.5$ and 500 x 500 kpc for the rest of the galaxies.

We optimise the masking algorithm by D'Souza et al. (2014) to deal with crowded fields and the scattering of light from multiple sources. Using `SExtractor` (Bertin & Arnouts, 1996), we conservatively masked out other sources in the image, by employing the use of segmentation maps. To achieve this, we first stacked the mosaics in all three bands to create a 'master image'. The master image was convolved with a large 12 pixel top hat kernel. Using `SExtractor`, a segmentation map was created from the convolved 'master image', using a minimum detection area of 5 pixels, a Gaussian filter of 7×7 pixels (FWHM=4.0 pixels) for detection, a detection threshold of $1.5\,\sigma$, 32 deblending sub-thresholds, a deblending minimum contrast parameter of 0.001 and a global background detection. The use of a smoothening filter and a minimum detection area in combination with a low detection threshold allows one to reveal low surface brightness objects at the limits of detectability (Dalcanton et al., 1997). The masks were successively applied to individual g and r-band mosaics. The i-band mosaics were only used for creating the master images for the masking procedure. In Appendix A.4, we demonstrate that our masking algorithm is robust against undetected sources and scattered light. The over-subtraction of real stellar structures due to the masking process is minimised through the stacking procedure outlined later.

The masked mosaics were corrected for Galactic extinction following Schlegel et al. (1998) and then transformed to the highest redshift range of the sub-sample with the flux-conserving IRAF task `GEOTRAN`. This involves both a cosmological surface brightness
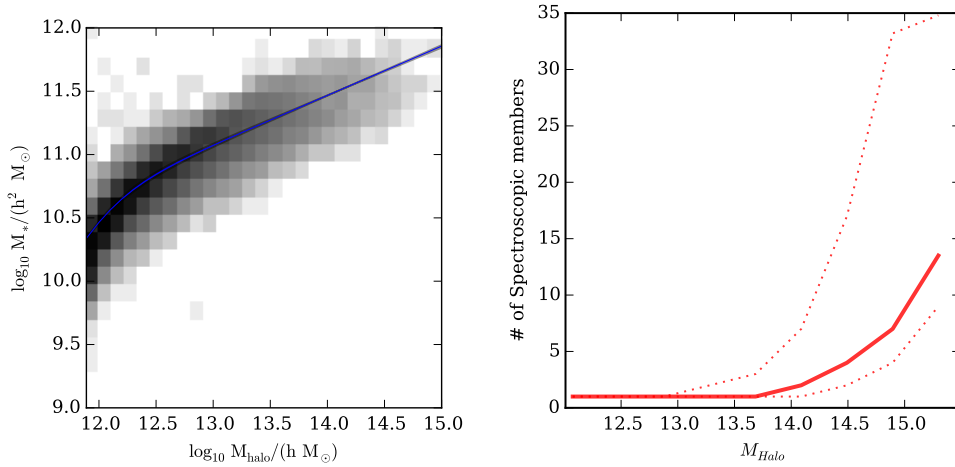
Figure 3.1: Top: The MPA-JHU stellar mass as a function of its estimated halo mass. Over-plotted is also the stellar-halo mass relationship from Moster et al. (2010). Bottom: Median number of spectroscopic confirmed galaxies in the group as a function of halo mass. Dotted lines represent 16% and 84% of the distribution.

dimming of $(1 + z)^4$ and an image re-scaling. A final run of `SExtractor` was used to determine the position angle of the galaxy in the r-band mosaic. This position angle is measured by calculating the second-order moments of the intensity distribution and corresponds to a surface brightness threshold of $\sim 24\,\text{mag arcsec}^{-2}$, or a radius of ~ 10 kpc. Each mosaic was then rotated using `GEOTRAN` such that the major axis of each galaxy was aligned. The final transformed mosaics were cropped to a uniform size. We did not apply any K-corrections because of the additional uncertainty they introduce. At $z = 0.1$, $1\,\text{pixel} = 0.71\,\text{kpc}$: the smaller 500 x 500 kpc mosaics were cropped to a uniform size of 1000×1000 pixels. At $z = 0.2$, $1\,\text{pixel} = 1.27\,\text{kpc}$: the mosaics are cropped to a uniform size of 1600×1600 pixels.

Individual transformed mosaics were discarded if found unsuitable for stacking. First, mosaics with bright sources ($m_{r\,Petrosian} < 12.0$ and within a distance of 1 Mpc from the centre of the galaxy) were removed. Secondly, if the masking algorithm failed, the mosaic was discarded. Finally, we calculated histograms of the average intensity and the cumulative intensity of all the unmasked pixels in each mosaic. Mosaics which deviated more than $3\,\sigma$ from the median values were discarded. Closer examination reveals that often the masking algorithm failed in such cases, due to extremely crowded fields or neighbouring bright stars.

The mosaics were stacked using either a clipped-mean or a median stacking taking into consideration the masked regions. For the clipped-mean stack, we removed 5% of the extreme minimum and maximum values. While stacking, we weighted each galaxy images by $1/V_{max}$ (where, V_{max} is the total comoving volume out to the redshift of the galaxy). Errors on the stacks were calculated using bootstrapping.

3.2.3 Binning Procedure

We stack galaxies in bins of halo mass, stellar mass, concentration and surface mass density. In the following sections, we bin in terms of :

1. halo mass.

2. stellar mass.

3. halo mass and galaxy type.

4. halo mass and concentration.

5. halo mass and central dispersion, $(u - r)^{0.1}$, central D4000 and surface mass density.

We separate late-type from early types based on the morphological concentration parameter (Strateva et al., 2001). $C < 2.6$ are considered late-type galaxies, while $C > 2.6$ are considered early-type galaxies. We ensure that each of the stacks contain enough number of galaxies such that we can reach a limiting depth of $31 \, \mathrm{mag \, arcsec^{-2}}$ (See Figure 2.2).

3.2.4 Analysis of the stacked images

We follow the methodology of D'Souza et al. (2014) in calculating the average ellipticity, surface brightness and g-r colour profiles of the galaxy stacks. In addition, we also calculate the outer slope of the surface brightness profile as well as the accreted light fraction. We summarise the main elements of the procedure outlined in D'Souza et al. (2014) and highlight the relevant changes.

1. *Individual PSF.* In this work, we explicitly calculate a PSF for each stack in the g and r band in the following way. We first stack bright stars together following the methodology of D'Souza et al. (2014) to create a general average PSF reaching out to a radius of 100 pixels. Beyond this, we extend the PSF out to a radius of 500 pixels by assuming a conservative powerlaw slope of -2 (Sandin, 2014). This allows us to create a general "conservative PSF" of size 1000×1000 pixels. For each galaxy in the stack, we rescale this "conservative" PSF to account for the transformation of the galaxy image to redshifts $z = 0.1$ or $z = 0.2$ depending on the stacks. The final average PSF of the stack is obtained by a clipped-mean stacking of the individual rescaled PSFs. Due to the rescaling involved, the FWHM of the average PSF of the stack is smaller than used in D'Souza et al. (2014).

2. *g-r colour profiles and image deconvolution.* g-r colour profiles were constructed from surface brightness profiles in the r and g band. The error on the g-r is the quadratic sum of the errors in each band. The PSF can affect the g-r colour profiles of galaxies, especially of late-type galaxies. Hence, we deconvolve the stacked images using the methodology outlined by Tal & van Dokkum (2011). In short, we fit a double Sérsic

model convolved with the PSF to the 2D surface brightness distribution. We find the residuals by subtracting the PSF convolved model from the image. The deconvolved image is the double Sérsic model to which we add the residuals. Such a procedure is sufficient to reduce the effect of the PSF on the radial g-r colour profile of the galaxy stack. By generating mock images, we have demonstrated that this procedure is robust. In general, we find that effect of the above rescaled PSFs have a negligible influence on the g-r colour profiles.

3. *Ellipticity profiles.* We derive ellipticity profiles by fitting concentric ellipses to contours of the surface brightness distribution of the stacked images after convolving it with a Gaussian smoothing kernel. The standard deviation of the smoothing kernel ranged from 1 pixel at the center of the image to 5 pixels at around 80 kpc. The size of the kernel image is 8 times the standard deviation.

4. *Residual background subtraction.* A small amount of residual sky background remains after stacking the sky subtracted SDSS DR9 images (Blanton et al., 2011). We estimate this residual background in a circular annulus of 100 pixels width at the outskirts of the mosaic, and subtract it from the stacked image.

5. *Surface brightness profiles.* Surface brightness profile down to $\mu_r \sim 26\,\mathrm{mag\,arcsec^{-2}}$ along the major axis were derived in elliptical annuli on the sky-subtracted stacks. Errors in the surface brightness profiles were estimated from the error image derived through bootstrapping the stacking process.

6. *Outer slope.* We calculate the outer slope $\Gamma = d(\log_{10} I)/d(\log_{10} R)$ of the surface brightness profiles for the r-band stacks using measurements from R_{90} (the radius containing 90% of the light of the galaxy) to the radius where the surface brightness profile reaches $31.5\,\mathrm{mag\,arcsec^{-2}}$ according to the methodology outlined in the Appendix of D'Souza et al. (2014). Our calculation of the outer slope takes into consideration the errors in the surface brightness profile. Hence, the inner data points are weighted much more than the outer data points. Our choice of calculating the slope beyond R_{90} is motivated by the fact that at this radius we are uniformly probing the outer stellar halo across all galaxy types.

7. *Outer light fraction.* We calculate the outer light fraction using the methodology of D'Souza et al. (2014). We fit double Sérsic models convolved with the stacked PSF to the 2D surface brightness distribution of the stacks. The fraction of light contributed by the outer Sérsic component is the outer light fraction. In Appendix A.5, we outline how we estimated the outer light fraction from the SDSS stacks consistently across the final transformed redshift. In Section 3.3, we test if the outer light fraction corresponds to the accreted mass fraction using mock images from simulations.

3.3 Accreted mass fractions from stacked mock images

In D'Souza et al. (2014), we measured the outer light fraction of the galaxy stack by taking advantage of the fact that the full 2D surface brightness distribution of the stack could be approximated by an inner and outer Sérsic models with fixed ellipticity. Using mock images from the `Illustris` suite of simulations (Vogelsberger et al., 2014), we now test whether the outer light fraction is equal to the accreted mass divided by the M/L ratio.

3.3.1 Comparison with the `Illustris` Simulations

The Illustris simulations are large hydrodynamical simulations run with the `AREPO` code (Springel, 2010) and include key physical processes that are believed to be relevant for galaxy formation [2]. We use Illustris-1, the highest resolution run, which handles the DM component with a mass resolution of $m_{DM} = 6.26 \times 10^6 M_\odot$ and the baryonic component with $m_{baryon} = 1.26 \times 10^6 M_\odot$. The gravitational softening lengths are 1.4 and 0.7 kpc for the DM and baryonic particles respectively. From these simulations, we select 4644 central galaxies at $z = 0$, whose mass of the DM subhalo is $\log_{10} M_{halo}/h \geq 11.5$. Each of these galaxies are resolved by much more than 3500 stellar particles per halo. For each galaxy, we separate stars into "insitu" and "accreted" components. Insitu stars are those stars, that at the time of formation lie on the main progenitor branch of a given halo at $z = 0$. For each galaxy, we can thus define an accreted mass fraction.

We first compare the radial stellar mass surface density profiles of Illustris galaxies with observational constraints from SDSS. In the top panel of Figure 3.2, we plot the median radial stellar mass surface density profiles of the Illustris galaxies along with their scatter in bins of halo mass. To compare with observational data, we overplot the median and the scatter in the stellar mass surface brightness profiles of the SDSS galaxies out to 4 kpc for each halo mass bin. These profiles were obtained by multiplying a radially constant MPA-JHU M/L ratio with the SDSS r-band `profMean` surface brightness profiles of galaxies. We find a remarkable agreement between the median surface mass density profiles of the Illustris galaxies and the SDSS data. Deviations are found in the lowest halo mass bin. The scatter in the surface mass density profiles in the SDSS galaxies is larger than the scatter found in the Illustris simulations. The low scatter in the Illustris simulations is

---

[2] The Illustris simulations include a number of physical processes. The relevant references are: (a) **Star formation**: Springel et al. (2005a); Springel and Hernquist (2003); Yepes et al. (1997); Chabrier (2003); Bruzual and Charlot (2003). (b) **Stellar evolution and enrichment**: Wiersma et al. (2009b); Matteucci et al. (2006); Greggio (2005); Karakas (2010); Travaglio et al. (2004); Thielemann et al. (2003); Maoz et al. (2012); Dahlen et al. (2004); Portinari et al. (1998). (c) **ISM and cooling**: Katz et al. (1992, 1996); Wiersma et al. (2009a); Smith et al. (2008); Rahmati et al. (2013); Faucher-Giguere et al. (2009); Ferland et al. (1998); Katz et al. (1996); Cen (1992). (d) **Galactic-scale stellar feedback**: Puchwein and Springel (2013); Oppenheimer and Davè (2008, 2006); Okamoto et al. (2010); Springel and Hernquist (2003). (e) **BH and AGN feedback**: Di Matteo et al. (2008); Springel et al. (2005a); Di Matteo et al. (2005); Sijacki et al. (2007, 2009); Vogelsberger et al. (2013); Ciotti and Ostriker (2007); Sazonov et al. (2005); Yu and Tremaine (2002).
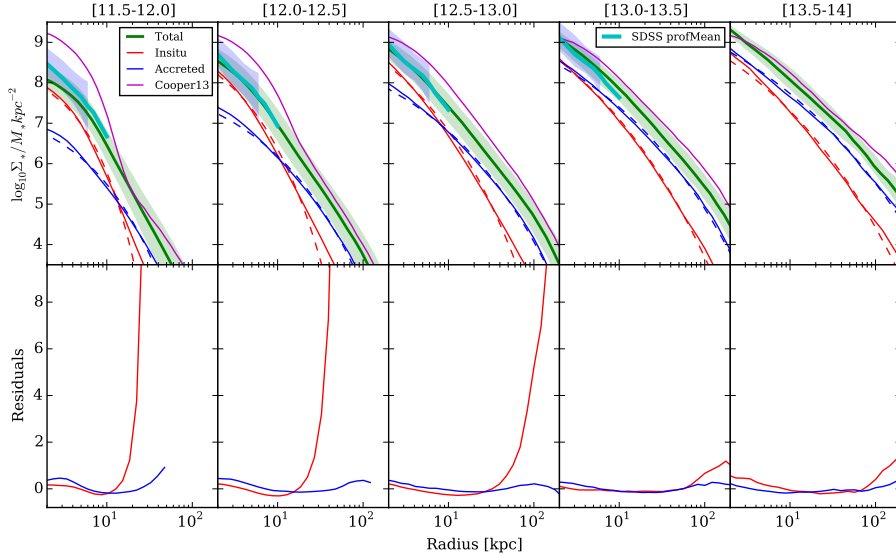
Figure 3.2: The top panel shows the median of the total (green), insitu (red) and accreted (blue) stellar mass surface density profiles in various halo mass bins from the Illustris simulations. The purple line indicates the stellar mass surface density profiles (1% tagging) from Cooper et al. (2013). The light green region indicates the 10-90 per cent scatter of the median profile of the Illustris galaxies. The thick cyan line indicates the median of the stellar mass surface density profiles obtained from SDSS `profMean` radial observations multiplied by a radially constant MPA-JHU M/L ratios. The scatter in the SDSS profiles is indicated in light shaded blue. Dashed red and blue lines indicate Sérsic fits to the insitu and accreted median profiles. The bottom panel indicates the residuals of the fit to the insitu (red) and accreted profiles (blue).

partly due to the AGN feedback prescriptions and the way the ISM is approximated in the simulations (Kauffmann, 2015).

In Figure 3.2, we also plot the stellar surface mass density profiles of the insitu and accreted components of the galaxies in each halo mass bin. The overall shape of the surface mass density profiles is determined by the relative contributions of the insitu and the accreted components. For the lower halo mass galaxies, the inner part of the surface mass density profile is dominated by the insitu component, while the accreted component dominates the surface mass density profile at radii larger than 15 kpc. For the largest halo mass galaxies, the accreted component dominates the overall stellar mass surface density profile at all radii.

We also compare the median Illustris profiles with the 1% tagged stellar mass surface density profiles from Cooper et al. (2013). As seen in Figure 3.2, the profiles differ in both normalisation and shape from those of the Illustris galaxies, especially for the lower halo mass galaxies. In particular, the pronounced bump or the inflexure in the Cooper et al.
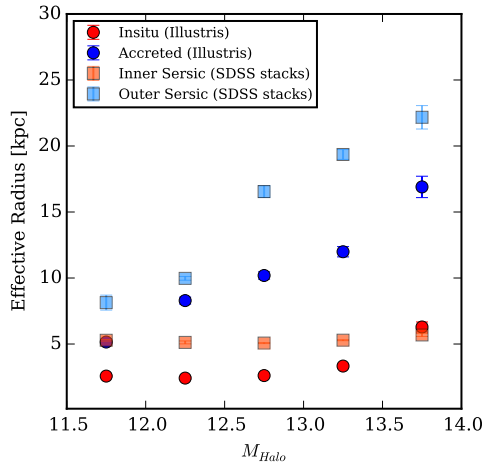
Figure 3.3: The effective radius of the Sérsic components fit to the insitu and the accreted components respectively (round symbols). Also shown is the effective radius of inner and outer components of the double Sérsic model fit to the 2D surface brightness distribution of the SDSS stacks (square symbols).

surface mass density profile (arising at the point where the accreted component dominates over the insitu component) is not so prominent in the surface mass density profiles from the Illustris galaxies.

We fit Sérsic functions separately to the median radial insitu and the accreted components in each halo mass bin. The residuals of the fits are shown in the lower panels of Figure 3.2. Overall, we find that the insitu and accreted components can be well described by Sérsic functions. Deviations of the insitu component from the Sérsic model are seen at large radii. These deviations decrease with halo mass and are probably due to an excess of young stars formed at the outskirts of galaxies. This has been previously identified as one of the limitations of the Illustris galaxy formation model, where lower mass disk galaxies at $z = 0$ exhibit strong stellar and gaseous ring-like features Snyder et al. (2015).

The effective radius of the Sérsic models fit to the insitu and the accreted components are shown in Figure 3.3. The effective radius of the insitu component is around ~ 2.5 kpc, while the effective radius of the accreted component is larger than 5 kpc and increases with halo mass. The effective radius of the insitu component is larger than the width of PSF used to create the mock images. We also overplot the effective radius of the inner and outer components of the double Sérsic model fit to the 2D surface brightness distribution of the observational SDSS stacks. We find that the effective radius of the outer Sérsic component is much larger than found in the simulations.
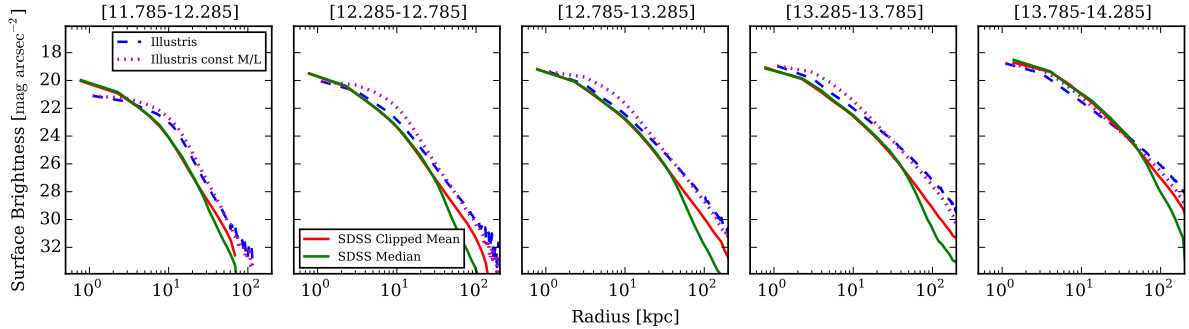
Figure 3.4: We compare the surface brightness profiles in elliptical annuli between the mock stacks from the Illustris simulations (blue dashed lines) and the stacked SDSS data (solid lines). The red solid lines show the clipped-mean stacks, while green solid lines show the results from median stacking. We also indicate the surface brightness profiles from the mock Illustris stacks assuming a constant M/L ratio (maroon dashed lines).

3.3.2 Mock Images from the `Illustris` Simulations

We construct mock r-band SDSS-like images of the Illustris galaxies in three projections with realistic levels of sky, Poisson noise, scattering due to the average SDSS PSF and with the scale $1\,\mathrm{pix} = 1\,\mathrm{kpc}$. We use the stellar magnitudes in the r-band provided by the public release of the Illustris simulations. These were calculated using Bruzual & Charlot (2003) models and a Chabrier (2003) IMF. For each galaxy image, we calculate its Petrosian radius R_p as well as its R_{50} and R_{90} defined similarly as in observations. We also calculate for each galaxy image its concentration and its surface mass density. We stack the mock images of galaxies in bins of halo mass. Each mock image was rotated such that the total distribution of flux in the inner part of the galaxy are aligned, before stacking. This was done in order to mimic the observational analysis and allow for a direct comparison with the SDSS stacks.

We measure the surface brightness in the r-band stacks of the mock galaxies from the Illustris simulations in elliptical annuli. In Figure 3.4, we compare the surface brightness profiles between the stacks of mock galaxies and those from the SDSS data. The latter is shown for the clipped-mean and median stacking. We find that the surface brightness profiles are a strong function of halo mass for both the Illustris and the SDSS galaxies. There are noticable differences in the profiles of the mock galaxies from Illustris and those derived from SDSS data. In the lower halo mass bins, the effective radius of the Illustris galaxies are larger than found in the data (Snyder et al., 2015). For larger halo masses, small differences are also seen in the surface brightness profile at large radii: the surface brightness of SDSS galaxies is slightly lower than found in the Illustris simulations.

We also note that the surface brightness profiles of mock galaxies assuming a constant radial M/L ratio show considerable differences with the profiles derived using the Illustris
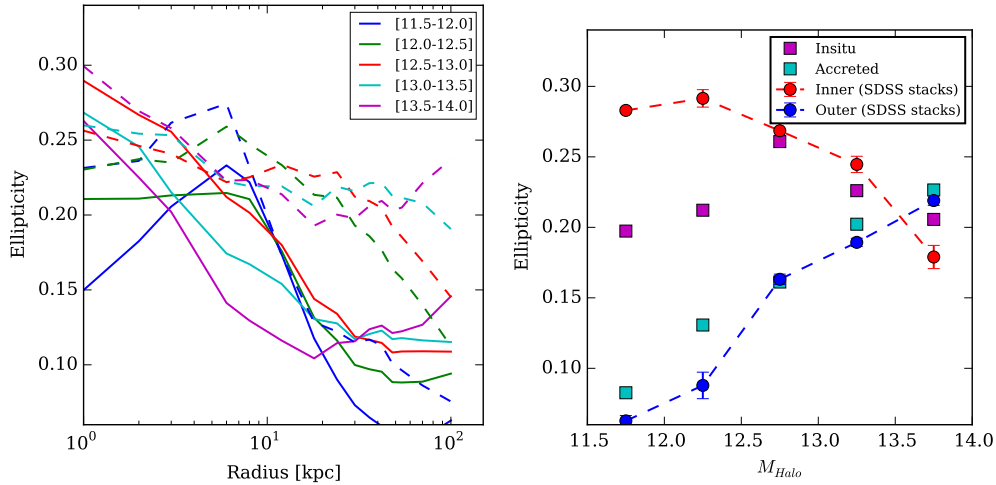
Figure 3.5: Left: Difference in ellipticity profiles between the insitu (solid line) and accreted (dashed lines) components from mock galaxy observations of the Illustris simulations. Right: Ellipticity of insitu and accreted components versus ellipticity of inner and outer Sérsic components.

M/L ratio. The profiles with constant radial M/L ratio were constructed such that the M/L ratio of the central part of the galaxy was assumed to be constant throughtout the galaxy. This difference in the shape of the profile decreases with halo mass. We will come back to this in Section 3.5.3 when we discuss the stellar age and metallicity profiles of the Illustris halos in detail.

Profiles derived from the SDSS median stacks show significant differences with the clipped-mean stacks below $\mu_r \sim 27\,\mathrm{mag\,arcsec^{-2}}$. In particular, the surface brightness profiles of the SDSS median stacks begin to get steeper beyond a certain radius than the profiles from the clipped-mean stacks. This difference in the surface brightness profiles hints to a possible skewed distribution of the outer stellar haloes for a given halo mass. No such difference in surface brightness profiles is found in the mock Illustris stacks. For the lowest halo mass bins, the two profiles (clipped-mean and median) differentiate at a radius which contains 98% of the total light of the galaxy. For the highest halo mass bins, the profiles differentiate at a radius which contains 87% of the total light of the galaxy. The difference in total light between the median and the clipped-mean stacks is at the most 2-3%. This implies that the smaller scatter in stellar surface mass densities in the Illustris galaxies compared to the SDSS galaxies, persists out to large radii.

We measured the ellipticity profiles of the final stacks by fitting contours to the 2D surface brightness distribution. We also measure the ellipticity of the insitu and accreted stellar components in the final galaxy stacks by creating mock images of the separate components (see Figure 3.5). We find that the insitu and the accreted components have distinct ellipticity profiles in the final stacks. The insitu component is extremely elliptical at the center of the galaxy and becomes more circular towards the outskirts. On the
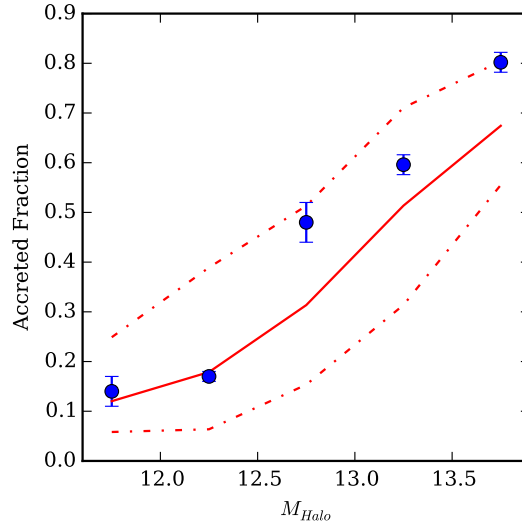
Figure 3.6: Test of whether we can recover the true accreted mass fraction of stars using the fraction of the integrated stellar mass in the outer Sérsic component. The red solid line represents the median accreted mass fractions as a function of halo mass in the Illustris simulations. The dashed red lines represent the 16th and 84th percentile distribution in the accreted mass fractions from the simulations. Blue squares represent the Illustris mock images with the M/L ratio derived using BC03.

other hand, the accreted component has a near constant ellipticity. Towards the outer regions, the accreted component is more elliptical than the insitu component. We note that each component of our double Sérsic model fit to the 2D surface brightness distribution has a fixed ellipticity. We also indicate the constant ellipticity of the inner and outer Sérsic models obtained from fitting models to the SDSS stacks. While there is a good agreement between the ellipticity of the inner/outer Sérsic models and the insitu/accreted components, the decreasing ellipticity of the insitu component indicates that the fixed ellipiticity of the inner Sérsic component is a limited approximation.

3.3.3   Testing our ability to recover the accreted mass fractions

We now test if the amount of light contained in the outer component by fitting double Sérsic models to its 2D surface brightness distribution multiplied by the M/L ratio is equal to the accreted mass fraction of the galaxy stack. The error image for the fitting procedure was estimated through bootstrapping the mock images.

In the top panel of Figure 3.6, we show the median accreted mass fraction as a function of halo mass along with 16th and 84th percentile distribution in the simulations. We also show the estimated light fraction in the outer component from fitting double Sérsic models to the 2D surface brightness distribution, as well as the uncertainty in the estimates.
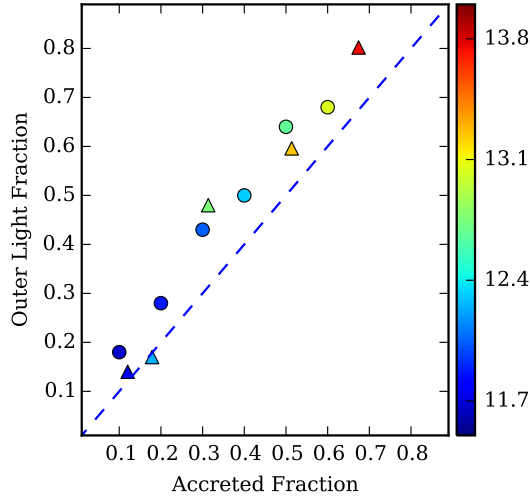
Figure 3.7: Accuracy of recovery of accreted mass fractions from the outer light fractions. The symbols are colour coded according to their median halo mass of galaxies in the stack. Round symbols indicate stacks with a limited spread in accreted mass fractions (explained in the text). Triangles are for stacks in bins of halo mass shown in Figure 3.6.

We find that the estimated outer light fraction is systematically higher that the median accreted mass fraction for each halo mass bin, especially for higher halo mass bins.

In order to check if we do not systematically over-estimate the outer stellar light fraction due to the way we bin our galaxies, we stack galaxies with a smaller spread in their accreted mass fractions. We do this by selecting galaxies with accreted stellar mass fractions in the ranges 0.15-0.25, 0.25-0.35, 0.35-45, 0.45-0.55 and 0.55-0.65 (with 2971,1371,700, 319 and 155 mock images in each bin respectively), while imposing that the scatter in halo mass in each bin was not more than 0.5 dex. We find that although we recover the general trend of an increase in the accreted light fraction, we overestimate the accreted light fractions not greater than 0.1 dex. For lower accreted fractions this accounts for a relative error of nearly 150%, while for higher accreted fractions we overestimate it by nearly 20%. This indicates that the overestimation in the mean accreted fractions is not due to the scatter in the true accreted fractions.

In Figure 3.7, we demonstrate how accurately we can recover the accreted mass fraction from the outer light fraction, for various halo mass ranges. We conclude that we can predict the accreted mass fractions to an accuracy of 0.1 dex.

In order to estimate how much our assumption of fixed ellipticity for the inner Sérsic component affects our estimation of the accreted light fraction, we fit a model with decreasing ellipticity for the inner S'ersic component. We fix the rate of decrease of ellipticity to match the data in Figure 3.5, namely 0.04 per kpc. We find that estimate of the outer stellar fraction is 13% larger than that derived with the assumption of fixed ellipticity.
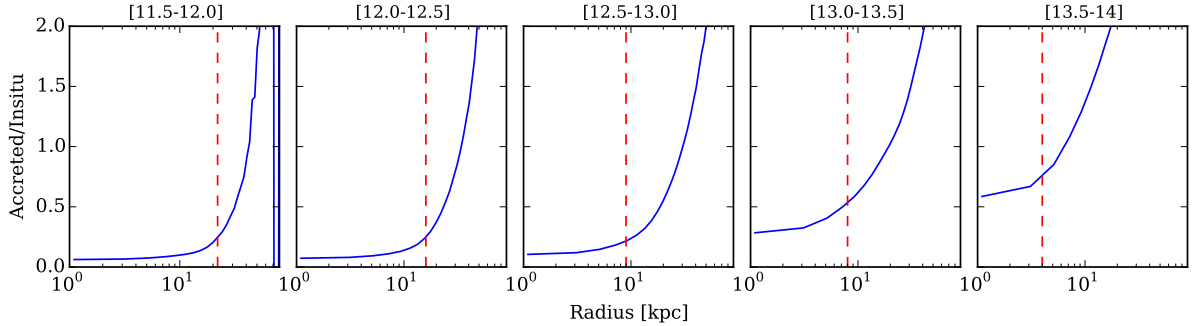
Figure 3.8: The radial profile of the accreted versus the insitu mass fraction for various halo mass bins derived the Illustris mock stacks. The dashed red line indicates the break in the surface brightness profile as mearured by fitting a double Sérsic model to the 2D surface brightness distribution.

Finally, we compare the break in the surface brightness profile as traced by the double Sérsic model with the fraction of accreted verses insitu material as a function of radius. We calculate the break in the surface brightness profile as the radius where the outer Sérsic component dominates over the inner Sérsic component. In Figure 3.8, we find that the break in the surface brightness profile occurs in the vicinity of the sharp increase in the fraction of accreted material over insitu material. For the lowest halo mass bin, we overestimate the break in the surface brightness profile. This indicates that the double Sérsic model indeed traces the insitu and accreted components of the galaxy stacks.

We conclude that the fitting of double Sérsic models to galaxy stacks traces well the insitu and accreted stellar components, and that the outer light fraction is a good measure of the accreted mass fractions of a galaxy.

3.4   Observational Results from Stacked Galaxies

3.4.1   Outer light fractions

Outer light fraction as a function of halo mass and stellar mass

We first study the outer light fraction as a function of halo mass and stellar mass in two regimes: above and below the characteristic mass ($\log M_{halo} \sim 12.5$ and $\log M_* \geq 11.0$) in the stellar-halo mass relationship. We first consider galaxies above the characteristic mass (~ 81000 galaxies). We stack galaxies as a function of increasing stellar mass. We also stack galaxies as function of increasing halo mass. Each stack contains 1000 galaxies. In Figure 3.9, we plot the outer light fraction as a function of stellar mass and halo mass. We find that the outer light fraction increases as a function of both stellar mass and halo mass. For a given halo mass and stellar mass, there is a considerable scatter in the outer

light fraction.

We quantify the correlation between the outer light fraction (f_{outer}) with stellar mass (M_*) and halo mass (M_{halo}). We fit a linear relation between f_{outer} and M_{halo} taking into consideration the statistical errors, and ask whether the residuals of f_{outer} from this relation are correlated with M_*. Similarly, we also fit a linear relation between f_{outer} and M_*, and examine if the residuals correlate with M_{halo}. In the lower panels of Figure 3.9, we find that the residuals from the M_*-f_{outer} fit correlate more strongly with M_{halo} than the residuals from the M_{halo}-f_{outer} fit with M_* (a Pearson coefficient of 0.245 vs 0.047).

We repeat the same exercise for galaxies above the characteristic mass which have 3 or more spectroscopic members ($\sim$ 8232 galaxies) (See Figure 3.10). We again stack in increasing stellar and halo mass (bins of 1050 galaxies). We find that the residuals from the M_*-f_{outer} fit correlate more strongly with M_{halo} than the residuals from the M_{halo}-f_{outer} fit with M_* (a Pearson coefficient of 0.469 vs -0.027). The increase in the significance of the result is likely due to the fact that halo mass is more accurately estimated if there are more group members. We conclude that above the characteristic mass, the primary relationship is between the outer light fraction (f_{outer}) and halo mass (M_{halo}).

Next, we consider galaxies below the characteristic mass. We similarly stack galaxies as a function of increasing stellar mass and halo mass. Most of the stacks contain 6000 galaxies. The lowest two stacks contain 9000 galaxies to ensure enough S/N to detect the outer light fraction. In Figure 3.9, we also plot the outer light fraction as a function of stellar mass and halo mass for galaxies below the characteristic mass. We find that the below the characteristic mass, there is a considerable decrease in the outer light fraction. We also find that the rate of change of the outer light fraction with halo mass below the characteristic mass is much steeper than the rate of change of the outer light fraction above the characteristic mass. By similarly examining the residuals between the relationships of $f_{outer} - \log(M_{Halo})$ and $f_{outer} - \log(M_*)$, we find that below the characteristic mass, the outer light fraction is a slightly stronger function of stellar mass than halo mass (a Pearson coefficient of -0.231 vs 0.353). However, the low significance of the correlation indicates that below the characteristic mass, the outer light fraction is dependent on a quantity other than the stellar mass or the halo mass. We explore this further in the following section.

Outer light fraction as a function of halo mass and concentration

In Figure 3.11, we estimate the outer light fraction as a function of halo mass and concentration of the galaxy. For a given halo mass, we find that the the outer light fraction is a strong function of concentration. For the lowest halo mass bin, there is an increase in the outer light fractions from nearly 15% (lowest concentration) to 60% (highest concentration). For the higher halo mass bins, there is a smaller increase in the outer light fraction with concentration. By comparing Figures 3.11 and 3.9, we find that for the lowest halo mass bin the change in outer light fraction with concentration is larger than the corresponding change with halo/stellar mass.

The outer light fraction also increases with halo mass for a given concentration. For the highest concentration bin, the outer light fraction increases from 60% to 90% with
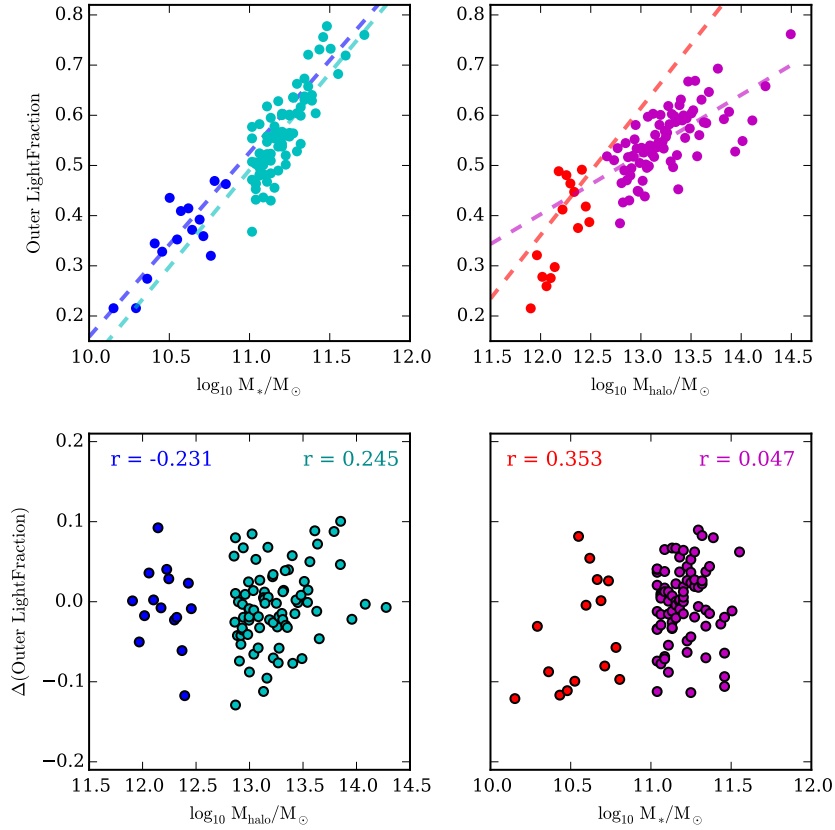
Figure 3.9: Top panels: The outer light fractions of SDSS stacks as a function of stellar mass (left) and halo mass (right) respectively in two regimes: galaxies above and below the characteristic mass ($\log M_{halo} \sim 12.5$) are shown on the right and left of each plot respectively in different colour schemes. The dashed lines indicates the best fit of the relationship between the outer light fraction and stellar mass/halo mass in the respective regime. Bottom left: The residuals from the best fitting $f_{outer} - \log(M_*)$ relation are plotted as a function of $\log(M_{Halo})$. Bottom right: The residual of the best fitting $f_{outer} - \log(M_{Halo})$ relation are plotted as a function of $\log(M_*)$. The Pearson coefficient of the residuals are also indicated in the lower panels for each of the mass ranges considered.
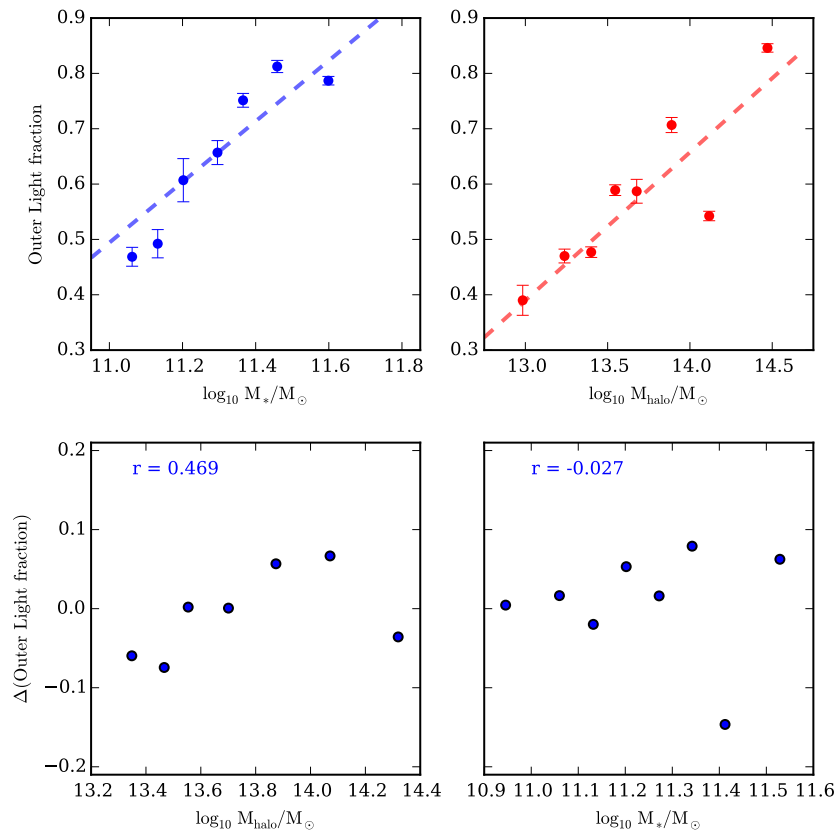
Figure 3.10: Same as Figure 3.9, but repeated for galaxy stacks with 3 or more confirmed spectroscopic members above the characteristic mass.
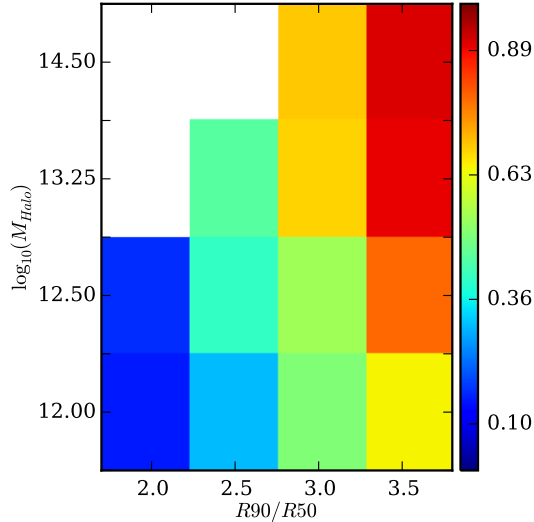
Figure 3.11: Outer light fractions of SDSS stacks in bins of halo mass and concentration.

increasing halo mass.

The large increase in outer light fraction with concentration implies that the morphological shape of the galaxy (probed by the concentration parameter) is strongly correlated with the accreted mass fraction. We note that in the lowest halo mass bin ($M_{Halo} \sim 12.0$), which corresponds roughly to the mass of the Milky Way's halo, the most bulge-dominated galaxies have accreted fractions as high as 60%.

For the lower halo mass bins, we find the outer light fraction is a stronger function of concentration than of other galaxy properties considered: central velocity dispersion, $(u - r)^{0.1}$ colour, central D4000 and surface mass density (See Figure 3.12).

For the lowest halo mass bin, we find that the outer light fraction is an increasing function of the central dispersion of the galaxy increasing from 30% (at 80 km/s) to nearly 52% (at 160 km/s). We are unable to probe galaxies with velocity dispersions lower than the instrumental resolution of the SDSS spectrograph (70 km/s). For the higher halo mass bin, the outer light fraction shows a weaker relation with the central velocity dispersion of the galaxy. We also find that the outer light fraction is an increasing function of the $(u - r)^{0.1}$ colour of the galaxy increasing from nearly 27% (bluer galaxies) to 52% (redder galaxies). These confirm the result that low halo mass bulge dominated galaxies with high central velocity dispersions and redder colours have higher outer light fractions, and hence higher accreted mass fractions.

We find that younger stellar populations probed by low central D4000 have a lower outer light fraction than older populations indicated by high central D4000 values. We find that low surface mass density galaxies have low outer light fractions ($\leq 10\%$), and that the outer light fraction increases with increasing surface mass density. The outer light
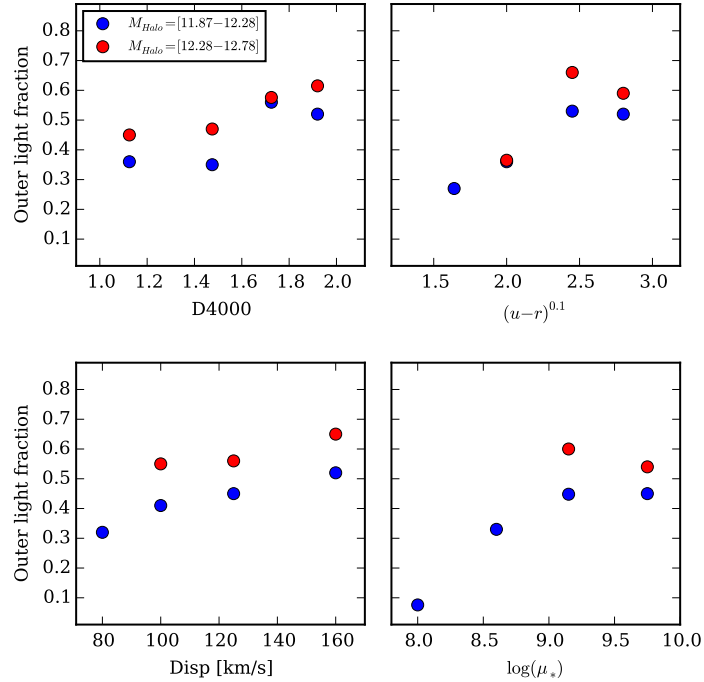
Figure 3.12: Outer light fractions of SDSS stacks as a function of central D4000, $(u-r)^{0.1}$, central dispersion and surface mass density for the two lowest halo mass bins.

fraction flattens for surface mass density greater than $\log(\mu_*) \sim 9$.

Finally, we test if the large variation in outer light fraction with concentration at low halo masses is sensitive to the sSFR. Fisher et al. (2009) showed that galaxies with a high central star formation (sSFR $> 10^{-11}\mathrm{yr}^{-1}$) have a high probability of being pseudo-bulge dominated. In Figure 3.13, we derive the outer light fraction for galaxy stacks in the lowest halo mass bin ($M_{Halo} = [11.87 - 12.28]$) as a function of concentration, but divided according to sSFR. In general, we find that the variation of the outer light fraction with concentration is quite robust to the central sSFR. Only at the high concentration end, we find that the outer light fraction is larger for galaxies with low sSFR than galaxies with high sSFR. This indicates that the outer light fraction is also less sensitive to the central sSFR than the concentration of the galaxy.

3.4.2 Outer Slope

Parametrising the outer slope of the surface brightness profile allows us an alternative way to characterise the stellar haloes of galaxies (Pillepich et al., 2014). In the work, we calculate the surface brightness profile in elliptical annuli and estimate the outer slope by fitting a straight line to the surface brightness profile from an outer radius to the radius
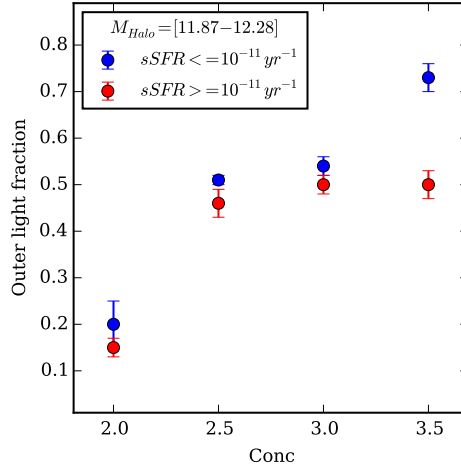
Figure 3.13: Outer light fractions of SDSS stacks as a function of concentration divided according to sSFR for the lowest halo mass bin $M_{Halo} = [11.87 - 12.28]$

which reaches the limiting magnitude of $31.5\,\mathrm{mag\,arcsec^{-2}}$ and taking into consideration the measurement errors. In Figure 3.14, we explore how our estimate of the outer slope of the surface brightness profile varies as a function of the inner and outer limiting radii. We first estimate the outer slope by varying the inner limiting radius from R_{50} to R_{90}. We find that the outer slope becomes steeper when we increase the inner limiting radius. For an inner limiting radius of R_{50}, there is hardly any relation of the outer slope with halo mass. The relationship of the outer slope with halo mass becomes more pronounced when increasing the inner limiting radius. The outer slope estimated from the surface brightness profiles calculated in circular annuli is slightly steeper for lower halo mass and slightly shallower for high halo mass as compared to that calculated in elliptical annuli. In estimating the outer slope, varying the outer limiting radius has a smaller effect that varying the inner limiting radius, since the inner high S/N measurements are weighted more over the outer low S/N measurements. We find that the measurement of the outer slope is strongly dependent on the way it is estimated.

In Figure 3.14, we also overplot the 2D projection of the predictions of the outer slope of the galaxies from the Illustris simulations and their intrinsic scatter (Pillepich et al., 2014). These were estimated by fitting a straight line from $R_{half\,mass}$ to R_{vir} in circular annuli without taking into consideration measurement errors. We find that there is a reasonable agreement in the overall trends of the prediction with our observational constraints from the stacks. We also find that slope calculated with an inner limiting radius of R_{80} agrees most consistently with the predictions from the Illustris simulations.

However for the rest of the analysis, we calculate the outer slope using an inner limiting radius of R_{90}. As seen in Figure 3.14, the outer slope calculated in such a way is most sensitive to change with rest to the halo mass. It also has the advantage that outer slope is calculated external to other internal properties of the galaxy like concentration (R_{90}/R_{50}).
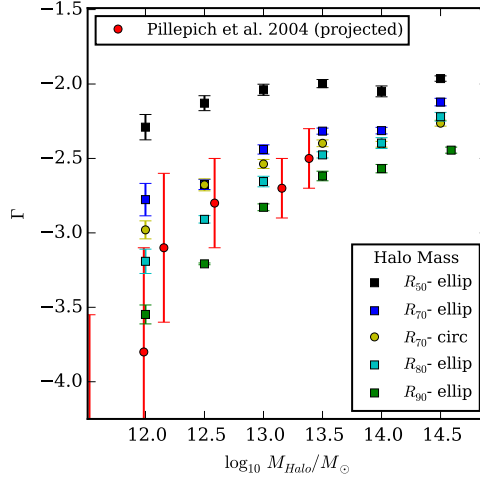
Figure 3.14: The outer slope of the surface brightness profile $\Gamma = d(\log_{10} I)/d(\log_{10} R)$ in bins of halo mass calculated calculated from R_{50}, R_{70}, R_{80} and R_{90} onwards in elliptical bins. Also show is the outer slope calculated in circular bins from R_{70} onwards. The red circles indicated the 2d projections of the predictions of the outer slope of galaxies derived from the Illustris simulations along with their scatter (Pillepich et al. 2014).

Outer slope as a function of halo mass and stellar mass

Similar to the outer light fraction, we now study the outer slope (Γ) as a function of halo mass and stellar mass in Figure 3.15. We consider the galaxy stacks described in Section 3.4.1. In the right panel of Figure 3.15, we find that the outer slope becomes shallower with halo mass. There are three distinct regimes in the Γ-M_{halo} relationship. Apart from the distinction of galaxies below and above the characteristic mass, we find that for galaxies above $\log M_{halo} > 13.7$ (marked in black in Figure 3.15), there is essentially no relationship between the outer slope and halo mass. The rate of increase of the outer slope with halo mass is faster below the characteristic mass than above the characteristic mass. Similar trends are also seen in the Γ-M_* relationship.

For galaxies above the characteristic mass and below $\log M_{halo} < 13.7$, we find that the residuals from the M_*-Γ fit correlate more strongly with M_{halo} than the residuals from the M_{halo}-Γ fit with M_* (a Pearson coefficient of 0.186 vs 0.056). Similarly, by examining the residuals of the fits for galaxies below the characteristic mass, we find that outer slope correlates more with halo mass than stellar mass (a Pearson coefficient of -0.136 vs 0.074). This implies that the primary relationship is between the outer slope and the halo mass in the mass ranges considered. The decrease in significance below the characteristic mass, implies that the outer slope is also dependent on another quantity. We explore this in the next subsection.

Figure 3.15: Top panels: The outer slope of SDSS stacks as a function of stellar mass (left) and halo mass (right) respectively in two regimes: Galaxies above and below the characteristic mass ($\log M_{halo} \sim 12.5$) are shown on the right and left of each plot respectively in different colour schemes. The dashed lines indicates the best fit of the relationship between the outer slope and stellar mass/halo mass in the respective regime. Bottom left: The residuals from the best fitting $\Gamma - \log(M_*)$ relation are plotted as a function of $\log(M_{Halo})$. Bottom right: The residual of the best fitting $\Gamma - \log(M_{Halo})$ relation are plotted as a function of $\log(M_*)$. The Pearson coefficient of the residuals are also indicated in the lower panels for each of the mass ranges considered.
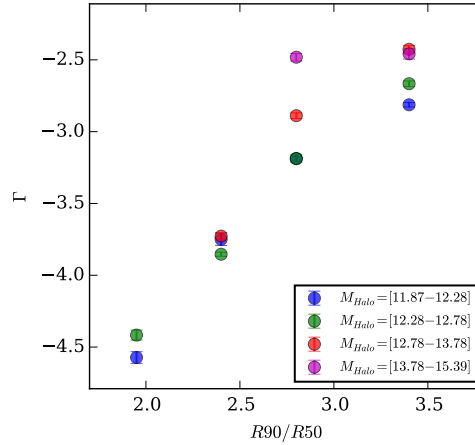
Figure 3.16: Outer slope ($\Gamma = d(\log_{10} I)/d(\log_{10} R)$) of the surface brightness distribution in bins of halo mass and concentration from SDSS stacks.

Outer Slope as a function of halo mass and concentration

In Figure 3.16, we study how the outer slope varies as a function of halo mass and concentration. The outer slope is a stronger function of concentration than halo mass. For a given halo mass, lower concentration galaxies have a steeper slope than high concentration galaxies. For the lowest halo mass bin, the outer slope Γ ranges from -4.6 to -2.8. By comparing Figures 3.16 and 3.15, we find that for the lowest halo mass bins, the outer slope is a stronger function of concentration than stellar/halo mass. The transition in populations from lower to higher concentration galaxies with increasing halo mass gives rise to the smooth trends of the outer slope with halo mass seen earlier.

The large change in the outer slope as a function of concentration is much larger than the variation with other quantities considered. In Figure 3.17, we see that the outer slope is also a strong function of stellar mass surface mass density. For the lowest halo mass bin, the outer slope increases from -4.6 to -3.2 with increasing stellar mass surface mass density. The outer slope is a slow increasing function of central velocity dispersion. Galaxies with low $(u-r)^{0.1}$ colour have steeper slopes than galaxies with high $(u-r)^{0.1}$ colour. Similarly galaxies with low central D4000 (younger stellar populations) have steeper slopes than galaxies with higher central D4000 (older stellar populations).

3.4.3   Outer ellipticity

We derive ellipticity (1-b/a) profiles by fitting contours to the surface brightness distribution of the final galaxy stacks. We recall that we orient the galaxies to be stacked according to distribution of light (second order moments of the intensity distribution) in the inner part of the galaxy. Interpreting the outer ellipticity profiles derived from galaxy stacks is
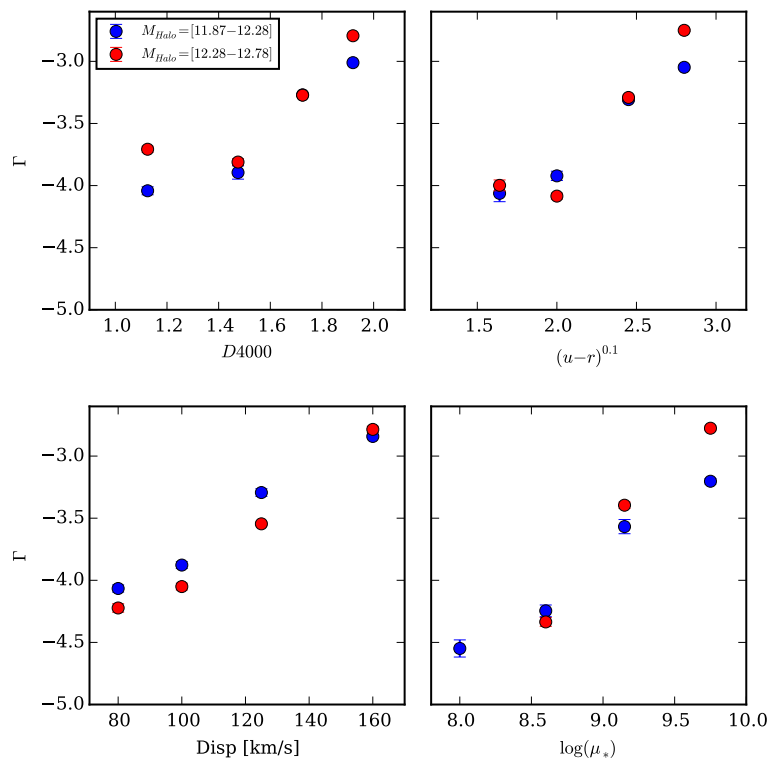
Figure 3.17: Outer slope of the surface brightness distribution of SDSS stacks as a function of central D4000, $(u-r)^{0.1}$, central dispersion and surface mass density for the two lowest halo mass bins.

not a simple task, given the axial ratio cuts used to construct the sample of galaxies to be stacked. In general, the final outer ellipticity of the stacks yields limited information of the intrinsic ellipticity distribution. It is a product of the distribution of the intrinsic ellipticity profiles of the individual galaxies and the orientation of their stellar halo with respect to the distribution of light in the inner part of the galaxy. Detecting a net outer ellipticity in the final stacks implies that the outer stellar halo of the individual galaxies is elliptical and that the outer stellar halo is oriented in the same direction as the inner distribution of light in the galaxy. On the other hand, a near-zero outer ellipticity in the outer stacks implies that either the stellar halo of galaxies are intrinsically circular or that the outer stellar halo is not oriented with the inner light distribution of the galaxy.

In this subsection, we parametrize the outer ellipticity from the profiles by calculating the mean of the ellipticity between $2 * R_{90}$ to $3 * R_{90}$, which is well in the dark-matter dominated regime of the surface brightness distribution.

Outer ellipticity as a function of halo mass and stellar mass

We now study the outer ellipticity as a function of halo mass and stellar mass in Figure 3.15. We consider the galaxy stacks described in Section 3.4.1. We find that the outer ellipticity is a increasing function of both stellar mass and halo mass. By employing a similar technique used earlier of fitting linear relations between the outer ellipiticity and stellar/halo mass and examining the residuals, we find that both above and below the characteristic mass, the outer ellipticity is a stronger function of stellar mass than halo mass in both regimes. By comparing the Pearson residuals, we also find that the outer ellipticity is a stronger function of stellar mass below the characteristic mass than above it. This implies that some aspect of baryonic physics affects the average outer ellipticity of a galaxy stack.

Outer ellipticity as a function of halo mass and concentration

In Figure 3.19, we indicate the net outer ellipticity as a function of halo mass and concentration. The radial ellipticity profiles are similar to those obtained in Figure 4 of D'Souza et al. (2014). The outer ellipticity is a strong function of both halo mass and concentration. For a given halo mass, the net outer ellipticity increases with concentration. Similarly for a given concentration, the net outer ellipticity increases with halo mass.

For the lowest halo mass bin, the largest variation in net outer ellipticity of the stack is obtained as a function of concentration. In Figure 3.20, we see that similar variations are also found for $(u - r)^{0.1}$, central D4000 and central dispersion. On the other hand, the net outer ellipticity is a weak function of surface mass density.

We conclude that there is limited evidence that galaxies with high halo mass and high concentrations have elliptical stellar haloes which are aligned with the inner light distribution of the galaxy.
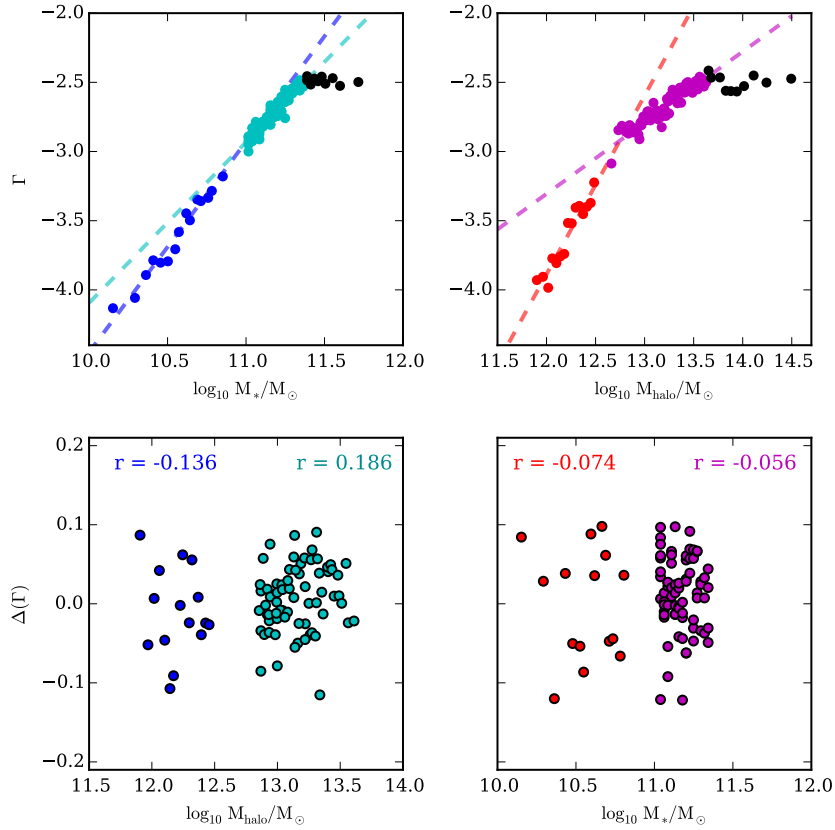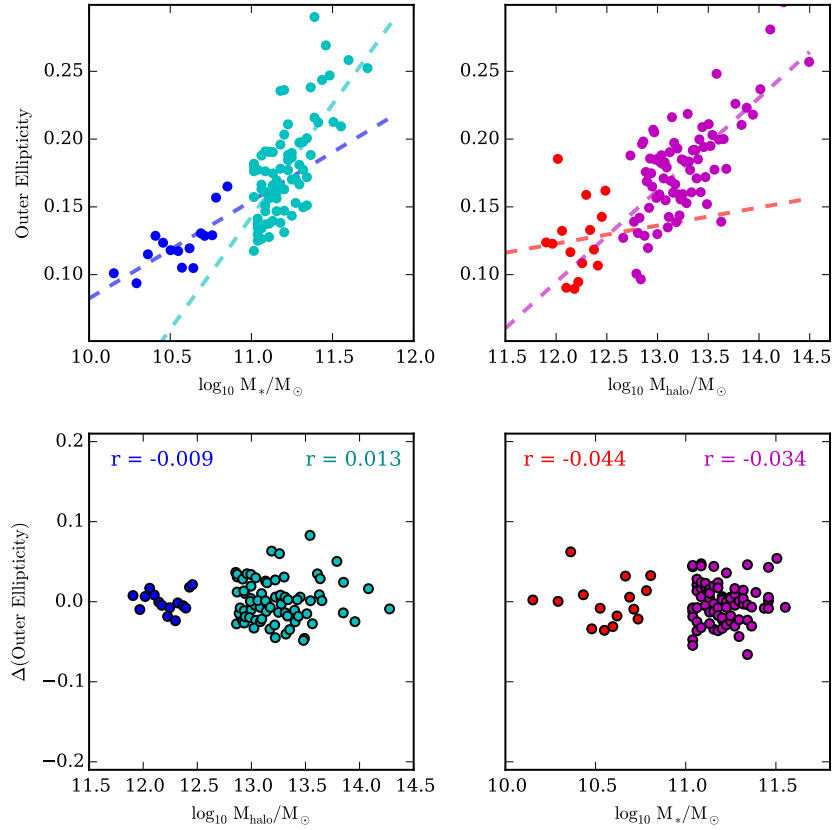
Figure 3.18: Top panels: The outer ellipticity of SDSS stacks as a function of stellar mass (left) and halo mass (right) respectively in two regimes: Galaxies above and below the characteristic mass ($\log M_{halo} \sim 12.5$) are shown on the right and left of each plot respectively in different colour schemes. The dashed lines indicates the best fit of the relationship between the outer ellipticity and stellar mass/halo mass in the respective regime. Bottom left: The residuals from the best fitting $Ellip - \log(M_*)$ relation are plotted as a function of $\log(M_{Halo})$. Bottom right: The residual of the best fitting $Ellip - \log(M_{Halo})$ relation are plotted as a function of $\log(M_*)$. The Pearson coefficient of the residuals are also indicated in the lower panels for each of the mass ranges considered.
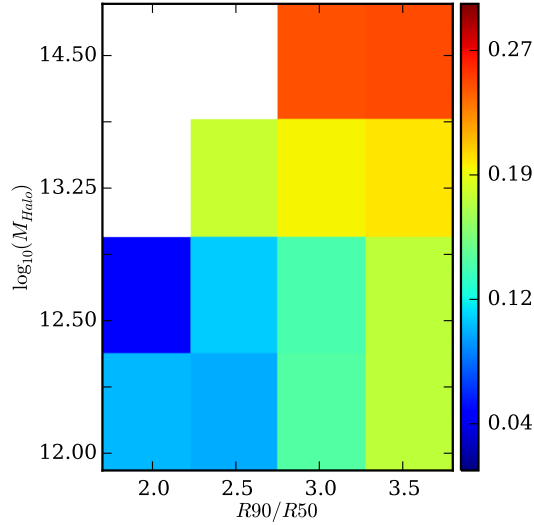
Figure 3.19: Outer Ellipticity ($> R_{90}$) of SDSS stacks in bins of halo mass and concentration. b) Outer Ellipticity ($> R_{70}$) of SDSS stacks in bins of halo mass and surface mass density.

3.4.4 g-r colour gradients

Examining the g-r colour profiles of the galaxy stacks allows us to probe in a limited way the stellar populations which make up the halo. We find similar g-r colour profiles as a function of halo mass and galaxy type as was obtained in Figure 7 of D'Souza et al. (2014). In general, the g-r colour of the outer stellar populations is redder than the central populations. Clear distinctions arise in the g-r colour profile of low-concentration and high concentration galaxies. Low concentration galaxies have a sharp inner g-r colour gradient, while high-concentration galaxies have a gentle g-r colour gradient, which flattens out at larger radii (out to 70-100 kpc).

For a given halo mass, we find that the gradient in g-r colour is also a smooth function of concentration. In Figure 3.21, we show the gradient in g-r colour calculated between the the inner (within R_{20}) and outer (beyond R_{70}) regions in bins of halo mass and concentration. In the lowest halo mass bin, the lowest concentration stacks have the steepest g-r colour gradient. The g-r colour gradient becomes shallower with increasing halo mass.

3.4.5 Summary

In the previous subsections, we studied the average properties of the stellar haloes of galaxies by stacking similar galaxies together. We characterize the stellar halo of the galaxy by calculating the fraction of light in the outer stellar component and its outer slope of its surface brightness profile. In addition, we also calculate the outer ellipticity
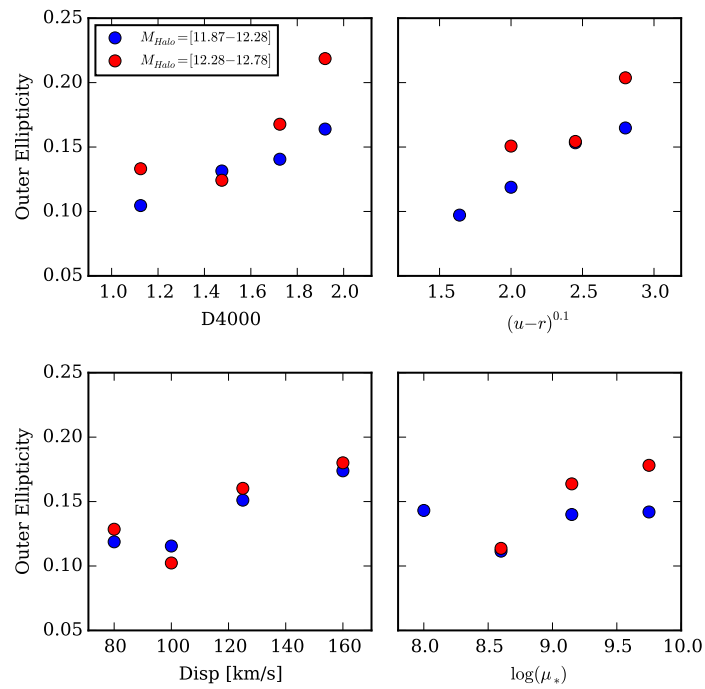
Figure 3.20: Outer net ellipticity of SDSS stacks as a function of central D4000, $(u - r)^{0.1}$, central dispersion and surface mass density for the two lowest halo mass bins.
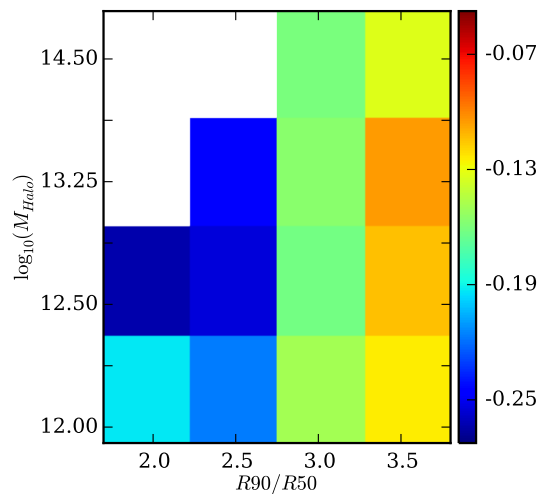
Figure 3.21: Gradients in g-r colour of SDSS stacks in bins of halo mass and concentration.

and the outer slope of the *g-r* colour profile. We summarize the main results of our findings.

1. Above the characteristic mass ($\log M_{halo} \sim 12.5$) in the stellar-halo mass relationship, we find that the outer light fraction is a stronger function of halo mass than stellar mass.

2. The rate of increase of the outer light fraction with halo mass is stepper below the characteristic mass than above the characteristic mass.

3. Below the characteristic mass, the outer light fraction is a stronger function of concentration than halo mass. For galaxies with halo mass $\log M_{halo} \sim 12.5$, the outer light fraction ranges from 15% to 60% with increasing concentration.

4. At a given halo mass, the outer light fraction is a weaker function of the age of the central stellar populations and the sSFR. In general, galaxies with higher central dispersion, redder $(u - r)^{0.1}$ colours , high surface mass density and older stellar population have higher outer light fractions than galaxies with lower central dispersion, bluer $(u - r)^{0.1}$ colours, low surface density and younger stellar populations.

5. The outer slope of the surface brightness profile is an increasing function of halo mass. Above $\log M_{halo} > 13.7$, there is no relationship between the outer slope and halo mass. For galaxies $\log M_{halo} < 13.7$, the outer slope is a stronger function of halo mass than stellar mass. However below the characteristic mass, the outer slope is a stronger function of the concentration of the galaxy than halo/stellar mass.

6. The outer ellipticity profiles of the galaxy stacks is a stronger function of stellar mass than halo mass. The outer ellipticity is also a strong function of concentration of the galaxy. This implies that galaxies with higher concentrations and higher halo mass have elliptical stellar haloes aligned with the inner light distribution of the galaxy.

7. The *g-r* colour gradients becomes shallower with increasing concentration.

3.5 Comparison with Simulations

3.5.1 Predicted Accreted Mass Fractions

In Section 3.4, we showed that there is a qualitative change in the relationship between the outer light fraction and halo mass before and after $\log M_{halo} \sim 12.5$. Qualitatively this agrees with the behaviour of the accreted mass fraction (f_{acc}) with halo mass. If galaxies accrete the majority of their stellar mass from subhaloes of mass $M_{sat} \sim 0.05 - 0.1 \, M_{host}$ (Purcell et al., 2007), then because of the reduced rate of star formation efficiency for galaxies below the characteristic mass (higher M/L ratio), the fraction of the accreted amount of stellar material will be lower than above the characteristic mass. This gives rise to the difference in the rate of growth of the accreted fraction with halo mass below and above the characteristic mass.

In Figure 3.22, we demonstrate that for the Illustris galaxies above the characteristic mass ($\log M_{halo} \geq 12.5$ and $\log M_* \geq 11.0$), the accreted mass fraction (f_{acc}) is more strongly correlated with the halo mass than the stellar mass. Similar to Figure 3.9, we quantify the correlation between the accreted mass fraction with stellar mass and halo mass of the Illustris galaxies by fitting linear relations between them. We find that the residuals from the M_*-f_{acc} fit correlate more strongly with M_{halo} than the residuals from the M_{halo}-f_{acc} fit with M_* (a Pearson coefficient of 0.245 vs -0.019).

In Figure 3.22, we also compare the relations between M_*-f_{acc} (dashed line) and M_*-f_{outer} (dotted line) obtained from Figure 3.9. We find although the slopes are the same, there is a slight offset in the two relationships. Similarly, we can also compare the relationship between M_{halo}-f_{acc} and M_{halo}-f_{outer}. We find that the former is much steeper than the latter. This could be due to the difference in cosmology assumed for the Yang et al. group finder (WMAP3 $\Omega_m = 0.24$,$\Omega_\Lambda = 0.76$) and the Illustris simulations (WMAP9 $\Omega_m = 0.272$, $\Omega_\Lambda = 0.727$). Assuming a WMAP9 cosmology, the Yang et al. group finder would assign a larger halo mass to each group, since there are more massive halos in a WMAP9 cosmology than a WMAP3 cosmology.

In Figure 3.22, we also plot the accreted mass fraction for the Illustris galaxies below the characteristic mass and quantify the relationships between the accreted mass fraction and the stellar mass/halo mass. We find that in constrast to the SDSS galaxies, there is no relationship between the accreted mass fraction and stellar mass for the Illustris galaxies below the characteristic mass. We also find that for the Illustris galaxies the accreted mass fraction is a weaker function of halo mass below the characteristic mass than above it. This is in contrast to the relationship between $f_{outer} - M_{halo}$ derived from SDSS galaxies. This could indicate that the galaxy formation physics at low stellar masses is not correctly modelled in the Illustis simulations.

We also compare the outer light fraction derived from the SDSS stacks with the predicted accreted mass fractions from the Illustris simulations in Figure 3.23 as a function of halo mass and concentration. Overall, we find good qualitative agreement between the trends of the outer light fraction derived from the SDSS stacks and the predicted accreted mass fraction The predicted accreted mass fraction increases as a function of both halo mass and concentration. For a given concentration, the accreted mass fraction increases strongly with halo mass. For a given halo mass, there is an increase in the accreted mass fraction with concentration. For the lowest halo mass bin, the accreted mass fraction increase from 10% to nearly 45% as a function of concentration.

On the other hand, trends in the outer light fraction from the SDSS stacks with surface mass density do not agree with the trends in the predicted accreted mass fraction. As seen in Figure 3.24, for the lowest halo mass bin, the accreted mass fraction decreases with surface mass density, while the outer light fraction from the SDSS stacks increase with surface mass density. This provides further evidence that the galaxy formation physics at low stellar masses is not correctly modelled in the Illustis simulations.
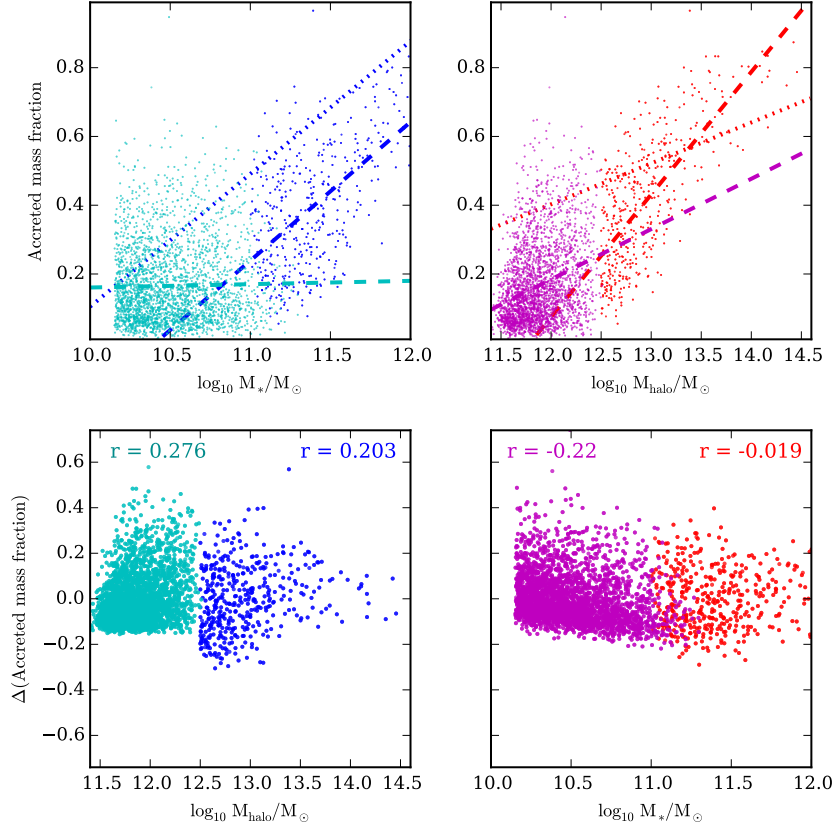
Figure 3.22: Top panels: The accreted mass fractions of Illustris galaxies as a function of stellar mass (left) and halo mass (right) respectively in two regimes: galaxies above and below the characteristic mass ($\log M_{halo} \sim 12.5$) are shown on the right and left of each plot respectively in different colour schemes. The dashed lines represent the best fit of the accreted mass fraction with stellar mass / halo mass. We also overplot the relationship of the outer light fraction as a function of stellar mass and halo mass from Figure 3.9 for galaxies above the characteristic mass. Bottom left: The residuals from the best fitting $f_{acc} - \log(M_*)$ relation are plotted as a function of $\log(M_{Halo})$. Bottom right: The residual of the best fitting $f_{acc} - \log(M_{Halo})$ relation are plotted as a function of $\log(M_*)$. The Pearson coefficient of the residuals are also indicated in the lower panels for each of the mass ranges considered.
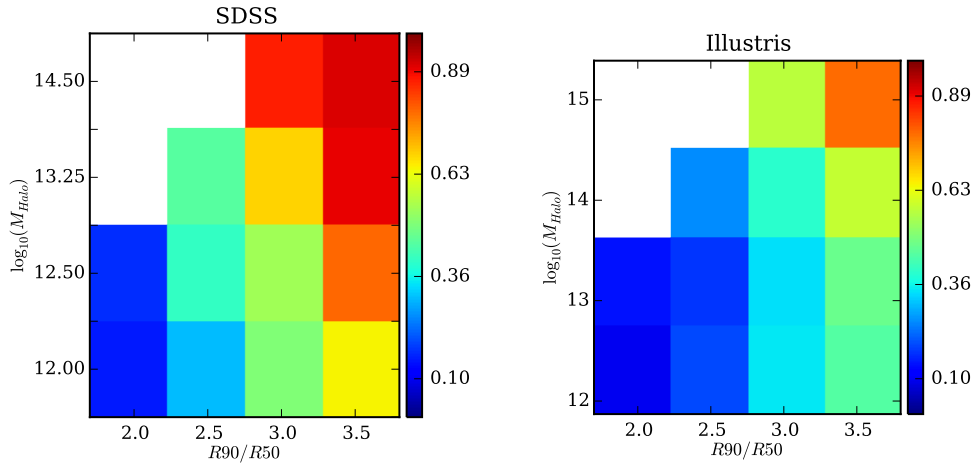
Figure 3.23: Comparison of the outer light fraction from the SDSS stacks (left) and the predicted accreted mass fractions from the `Illustris` simulations (right) in bins of halo mass and concentration.
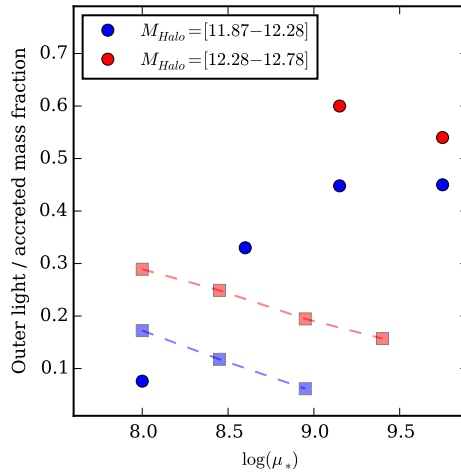
Figure 3.24: Comparison of the outer light fraction from the SDSS stacks (circles) and the predicted accreted mass fractions from the `Illustris` simulations (squares) as a function of surface mass density.
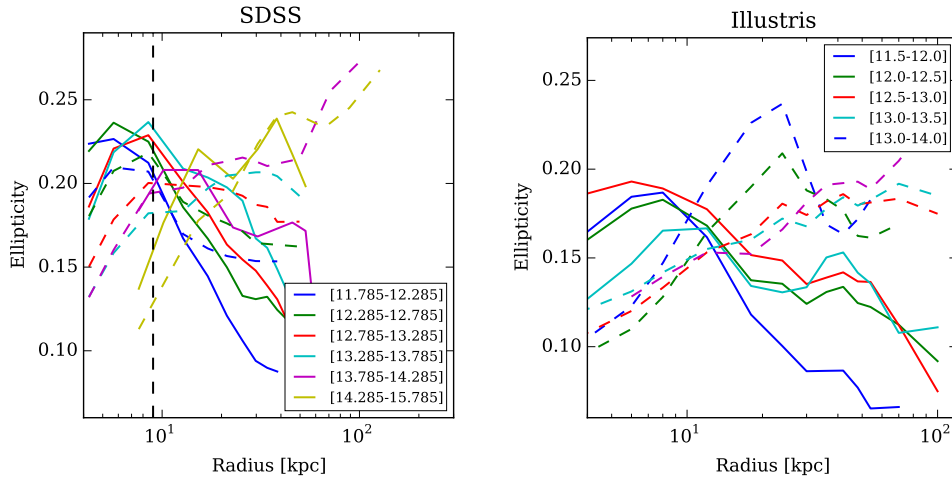
Figure 3.25: Comparison of the ellipticity profiles of stacks of early-type (dashed) and late-type (solid) galaxies from SDSS (left) and the Illustris simulations (right).

3.5.2   Ellipticity Profiles of Galaxies

Ellipticity profiles derived from stacks of mock galaxies from the Illustris simulations reproduce qualitatively the trends seen in the data (see Figure 3.25). Stacks of early-type galaxies tend to be elliptical in the outskirts as compared to stacks of late-type galaxies which are circular in the outskirts. In order to interpret the ellipticity profiles of the mock stacked galaxies, we parametrize the 3D ellipticity of the stellar haloes and the data matter of galaxies in the Illustris simulations by calculating the reduced moment of inertia tensor,

$$I_{ij} = \sum_k \frac{r_{k,i} r_{k,j}}{r_k^2},$$ (3.1)

in spherical shells with radii 0, 30, 60 and 100 kpc, which we then diagonalize. The spherical shells were chosen such that the inner shell probes the insitu component, while the outer component probes the accreted component. The axis ratios a,b and c are the square roots of the eigenvalues ($a \geq b \geq c$), and the eigenvectors give the directions of the principal axes. To calculate the error in the axis, we perform a bootstrap analysis of the particles in each shell by randomly sampling the particles allowing for duplication and repeating the exercise a 100 times.

To characterise the orientation and the ellipticity of the stellar halo, we calculate the angle ($\cos \beta$) between the major axis of the inner (0-30 kpc) and outer shell (60-100 kpc). We also calculate the (c/a) ratio of the outer shell for both stellar material and dark matter. The calculation of the c/a ratio in spherical shells instead of ellipsoid shells biases the derived axis ratio towards spherical. We follow Bailin & Steinmetz (2005) in correcting the axis ratio against this bias:

$$(c/a)_{true} = (c/a)_{measured}^{\sqrt{3}}$$ (3.2)
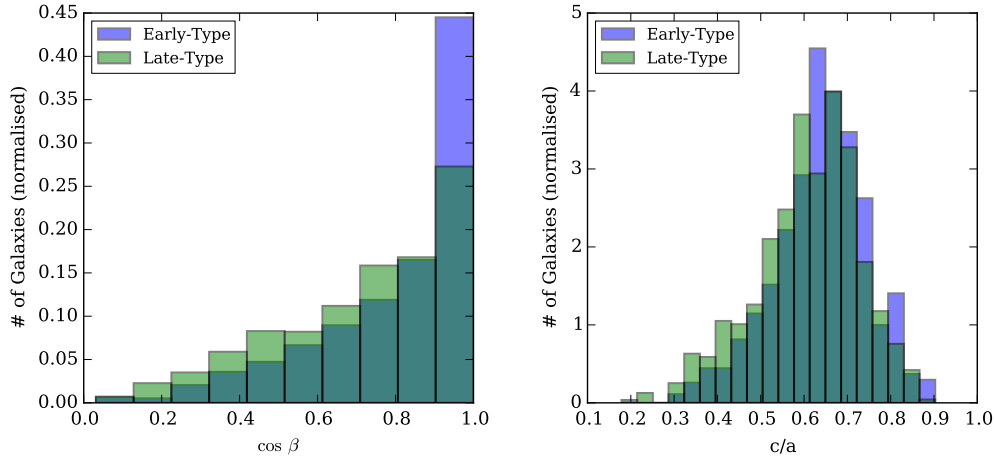
Figure 3.26: a) Histogram of the difference in angle between the inner (0-30 kpc) and outer (60-100 kpc) part of the galaxy for early and late-types from the Illustris simulations. b) Histogram of the ellipticity (expressed in c/a) of the outer part (60-100 kpc) of the galaxy for early and late-types.

In Figure 3.26, we show the distribution in the orientation and ellipticity of the stellar halo of early and late-type galaxies in the halo mass range $12.0 \leq \log(M_{halo}/M_{\odot}) \leq 14.0$. We plot only those measurements which can be determined to an accuracy of 33%. In the left panel, we show the angle ($\cos \beta$) of separation between the major axis of the inner and outer most shell for late-type and early-type galaxies. Early-type galaxies have preferentially a larger number of galaxies where the stellar halo is aligned with inner light distribution of the galaxy. On the other hand, late-type galaxies have a sizeable number of galaxies which are misaligned with the inner light distribution. 80% of late-type galaxies have $\cos \beta < 0.9$ as compared to 55% for early-type galaxies.

The right panel of Figure 3.26 shows the distribution of c/a between late-type and early-type galaxies in the outer shell (60-100 kpc). Although the distributions appear similar, late-type galaxies have a larger number of galaxies with lower c/a. This hints to the evidence that disrupting satellites and streams often get aligned with the disk.

Using the particle data from the Illustris simulations, we conclude that the stellar halo of both mock late-type and early-type galaxies are elliptical. However, the stellar halo of early-type galaxies tend to be aligned with the inner light distribution of the galaxy than late-type galaxies. The preferential misalignment of the outer stellar halo of late-type galaxies over early-types could explains the ellipticity profiles in the stacked SDSS galaxies.

3.5.3 Age and Metallicity Profiles

We derive median age and metallicity profiles in bins of halo mass and galaxy type in Figure 3.27 from the Illustris simulations. We also derive light-weighted (r-band) age and

metallicity profiles. The age and metallicity profiles are constructed in a similar way as the *g-r* colour profiles from the SDSS stacks to enable direct comparison. We note that the Illustris simulations uses a Chabrier IMF.

The median metallicity of both late and early types decreases as a function of radius. The rate of decrease in metallicity steepens after a transition radius. The transition radius from a slow decrease to faster decrease in metallicity is smaller for late-types than early types. The transition radius also increases with increasing halo mass. High-mass early type galaxies show a gentle decrease in metallicity out to a large radius (~ 50 kpc).

On the other hand, the median age profiles of the galaxies show marked differences between early and late-types. In general, the population of stars at large radii is older for both early and late type galaxies. For lower mass late-type galaxies, there is a general decrease in median look-back time until it reaches a minimum and increases thereafter. This minimum in the median age occurs around 10 kpc, suggesting recent star formation out in the disk. Large early type galaxies have a flat age gradient out to 45 kpc, and a steep increase thereafter.

The light-weighted age and metallicity profiles show similar trends. The transitions in the characteristic shapes of the median metallicity and age profiles seem to be driven by the acccreted populations. In general, the outer stellar populations of the halo are metal poor and have large median ages. Both the upturn in median age and decrease in metallicity occur at the same radius. For early-type galaxies, this transition radius is not correlated with R_{acc}, the radius where the accreted population begins to dominate the surface brightness profiles.

The integrated light from the *g* and the *r* bands is dominated by light from younger stellar populations. The characteristic decrease in *g-r* colour followed by an upturn in late-type galaxies can be possibly explained by a similar upturn in age gradients. On the other hand, the gentle decrease in *g-r* colour in early-type galaxies seems to be driven by metallicity gradients, given the flat age gradients out to large radii in early type galaxies. The flattening and upturn in the *g-r* colour in late-type and early-type galaxies is driven by increasing age at larger radii. Further tests are required to test if the radial trends in *g-r* colour are indeed a direct consequence of the radial profiles of age and metallicity.

3.6 Discussion and Conclusions

After demonstrating that we can recover upper limits of the accreted light fractions of stacked galaxies within a precision of 0.1 dex by estimating its outer light fraction, we study the properties of the stellar halo of galaxies as a function of their halo mass. These halo masses were estimated by Yang et al. (2007) from the characteristic stellar mass of the galaxy group. They also provide estimates of the halo mass from the characterstic luminosity of the galaxy group ($L_{19.5}$). The characteristic luminosity of a group is the combined luminosity of all galaxies in a group whose luminosities are $M_r^{0.1} - 5\log \leq -19.5$. The characteristic stellar mass of a group is the corresponding combined stellar mass of all galaxies in the group defined in a similar manner. The main uncertainty in the estimated
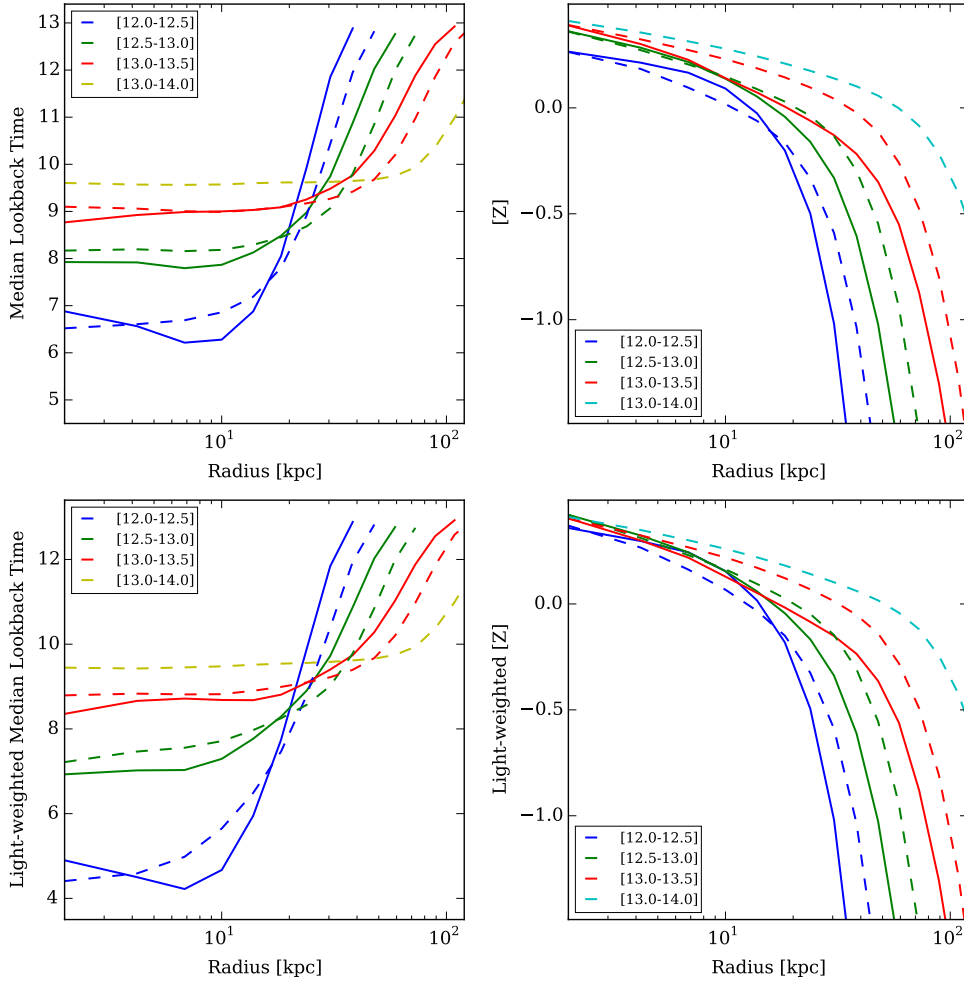
Figure 3.27: (a & b) Age and metallicity profiles from galaxy stacks from the Illustris simulations in bins of halo mass and galaxy type. Solid lines are late-type while dashed lines represent early-types. (c & d) Luminosity weighted age and metallicity profiles from galaxy stacks in bins of halo mass and galaxy type.

halo masses comes from the intrinsic scatter between the halo mass and the characteristic luminosity (stellar mass) of the group, which is about 0.2 dex. The scatter between the halo mass estimated from the characteristic luminosity ($L_{19.5}$) and the characteristic stellar mass is much smaller than 0.2 dex.

We find observational evidence that the accreted light fractions derived from SDSS stacks is a stronger function of halo mass than stellar mass (MPA-JHU) above log $M_{halo} \sim$ 12.5, which agrees with theoretical predictions (Purcell et al., 2007; Cooper et al., 2013). The accreted stellar fraction reflects the amount of disrupted satellites accreted onto the galaxy which is a strong function of halo mass. The drop in the observed accreted fractions below the turn-off halo mass (log $M_{halo} \sim$ 12.5) reflects the high M/L ratio of accreted dwarf satellite galaxies. Similar trends are also seen in the Illustris simulations.

For a given halo mass, there is a considerable spread in the amount of stellar matter accreted by the galaxy. This results in a corresponding spread in the estimated accreted fractions and outer slope. In this work, we find that for galaxies below the characteristic mass, this spread in accreted fraction is most correlated with the morphological shape of the galaxy parametrized by its concentration (Figures 3.23). We find similar relationship between the accreted mass fraction and the concentration of the galaxies in the Illustris simulations. Our results imply that the physical processes responsible for the accretion of the stellar material and the formation of the stellar halo are directly related to the morphological shape of the galaxy and not to the age of the central stellar populations or its star formation rate. This also agrees well with the findings of Rodrigues-Gomez et al. (2015) who find that the accreted mass fraction of galaxies from the Illustris simulations are weakly dependent on the stellar age, colour and star formation, but strongly dependent on morphology, halo formation time and recent merger history. However the lack of increase of the accreted stellar mass fraction with stellar mass for galaxies below the characteristic mass indicates that the Illustris simulations fail to account for all the relevant physical processes responsible for in-situ star formation.

We confirm the outer slope becomes shallower with increasing halo mass as predicted by Pillepich et al. (2014). Shallower slopes indicate higher accreted fractions. At higher halo masses, while there is a weak increase in the outer slope with increasing halo mass, the increasing accreting fraction reflects in larger effective radius and deviations in the surface brightness profile at large radii. This may indicate the inside-out growth of the outer stellar halo.

Comparision with mock images from the Illustris simulations allows us to intepret the ellipticity profiles of the galaxy stacks. We find that the stellar halo of early-type galaxies are more aligned with the inner light distribution of the galaxy than late-types. This is consistent with the findings of large-survey studies showing that red galaxies are preferentially aligned with their haloes while blue galaxies have a more isotropic distribution (Yang et al., 2006; Brainerd, 2005). The presence of such misalignment for late-type galaxies is intriguing. Recently, Debattista et al. (2015) have suggested that the presence of gas cooling on to the disk could explain the misalignment found in gas-rich late-type galaxies.

Chapter 4

The Massive End of the Stellar Mass Function

Note: This chapter has been published in Monthly Notices of the Royal Astronomical Society *(D'Souza et al., 2015).*

4.1 Introduction

The stellar mass function of galaxies is a basic probe of galaxy formation and evolution enabled by large redshift surveys. In recent years, major advances have been made by large redshift surveys, such as the 2dF Galaxy Redshift Survey and the Sloan Digital Sky Survey (SDSS), in estimating the stellar mass function in the low-redshift Universe (Cole et al., 2001; Bell et al., 2003; Blanton et al., 2003). For example, Li & White (2009) have used a uniform sample of almost half a million galaxies from SDSS DR7 to derive the stellar mass function at $z = 0.1$. This has been complemented by the effort of the Galaxy and Mass Assembly Survey (GAMA Baldry et al., 2012), which has accurately constrained the faint end slope of the stellar mass function down to stellar masses $\sim 10^8 M_\odot$.

The calculation of the stellar mass function hinges on the proper determination of the stellar mass of a galaxy, which in turn depends critically on the estimation of its total flux in a given pass-band. Systematic differences in the estimation of the stellar mass of a galaxy may arise from different choices of the initial mass function (IMF) and the stellar mass-to-light ratio (M/L), as well as from different estimations of the galaxy total flux. Determining the flux accurately for a large number of galaxies in an all-sky survey is a challenging task. In particular, quantifying the flux in the outer low surface brightness (LSB) regions of a galaxy has proven to be difficult and is still subject of much debate (Bernardi et al., 2013; Simard et al., 2011). These uncertainties mean that the slope at the massive end of the mass function is not very well determined. This has significant implications for several astrophysical problems, including halo occupation models, the mean baryon fraction in the Universe, X-ray and Sunavey-Zeldovich studies of high mass galaxies, and understanding the evolution of massive galaxies to high redshifts.

Different approaches have been employed by SDSS in its photometric pipeline (`PHOTO`) to estimate the total flux of a galaxy. In addition to SDSS `Petrosian` magnitudes, two dimensional models (e.g. exponential or de Vaucouleurs) have been used to model the surface brightness distribution of galaxies (SDSS `Model` magnitudes). Further improvement has been provided by SDSS `cModel` magnitudes, for which fluxes are estimated as a linear combination of an exponential and a de Vaucouleurs model. In recent years, several studies have tried to fit Sérsic and multi-component models to the surface brightness distribution (Simard et al., 2011; Lackner & Gunn, 2012; Bernardi et al., 2013).

Each of these approaches provides a progressively better estimate of the total flux of a galaxy, but they all suffer from the same intrinsic drawback, namely that the models are fits to the central, high signal-to-noise ratio (SNR) regions of the galaxy and assumptions are required about the outer lower SNR (beyond $\mu_r \sim 27\,\mathrm{mag\,arcsec^{-2}}$) part of the galaxy profile. Additionally, the total flux estimated through model fitting can be biased in a number of ways.

The biggest source of systematic bias in the flux determination is related to the estimation of the sky background, especially for large nearby objects or those located in dense environments (von der Linden et al., 2007; Bernardi et al., 2007). In principle, this can be overcome by considering extremely large fields of view. For example, considerable progress has been achieved by Blanton et al. (2011) by fitting the masked sky background for each SDSS scan with a smooth continuous function.

However, even with improvements to the sky background algorithm, one is still limited by the depth of the survey. The relatively short exposure time of SDSS (53.9 secs) limits the accuracy of the background determination and subtraction. This in turn limits ones ability to distinguish between the flux of the outer stellar halo and the sky background, leading to an over- or under-estimation of the total flux of a galaxy. In particular, multi-component model fitting of the main galaxy can lead to biased results. This may explain why recent attempts to trace the low SNR LSB part of a galaxy through fitting multi-component models to single SDSS photometric images have yielded divergent results (Simard et al., 2011; Bernardi et al., 2013; Meert et al., 2015).

Other sources of systematic error in determining the flux of a particular object are the procedures employed for deblending and masking, as well as the radial extent of the models used for the surface brightness fitting. Finally, in addition to photometry, several other effects have a considerable impact on the massive end of the stellar mass function, such as evolutionary corrections and *fiber collisions* (i.e. the fraction of galaxies not targeted for spectroscopy due to the fact that fibres cannot be positioned closer together than 55 arcseconds on the SDSS plug plates).

An alternative but viable approach to fitting models to individual images of galaxies, is to stack images of similar galaxies to quantify the average total amount of extra light in the outer parts (Tal & van Dokkum, 2011; D'Souza et al., 2014). By stacking galaxies as a function of their stellar mass and galaxy-type, we reached a depth of $\mu_r \sim 32\,\mathrm{mag\,arcsec^{-2}}$ (D'Souza et al., 2014). The increased depth of galaxy stacks helps to reliably constrain the total amount of light especially in the LSB component. In addition, the background for stacked galaxies can be determined more accurately. This then provides a direct handle on

the corrections to the `Model` magnitudes as a function of the stellar mass and galaxy type.

In this Chapter, we attempt to derive flux corrections to the `Model` magnitudes and re-derive the galaxy stellar mass function at redshift $z = 0.1$ using MPA-JHU (Max-Planck Institute for Astrophysics & John Hopkins University) stellar masses (Kauffmann et al., 2003) and the sample of Li & White (2009). We estimate corrections to the `Model` magnitudes by stacking volume-limited samples in bins of stellar mass, concentration and model type. We also consider various effects that may systematically bias the stellar mass function.

In Section 4.2, we define the samples used for deriving the corrections as well as the full sample used to derive the stellar mass function. In Section 4.3, we derive the flux corrections to the `Model` magnitudes. In Sections 4.4 and 4.5, we derive the galaxy stellar mass function and the luminosity function respectively. In Sections 4.6 and 4.7, we summarise and discuss our results. Throughout this chapter, we assume a flat ΛCDM cosmology, $\Omega_{\rm m} = 0.25$ and $\Omega_\Lambda = 0.75$. We further assume a Hubble parameter $h = 0.72$ for the calculation of physical distance scales wherever necessary.

4.2   Sample Selection

4.2.1   Sample for Calculating the Mass Function

Following Li & White (2009), we select SDSS spectroscopic galaxies from the NYU-VAGC (New York University - Value Added Catalogue) [1] catalogue (Blanton et al., 2005) with redshifts in the range $0.001 \leq z \leq 0.5$ and `Petrosian` r-band magnitudes in the range $12 \leq m_{rPet} \leq 17.6$.[2] This gives us a total of 533442 galaxies, which are ideal for large scale structure studies. We further pruned the sample to 523476 galaxies by retaining only those galaxies with a valid MPA-JHU stellar mass. We estimate the "effective" survey area to be $6570\,deg^2$ (2.0084 steradians), by taking into account the incompletness and the masked-out regions (due to bright stars) of the survey.

For the stellar mass function, we use the stellar masses provided in the DR7 version of the MPA-JHU catalogue[3], which assumes a universal Chabrier initial stellar mass function (Chabrier 2003).

To derive the luminosity function, we use the r-band absolute `Model` magnitude ($M_{r^{0.1}}$), corrected for evolution and K-corrected to its value at $z_0 = 0.1$ according to the following equation:

$$M = m - DM(z) - K(z; z_0) + Q_e(z - z_0) \,, \tag{4.1}$$

where M is the absolute magnitude, $DM(z)$ is the distance modulus at redshift z, m the apparent magnitude, $K(z; z_0)$ is the K-corrections relative to a passband blue-shifted by z_0 and the luminosity e-correction is parametrised linearly by Q_e. The K-corrections were calculated using the code `Kcorrect v4_3` (Blanton & Roweis, 2007). In general, we assume

---

[1]Available at http://sdss.physics.nyu.edu/vagc/ .

[2]We also include the three survey strips in the Southern Cap.

[3]Available at http://www.mpa-garching.mpg.de/SDSS/DR7/
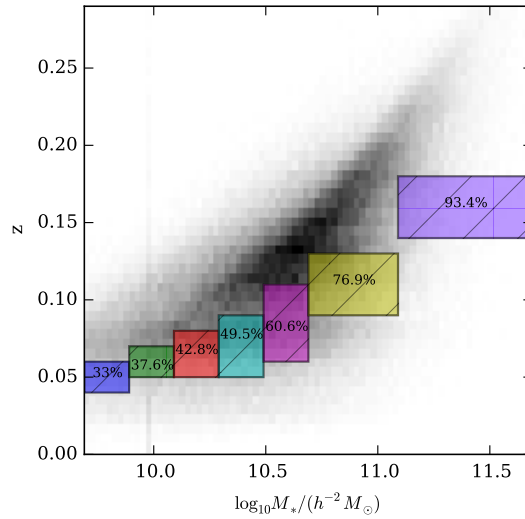
Figure 4.1: Volume-limited samples used for stacking: Shaded contours show the distribution of the parent sample galaxies in the plane of stellar mass versus redshift. The seven coloured boxes indicate the redshift limits of the seven stellar mass sub-samples. These sub-samples are further divided by concentration (C) (not shown in the figure). The numbers in the coloured boxes indicate the fraction of centrals in these volume limited stellar mass sub-samples.

a uniform luminosity evolutionary correction of $Q_r = 1.62$ as derived by (Blanton et al., 2003).

4.2.2   Sample for Determining the Flux Corrections

To derive the corrections to the `Model` magnitudes, we stack volume-limited sub-samples of isolated galaxies defined from the parent sample in various ranges of stellar mass, concentration ($R90/R50$) and redshift (See Table 4.1). In each sub-sample, galaxies that were better fit by an exponential (`Exp`) or a de Vaucouleurs (`deV`) model by the SDSS pipeline (defined by comparing the likelihood values of the model fits from the SDSS `PhotoObjAll` database) were stacked separately.

We select isolated galaxies by requiring that there are no brighter companions in the spectroscopic sample within $R \leq 1\,\mathrm{Mpc}$ (where R is the projected comoving separation) and $|\delta z| < 1000\,\mathrm{km\,s^{-1}}$.

In Figure 4.1, the redshift limits of the various stellar mass sub-samples are shown projected along the plane of stellar mass versus redshift of the parent NYU-VAGC sample. The fraction of centrals in each stellar mass sub-sample are also shown.

Table 4.1: Volume-limited samples of isolated galaxies selected by stellar mass from the NYU-VAGC sample for the purpose of stacking

.

Sample	Stellar mass	Concentration	Redshift	$N_{gal\,\mathrm{Exp}}$	$N_{gal\,\mathrm{deV}}$
A1	$9.69 < \log(M_*/M_\odot) < 9.89$	$1.7 < C < 2.5$	$0.04 < z < 0.06$	797	117
A2	$9.69 < \log(M_*/M_\odot) < 9.89$	$2.5 < C < 3.3$	$0.04 < z < 0.06$	66	501
B1	$9.89 < \log(M_*/M_\odot) < 10.09$	$1.7 < C < 2.5$	$0.05 < z < 0.07$	1028	175
B2	$9.89 < \log(M_*/M_\odot) < 10.09$	$1.7 < C < 2.5$	$0.05 < z < 0.07$	83	1111
C1	$10.09 < \log(M_*/M_\odot) < 10.29$	$1.7 < C < 2.1$	$0.05 < z < 0.08$	638	15
C2	$10.09 < \log(M_*/M_\odot) < 10.29$	$2.1 < C < 2.5$	$0.05 < z < 0.08$	752	308
C3	$10.09 < \log(M_*/M_\odot) < 10.29$	$2.5 < C < 2.9$	$0.05 < z < 0.08$	121	1499
C4	$10.09 < \log(M_*/M_\odot) < 10.29$	$2.9 < C < 3.3$	$0.05 < z < 0.08$	2	1071
D1	$10.29 < \log(M_*/M_\odot) < 10.49$	$1.7 < C < 2.1$	$0.05 < z < 0.09$	342	38
D2	$10.29 < \log(M_*/M_\odot) < 10.49$	$2.1 < C < 2.5$	$0.05 < z < 0.09$	534	535
D3	$10.29 < \log(M_*/M_\odot) < 10.49$	$2.5 < C < 2.9$	$0.05 < z < 0.09$	89	1468
D4	$10.29 < \log(M_*/M_\odot) < 10.49$	$2.9 < C < 3.3$	$0.05 < z < 0.09$	1	2153
E1	$10.49 < \log(M_*/M_\odot) < 10.69$	$1.7 < C < 2.1$	$0.06 < z < 0.11$	239	74
E2	$10.49 < \log(M_*/M_\odot) < 10.69$	$2.1 < C < 2.5$	$0.06 < z < 0.11$	555	1093
E3	$10.49 < \log(M_*/M_\odot) < 10.69$	$2.5 < C < 2.9$	$0.06 < z < 0.11$	72	1981
E4	$10.49 < \log(M_*/M_\odot) < 10.69$	$2.9 < C < 3.3$	$0.06 < z < 0.11$	-	1867
F1	$10.69 < \log(M_*/M_\odot) < 11.09$	$1.7 < C < 2.1$	$0.09 < z < 0.13$	199	264
F2	$10.69 < \log(M_*/M_\odot) < 11.09$	$2.1 < C < 2.5$	$0.09 < z < 0.13$	303	1510
F3	$10.69 < \log(M_*/M_\odot) < 11.09$	$2.5 < C < 2.9$	$0.09 < z < 0.13$	76	2919
F4	$10.69 < \log(M_*/M_\odot) < 11.09$	$2.9 < C < 3.3$	$0.09 < z < 0.13$	1	4180
G1	$11.09 < \log(M_*/M_\odot) < 11.69$	$1.7 < C < 2.1$	$0.14 < z < 0.18$	6	47
G2	$11.09 < \log(M_*/M_\odot) < 11.69$	$2.1 < C < 2.5$	$0.14 < z < 0.18$	11	220
G3	$11.09 < \log(M_*/M_\odot) < 11.69$	$2.5 < C < 2.9$	$0.14 < z < 0.18$	15	792
G4	$11.09 < \log(M_*/M_\odot) < 11.69$	$2.9 < C < 3.3$	$0.14 < z < 0.18$	3	2794

4.3 Flux Corrections to the `Model` magnitudes

In this section, we derive corrections to the original SDSS `Model` magnitudes derived from the standard DR7 photometric pipeline (`photo v5_4`). We first demonstrate that the original SDSS `Model` magnitudes are biased, in agreement with other studies (Simard et al., 2011; Bernardi et al., 2013). We then proceed to derive corrections to the `Model` magnitudes.

4.3.1 Systematic Biases in `Model` magnitudes

The original `Model` are affected by two sources of systematic bias related to over-subtraction of the sky background (von der Linden et al., 2007; Bernardi et al., 2007) and to simplistic choices of the model for the surface brightness profile of the galaxy (exponential or de Vaucouleurs). In this section, we allow for more complex models to describe the light profiles and we also allow the sky background to vary.

We fit 2D axisymmetric models (single Sérsic and double Sérsic models along with a constant background) using the Bayesian analysis described by D'Souza et al. (2014) to individual postage-stamp cutouts of the highest stellar mass and high-concentration galaxies ($11.49 < \log(M_*/M_\odot) < 11.69$, $2.9 < C < 3.3$) in the redshift range $0.14 < z < 0.18$ (covered by the sample G4 above - 38 galaxies) and $0.2 < z < 0.4$ (414 galaxies). The choice of the sample was motivated by the idea of testing the robustness of the `Model` magnitudes in the limits of high stellar mass and high redshift, where the relative contribution due to the sky background becomes increasingly significant.

We compare our best fitting model with the `Model` magnitudes reported by the SDSS `photo v5_4` pipeline. In Figure 4.2, we plot a histogram of $M_{model} - M_{fit}$ for each galaxy. The distribution is broad with a standard deviation of 0.25 magnitudes and is positively skewed. The median is shifted by is 0.03 magnitudes and the mean by 0.08 magnitudes. The large spread in the histogram arises from a degeneracy between the best-fit model and the level of sky background. The results in Figure 4.2 demonstrate that shallow single-exposure SDSS images are insufficient to accurately quantify the total amount of light in massive early-type galaxies to better than 0.25 mag. We also note that estimates of the total flux from a single SDSS image will also be affected by the deblending and masking algorithm [4].

Because of the limitations in estimating total fluxes from single SDSS images, we have chosen to correct `Model` magnitudes using *stacked images*, where the increased signal-to-noise ratio better constrains both the model and the level of sky background.

4.3.2 Stacking images

In order to derive the flux corrections to the `Model` magnitudes, we used the sky-subtracted SDSS Data Release 9 images to create mosaics in the g, r and i bands centred on each

---

[4]In this paper, we follow the deblending and masking technique outlined in Chapter 3
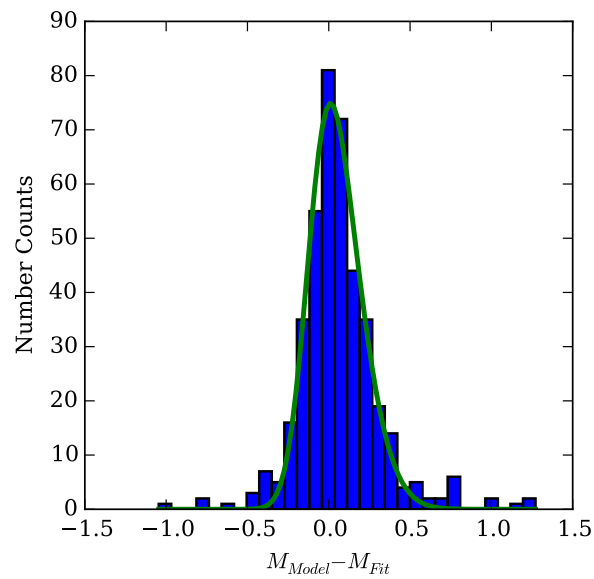
Figure 4.2: Bias in SDSS `Model` magnitudes: A histogram of the difference between the flux derived from our best fit models of high stellar mass high-concentration galaxies and the `Model` magnitudes from DR7 for galaxies with $11.49 < \log(M_*/M_\odot) < 11.69$, $2.9 < C < 3.3$, $0.14 < z < 0.18$ and $0.2 < z < 0.4$. The green solid line indicates the fit to the skewed-normal distribution.

galaxy in the sub-samples defined in Section 4.2.2. The mosaics extend out to radii of 0.6 - 1 Mpc depending on the stellar mass and redshift range. We follow the stacking procedure outlined in Chapter 3 and similar to that used by D'Souza et al. (2014). In short, each mosaic was deblended, masked, corrected for galactic extinction (Schlegel et al., 1998), transformed to the highest redshift in that respective bin, rotated so that the major axis of each galaxy is aligned, and then stacked using the truncated-mean algorithm.[5] The g- and the i- band images were only used to create the final mask along with the r-band images. Conservative masking was used. The final stacking was done using the masked and transformed r-band images.

4.3.3   Measuring the Total Flux of the Stacked Images

Measuring the total integrated flux of a galaxy stack by fitting a model to its light distribution misses a fair amount of light due to the inability of the model to reproduce the bulge/disk component of the inner part of the galaxy. For example, a double Sérsic model can miss upto 0.22 mag near the centre of a galaxy stack. On the other hand, "isophotal" magnitudes are unable to measure the LSB features of the galaxy stack, especially in the low S/N regime.

In order to measure the total integrated light in each stack, we consider, therefore, a hybrid approach between a "model" and an "isophotal" magnitude. In particular, we first fit the large mosaics using two-dimensional axisymmetric double Sérsic models with a flat background using the Bayesian analysis described by D'Souza et al. (2014). During this fit, the inner component is truncated outside a radius equal to $7\,R_e$, while the outer component extends out to infinity. Then, to the flux derived by the double Sérsic model, we add the total residual flux ($=$ `Data`$-$`Model`) within a circular aperture of limiting radius R_{lim}, defined as the radius at which the residual flux is maximised. The advantage of this hybrid approach is that the double Sérsic model measures the slow decline of flux into the low S/N regime, while the sum of the residual and model fluxes reproduces the total flux in the high S/N part of a galaxy stack.

In the next subsections, we explore the different factors that may bias our measurements of the total flux of the stack.

Bias due to Inaccurate Sky Background Subtraction

The sky residuals in the individual SDSS DR9 images are responsible for some small amount of residual sky background in the final stacks ($< 4 \times 10^{-4}$ nanomaggies per pixel). We quantify this residual by adding a flat background component as a free parameter of our models (Section 4.3.3). As show later in Section 4.3.3, this bias is minimal (≤ 0.01 mag).

For the individual DR9 images, Blanton et al. (2011) quantified the spread in the sky background residuals to be $\sigma \sim 3.13 \times 10^{-3}$ nanomaggies per pixel. The median bias in the r-band magnitudes was estimated to be at the most 0.1 mag independent of $R50$. In

---

[5]For the truncated-mean stack, we removed 5% of the extreme minimum and maximum values for each pixel.

addition, higher stellar mass galaxies are found predominately at higher redshifts in the SDSS spectroscopic sample, limiting the bias in the flux of individual images caused by faulty sky-subtraction.

Bias due to Models Used

In order to test how the choice of model may affect the corrections to the total luminosity using the "hybrid" magnitudes, we fit each of our galaxy stack using two-dimensional exponential, de Vaucouleurs, Sérsic and double Sérsic models. Each model also includes a flat sky residual. By comparing the evidences generated from the Bayesian fitting, we find that the double Sérsic models are preferred by more than 10-σ over the other models in all cases. The de Vaucouleur model gives the highest estimate of the total amount of light, followed by the single Sérsic, the double Sérsic and the exponential model respectively. Calculating the magnitudes in the "hybrid" manner as described above gives very little difference in the total flux derived from different models.

Each model also yields different estimates of the residual background in the stacks. However, determining the background level independently and keeping it fixed during the fitting process does not alter our estimates of the extra light (at the 0.01 mag level). This is due to the fact that the results of the fitting are driven primarily by the inner high SNR part of the galaxy stack.

We conclude that the combination of the depth of our stacked image and our "hybrid" magnitudes enables us to accurately constrain the total flux in the galaxy stack. Our outer models are not truncated, but instead extend out to infinity. The difference between models which are truncated at $7\,R_e$ and models which instead extend out to infinity is at most 0.05 mag.

4.3.4   Measuring the Flux Corrections

For each stellar mass, concentration range and model fit type (exponential or de Vaucouleurs), we measure the average extra flux correction to the `Model` magnitudes as the difference between the total integrated light in the stack and the median `Model` flux of the galaxies in the stack. The median `Model` magnitude was calculated by taking the median of the individual fluxes of galaxies in the stack. We find that the median `Model` magnitude is on average higher than the mean `Model` magnitudes. We use a two-dimensional-interpolation scheme to calculate the average extra light as a continuous function of stellar mass and concentration for each model type. These are shown in Figure 4.3. As can be seen, there is an extra light contribution from those galaxies which were fit by an exponential model both for high concentrations and for high stellar masses. The extra light correction from those galaxies fit by a de Vaucouleurs model comes predominately from the massive, high concentration galaxies. On the other hand, the de Vaucouleurs model often over-estimates the flux of a galaxy for low concentration massive galaxies.

We note that the large width of the stellar mass bins for the highest stellar mass galaxies may influence the correction derived in the stacking procedure. To account for
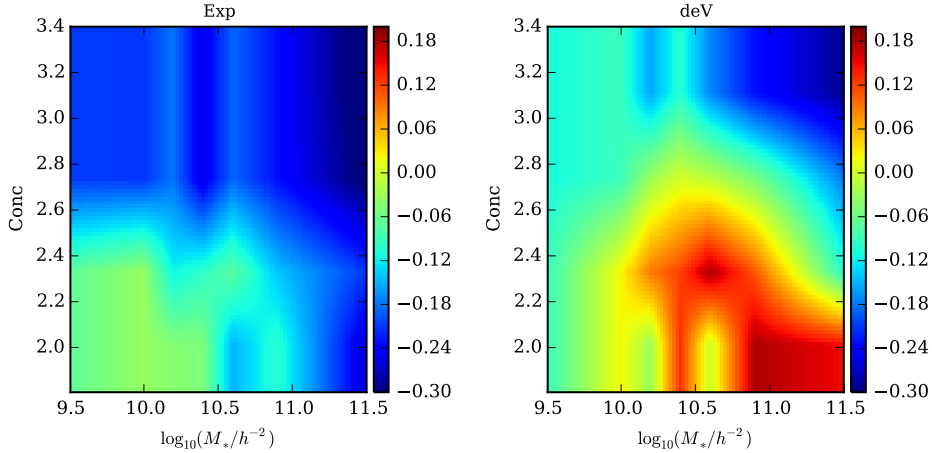
Figure 4.3: The flux corrections (ΔMag) as a function of stellar mass and concentration using an interpolation scheme for exponential (`Exp`) and de Vaucouleurs (`DeV`) fit galaxies.

this, we divide our highest mass sample, G4 ($11.09 < \log(M_*/M_\odot) < 11.69$, $2.9 < C < 3.3$, $0.14 < z < 0.18$), into smaller mass bins of size 0.1 dex. We find that the relative corrections ranges from 0.23 to 0.31 mag, gradually increasing from the lowest to the highest stellar mass bin (see Figure 4.4). The mean correction derived by stacking the entire sample G4 is 0.29 mag.

For galaxies outside the the mass limits defined in Section 4.2.2, we extrapolate assuming the same mass corrections of the nearest defined mass bin. In particular, at the high mass end, there are 116 galaxies with stellar masses larger than $\log(M_*/M_\odot) > 11.69$, the highest stellar mass bin used above. For these galaxies, we assume the corrections to be the same as found for the highest stellar mass bin (0.31 mag).

Assuming a constant M/L for each galaxy, we calculate the extra mass for each galaxy in our main sample given its stellar mass, concentration and model type (by comparing the likelihoods of the `Model` fits from the SDSS database) as:

$$\log \frac{M_* + \delta M_*}{M_*} = -\Delta\text{Mag}/2.5 \tag{4.2}$$

4.4   The Stellar Mass Function of Galaxies

4.4.1   Method

We estimate the abundance of galaxies as a function of their stellar mass using the $1/V_{max}$ method outlined by Li & White (2009). In combination with the depth and the large spectroscopic sample of SDSS, the $1/V_{max}$ method provides an unbiased estimate of the
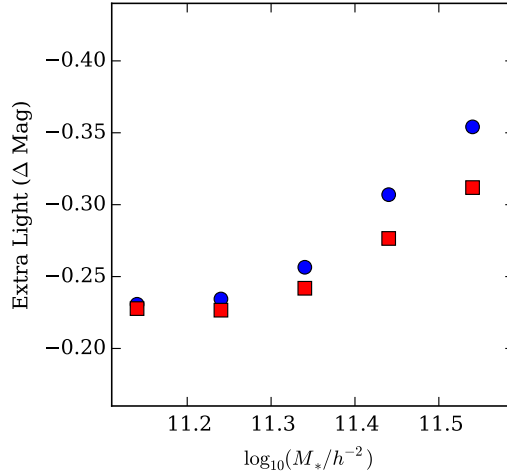
Figure 4.4: The flux corrections (ΔMag) as a function of stellar mass for galaxies in the sample G4 (blue circles). We also indicate the uncertainty in the corrections by showing the flux corrections derived from the mean `Model` flux of the stacks (red squares).

stellar mass function and its normalisation. In Section 4.4.2, we demonstrate that the $1/V_{max}$ estimator is unbiased against large scale structure at stellar masses of $\log(M_*/M_\odot) \geq 9.5$, which is the regime studied in this work. We limit ourselves to this regime since as estimated by Figure 4 of Baldry et al. (2008), all galaxies above stellar masses of $\log(M_*/M_\odot) \geq 9.5$, will be detected irrespective of their central surface brightness. Moreover, our flux corrections begin from $\log(M_*/M_\odot) \geq 9.6$ upwards.

For each observed galaxy i, we define the quantity $z_{max,i}$ to be the maximum redshift at which the observed galaxy would satisfy the apparent magnitude limit of our sample $m_{r_{Pet}} \leq 17.6$. Evolutionary and K-corrections are included when calculating $z_{max,i}$. Hence, $z_{max,i}$ is the minimum of the upper limit of the redshift slice and the solution of the equation:

$$M_i = m_{r_{Pet}}^{Faint} - DM(z_{max}) - K(z_{max}) + Q_e(z_{max} - z_i) \tag{4.3}$$

Similarly, we also define $z_{min,i}$ as the minimum redshift at which the galaxy would be present in our sample. Hence, $z_{min,i}$ is the maximum of the lower limit of the redshift slice and the solution to the equation:

$$M_i = m_{r_{Pet}}^{Bright} - DM(z_{min}) - K(z_{min}) + Q_e(z_{min} - z_i) \tag{4.4}$$

This then allows us to calculate $V_{max,i}$ for the galaxy in question as the total co-moving volume of the survey between $z_{min,i}$ and $z_{max,i}$. The stellar mass function can be then estimated as:

$$\Psi(M_*)\Delta M_* = \sum_i (f_{norm\,coll,i}\, V_{max,i})^{-1} \tag{4.5}$$

where $f_{norm\,coll,i}$ is the normalised fiber collision factor defined below, and the sum extends over all sample galaxies with stellar masses in the range $M_* \pm 0.5\,\delta M_*$. The error bars are estimated by taking into consideration both Poissonian and bootstrapping errors, as well as errors due to cosmic variance (See 4.4.2).

We calculate the stellar mass function in the total redshift range $0.001 \leq z \leq 0.5$ as well as in three redshift slices: $0.001 \leq z \leq 0.15$, $0.15 \leq z \leq 0.3$ and $0.3 \leq z \leq 0.5$.

4.4.2   Robustness of the $1/V_{max}$ Estimator

In this work, we estimate the abundance of galaxies using the $1/V_{max}$ method. Given the large effective surface area (nearly $6570\,deg^2$) and the depth of spectroscopic sample, the $1/V_{max}$ method will be invariant to large-scale structure up to a limiting stellar mass. To test this, we divide our sample into three independent but contiguous parts (Sample A, Sample B and Sample C split by right ascension), and calculate the standard deviation in the stellar mass function as a function of stellar mass. In the bottom panel of Figure 4.5, the standard deviation is plotted as a function of stellar mass. The difference in the estimates of the stellar mass function due to the $1/V_{max}$ method from the three independent samples is less than 10% for stellar masses $log(M_*/M_\odot) > 9.5$. The standard deviation gives us also a handle on the errors in our estimates of the stellar mass function due to the cosmic variance.

4.4.3   The Effect of Systematic and Random Errors on the SMF

In calculating the stellar mass function, various systematic and random effects combine to affect the final result. We discuss each of these effects in turn in the following subsections:

MPA-JHU Stellar Masses and Extra light from Photometry

The first source of systematic bias comes from the estimation of the stellar mass of individual galaxies. In this work, we use the MPA-JHU stellar masses to calculate the stellar mass function. This involves a change of flux (from `Petrosian` to `Model` magnitudes) and M/L ratio (from NYU-VAGC to MPA-JHU) relative to Li & White (2009).

We find that the use of NYU-VAGC stellar masses based on the `Model` magnitudes rather than the `Petrosian` magnitudes introduces a shift beyond the knee of the stellar mass function towards a shallower slope at the higher mass end. This shift is then further increased when we switch to MPA-JHU stellar masses based on the `Model` magnitudes. The slope of the massive end of the mass function is shallower than that obtained by shifting the mass function derived from the NYU-VAGC stellar masses by 0.1 dex (See appendix of Li & White 2009: $\Delta \log M_* = 0.1$). At a stellar mass of $\log M_* \sim 11.5\,M_\odot$, this accounts for an increase in the stellar mass function by a total of 1.24 dex (a 0.57 dex increase due to the change from `Petrosian` to `Model` magnitudes and a 0.67 dex increase due to the change from the NYU-VAGC to MPA-JHU M/L ratios).
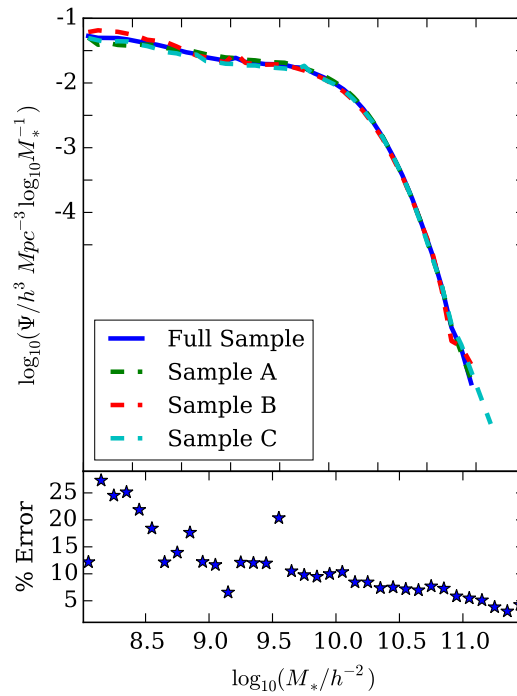
Figure 4.5: Top panel: The stellar mass function for the complete sample as well as the three independent smaller samples A, B and C, using the MPA-JHU stellar masses for the full redshift range $0.001 \leq z \leq 0.5$. Bottom Panel: The standard deviation in the stellar mass function as a function of stellar mass.

Our assumed M/L ratio affects our estimation of the stellar mass function. The use of the MPA-JHU stellar M/L ratios makes the slope at the massive end shallower than the NYU-VAGC M/L ratios. We note that the MPA-JHU M/L ratios are derived from models that include the possibility of complex star formation histories, whereas the NYU-VAGC assumes that red galaxies can be described by single stellar populations. Analysis of spectra of massive galaxies in the BOSS survey by Chen et al. (2013) indicates that the star formation histories of the most massive galaxies are characterised by episodic star formation histories.

The extra flux derived from the photometry of stacked galaxies introduces a further shift, making the slope at the massive end of the stellar mass function even shallower. We find that this shift of the stellar mass function is independent of whether we apply the corrections only to the central galaxies, or to all the galaxies in the sample. Although a small difference is found at the knee of the mass function, both results are consistent with each other within the error bars.

Fiber Collisions

The second source of systematic bias is caused by fiber collisions. The NYU-VAGC catalogue lists the spectroscopic completeness f_{sp} of each galaxy, defined as the fraction of photometrically defined target galaxies in the subarea for which usable spectra are obtained. The NYU-VAGC catalogue calculates the average completeness for each of these subareas by taking into consideration overlapping plates. In the jargon of the NYU-VAGC catalogue, these subareas are called *sectors*. f_{sp} contains information about the missing galaxies due to lack of fibers in dense regions, missing galaxies due to spectroscopic failures, and missing galaxies due to fiber collisions. The average f_{sp} for the sample defined above is 0.9146. However, f_{sp} assumes that all galaxies with measured spectra are randomly distributed within a sector, and hence cannot account for specific differences between high and low density regions in the same sector. In particular, due to fiber collisions, certain galaxies (e.g. satellite galaxies of large clusters found at high redshifts) will be preferentially missed.

To account for fiber collisions, we define the fiber collision $f_{coll,i}$ for each galaxy, as the fraction of photometrically defined target galaxies that fall within a area of 55" in radius. $f_{coll,i}$ takes the values between 0.111 and 1.0 (that is, 8 closest neighbours and no neighbours respectively). The average of $f_{coll,i}$ over our whole sample is 0.93819. We normalise $f_{coll,i}$ such that it's average value is the same as that of f_{sp}. $f_{norm\,coll,i} = fac * f_{coll,i}$, where fac is defined as $< f_{sp} > / < f_{coll} >$ and takes the value 0.9749. The normalised fiber collision $f_{norm\,coll}$ now has the general average properties of f_{sp}, but can better account for fiber collisions.

Weighting by normalised fiber collision maintains the normalisation of the stellar mass function at the low mass end and increases the mass function up to 22% at the high mass end. Li & White (2009) did not include fiber collisions in their derivation and we can only reproduce their stellar mass function by using `Petrosian` magnitudes and by neglecting the effect of f_{sp}.

Evolution Corrections

The third main source of systematic error is related to the assumption about the passive evolution of galaxies both in their number density and luminosity. In order to construct a stellar mass function from a large redshift range ($(0.001 \leq z \leq 0.5)$, we would need account for the passive evolution of galaxies using a so-called evolutionary correction. Assuming such a uniform evolutionary correction is problematic, since galaxy evolution is a function of galaxy type and cannot be described by a simple linear model. For example, star-forming galaxies will evolve more slowly in luminosity than early-type galaxies.

In order to quantify the effects on the stellar mass function related to the assumptions about galaxy evolution, we consider two approaches. In the first approach, we assume a uniform evolutionary correction ($Q_r = 1.62$), which would represent an upper limit for the evolution of early-type galaxies with high stellar masses and stellar populations that evolve passively with time (i.e. in the absence of any mergers). In the second approach, we derive the stellar mass function without evolution in three redshift slices: $0.001 \leq z \leq 0.15$, $0.15 \leq z \leq 0.3$ and $0.3 \leq z \leq 0.5$.

In Figure 4.6, we plot the stellar mass function derived using the MPA-JHU stellar masses, including a uniform evolutionary correction, accounting for fiber collisions and for the additional stellar mass corrections due to the extra light at large radii (red solid curve). In addition, we also indicate the mass function calculated in the three redshift slices mentioned above, without evolution. As seen from Figure 4.6, the evolutionary correction has only a small effect on the stellar mass function ($\sim 10\%$ at the massive end). This is related to the fact that the luminosity evolution is implicitly folded into the derivation of the M/L ratio.

Uncertainty due to binning the data

Another source of systematic bias is related to binning the data in calculating the mass function via the $1/V_{max}$ method. In particular, this introduces further uncertainty at the massive end of the mass function due to a combination of the low number statistics and the steep slope of the mass function over this mass range. In order to quantify this uncertainty, we recalculate the mass function with different values for the bin sizes, from 0.05 dex to 0.4 dex. In particular, larger bin sizes tends to bias the slope at the high mass end of the mass function towards shallower values. Reducing the bin size increases the steepness of the slope until a saturation limit of about 0.1 dex. The variation caused by changes in the bin size around the saturation limit is within the uncertainties derived by bootstrapping and within the Poissonian errors. Hence, we calculate the stellar mass function in bins of 0.1 dex.

Eddington Bias

Another source of systematic bias in the stellar mass function is caused by the random errors in the flux and M/L ratios of individual galaxies. Such an "Eddington" bias causes the stellar mass function to be higher in the low-number density part because of scattering
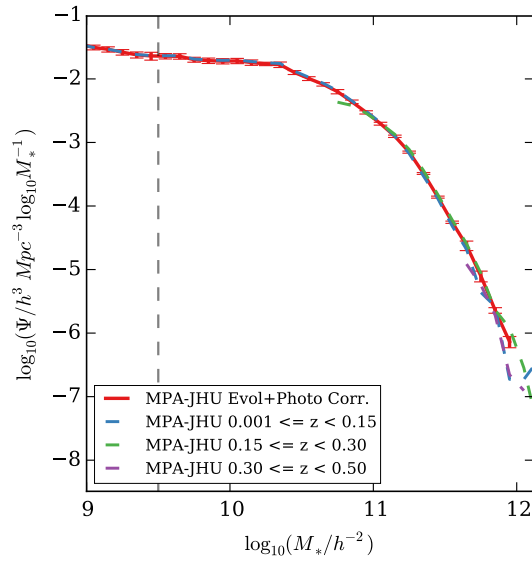
Figure 4.6:   The effect of evolutionary corrections on the stellar mass function: The red solid line shows the stellar mass function calculated using MPA-JHU stellar masses corrected for missing light from photometry of stacked galaxies, corrected for fiber collisions and with uniform evolutionary correction $Q = 1.62$ in the redshift range $0.001 \leq z \leq 0.5$. Also plotted are the stellar mass function without evolutionary corrections in redshift slices $0.001 \leq z \leq 0.15$, $0.15 \leq z \leq 0.3$ and $0.3 \leq z \leq 0.5$ dashed blue, green and violet lines.

from the lower stellar masses (higher number density). This becomes particularly acute because of the steepness of the stellar mass function at higher stellar masses.

To correct for this bias, we assume a parametrized form for the stellar mass function. We convolve this function with a distribution of the uncertainties in the stellar mass. We then fit this convolved function to the binned values of the stellar mass function calculated from the data using a maximum-likelihood method. The best fit paramteric function is thus our true stellar mass function corrected for the Eddington bias. For the parametric function, we assume a double Schechter function, given by

$$
\begin{aligned}
\Psi_M \mathrm{d}M \;=\; & \Big[\frac{\Psi_1^*}{M_1^*} \, e^{-M/M_1^*} \left(\frac{M}{M_1^*} \right)^{\alpha_1} + \\
& \frac{\Psi_2^*}{M_2^*} \, e^{-M/M_2^*} \left(\frac{M}{M_2^*} \right)^{\alpha_2} \Big] \mathrm{d}M \,,
\end{aligned}
\tag{4.6}
$$

where $\Psi_M \mathrm{d}M$ is the number density of galaxies between M and $M + \mathrm{d}M$. This provides a much better fit to the data relative to a single Schechter. We further assume that the uncertainties in the stellar mass are distributed normally in $\log_{10}(M_*/M_\odot)$.

To estimate the uncertainties in the stellar mass, we first estimate the M/L uncertainties as a function of stellar mass from the MPA-JHU database. We find that the average uncertainty $\Delta \log_{10}(M/L)$ ranges from 0.08 to 0.1 as a function of stellar mass. We then estimate the average uncertainty in the `Model` magnitude as a function of stellar mass. We find that the average uncertainty in the `Model` magnitude is $\sim 0.02 \, mag$ across the stellar mass range considered. Hence the M/L uncertainty is much larger than the flux uncertainty.

We find that correcting the stellar mass function for the Eddington bias reduces it at the high mass end by as much as 0.48 dex.

4.4.4 Results: Stellar Mass Function

In Figure 4.7, we present our final estimate of the stellar mass function corrected for missing flux, fiber collisions, evolution and Eddington bias with that of the original Li & White (2009) in red and the Bernardi et al. (2013) (Sersic-Exp fits) stellar mass function in green.

We provide a parametric representation of the stellar mass function for stellar masses greater than $\log(M_*/M_\odot) \geq 9.5$. The parameters of the double Schechter function are listed in Table 4.2. An integration of our stellar mass function for stellar masses greater than $\log(M_*/M_\odot) \geq 9.5$ gives the mean comoving stellar mass density of the low redshift universe as $\phi_* = 3.7 \pm 0.3 \, 10^8 \, h\mathrm{Mpc}^{-3}$. This amounts to a 35% increase in the mean comoving stellar mass density contributed from the same stellar mass range for the Li & White (2009) stellar mass function. In particular, focussing on the high stellar mass end: the mean comoving stellar mass density of galaxies with stellar masses $\log(M_*/M_\odot) \geq 11.0$ is a factor of 3.36 larger than the estimate by Li & White (2009), but is 43% smaller than reported by Bernardi et al. (2013).
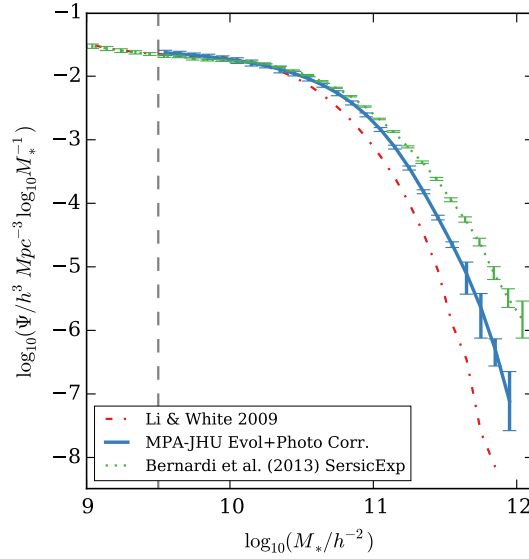
Figure 4.7:   The stellar mass function: The blue solid line shows the stellar mass function calculated using MPA-JHU stellar masses, corrected for missing flux, fiber collisions, evolution and Eddington bias. The red dot-dashed line shows the original Li & White 2009 stellar mass function calculated using the NYU-VAGC stellar masses based on `Petrosian` magnitudes. Also shown are the Bernardi et al. (2013) stellar mass function values (green) based on Sersic-Exp fits to individual galaxies. The dashed vertical line indicates our lowest stellar mass limit above which the stellar mass function is not affected by surface brightness completness issues.

Table 4.2: Parameters of a double Schechter function fit to the stellar mass function of SDSS galaxies.

Φ^* $(h^3\mathrm{Mpc}^{-3}\log_{10} M^{-1})$	α	$\log_{10} M^*$ $(h^{-2}M_\odot)$
0.008579	-1.082	10.615
0.000355	-1.120	10.995

Figure 4.8: The luminosity function: The $M_{0.1_r}$ luminosity function calculated with photometric corrections, fiber collisions and flux uncertainty in three redshift slices and assuming an uniform evolutionary correction of $Q_r = 1.62$. We also show the corresponding luminosity function from Bernardi et al. (2013) Sersic-exponential fits.

4.5 Galaxy Luminosity Function

Similar to the galaxy stellar mass function, we also calculate the galaxy luminosity function using the $1/V_{max}$ method. However, more careful attention needs to be paid to the evolutionary corrections which affects the luminosity function not only via the derivation of V_{max}, but also via the calculation of a galaxy luminosity via equation 4.1. We calculate the luminosity function using two approaches: in redshift slices ($0.001 \leq z \leq 0.15$, $0.15 \leq z \leq 0.3$ and $0.3 \leq z \leq 0.5$) without 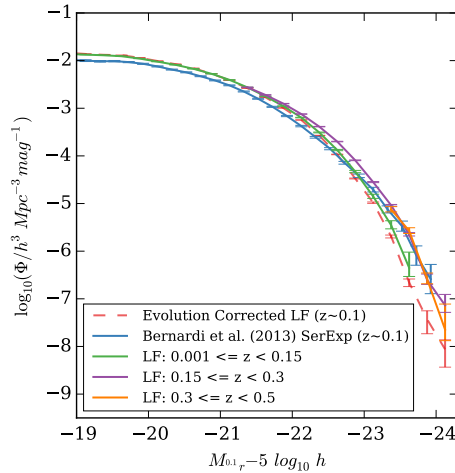evolution and using a uniform evolutionary correction of $Q_r = 1.62$. In Figure 4.8, we present the results of $M_{0.1_r}$ band luminosity function considering `Model` magnitudes with photometric corrections from stacking, fiber collisions and evolutionary corrections in bins of 0.25 dex. We also indicate the luminosity funtion without evolution corrections in three redshift slices. A comparision of our results with those of Bernardi et al. (2013) would require a more careful treatment of luminosity evolution which is beyond the scope of this paper.

4.6 Summary

In this paper, we have shown that stacking similar galaxies together in volume-limited stellar mass and concentration bins allows one to derive average flux corrections to the SDSS `Model` magnitudes. In particular, we find that these corrections range from 0.02 to 0.31 magnitude, depending on the stellar mass and concentration of the galaxy.

We apply these corrections to the `Model` fluxes and re-derive the stellar mass function using MPA-JHU stellar masses, accounting for galaxy evolution corrections and fiber col-

lisions. We find that the slope of the massive end of the stellar mass function is shallower than reported by Li & White (2009), but much steeper than derived by Bernardi et al. (2013).

The biggest change in the slope at the massive end of the mass function comes from our adoption of the MPA-JHU stellar masses (as much as a 1.24 dex increase at $\log M_* \sim$ 11.5 $M_\odot$ with respect to Li & White 2009). This involves an increase of 0.57 dex and 0.67 dex due to the changes in flux and M/L ratio respectively. The second major contributor is the bias caused by the uncertainty in M/L ratio and flux measurements of individual galaxies which accounts for a decrease of ~ 0.48 dex in the mass function at the massive end. Fiber collisions contributes to an increase of nearly 22% at the massive end. Galaxy evolution corrections accounts for a decrease of maximum 10% at the massive end of the mass function.

We also derive the r-band galaxy luminosity function and obtain similar results. In particular, the biggest source of systematic uncertainty in the galaxy luminosity function is related to the model assumed for the galaxy evolution correction. In this Paper, we use the evolution correction values derived by Blanton et al. (2003), which serves as an upper limit for galaxies at the bright end of the galaxy luminosity function.

4.7   Discussion

The flux corrections to the SDSS `Model` magnitude and their respective uncertainties derived in this work by stacking mosaics of similar galaxies in volume limited stellar mass and concentration bins are consistent with those presented by Simard et al. (2011). We find no evidence for the need of large flux corrections of the order of 0.5 magnitudes as proposed by Bernardi et al. (2013).

Our results are also consistent with extremely deep imaging of nearby early-type galaxies, obtained with the MegaCam camera on the Canada-France-Hawaii Telescope which indicate that outer LSB light contributes 5 to 16 percent to a galaxy's total luminosity (Duc et al., 2015). Stacking results for luminous red galaxies (average redshift of $z \sim 0.34$) from Tal & van Dokkum (2011) also indicate that typical SDSS-depth images miss about 20 percent of the total stellar light.

A number of systematic differences could contribute to the discrepancy between our results and those by Bernardi et al. (2013). In the limit of low SNR, the determination of the sky background level can influence the measured flux of a galaxy derived from fitting models to the surface brightness distribution. The depth of an image limits ones ability to distinguish between the flux of the outer LSB features of the galaxy and the sky background, especially for large stellar mass galaxies at higher redshifts. The use of multi-component models aggravates this problem.

The simultaneous estimation of the model parameters and the sky background level may be prone to systematic bias, since these are often degenerate with each other. Bernardi et al. (2013) use the `PyMorph` algorithm (based on `GALFIT`), which estimates the galaxy flux based on model fitting along with a simultaneous estimation of the sky background.

Meert et al. (2013) and Meert et al. (2015) have already highlighted the effect of a bias in the sky subtraction on the total flux of a galaxy. On the other hand, SDSS `Photo` pipeline estimates the `Model` magnitudes by first independently estimating and subtracting the local sky background. A similar procedure is followed by Simard et al. (2011). In this work, we use the background subtracted images provided with SDSS DR9 to derive the flux corrections. In addition, the depth of our stacked images allows us to accurately determine the residual sky background.

Estimating the total flux of a galaxy is dependent on the exact procedure used for deblending and masking (see Blanton et al. 2011 and Simard et al. 2011). In particular, the amount of masking employed has a substantial effect on the amount of flux that is derived for a specific galaxy. In this Paper, we use the conservative masking described in Chapter 3, which involves using multiple runs of `SExtractor` (Bertin & Arnouts, 1996).

Guo et al. (2010) calculated the stellar mass function using the NYU-VAGC stellar M/L ratios and `Model` magnitudes using the methodology of Li & White (2009). The stellar mass function derived here has a large shift and shallower slope than Guo et al. (2010), owing primarily to the use of the MPA-JHU stellar masses and the flux corrections to the `Model` magnitudes. The results of our work will affect the majority of recent halo occupation and abundance matching studies (e.g. Moster et al. 2013) that use the measurements of the stellar mass function from Guo et al. (2010).

Finally, we comment that the majority of studies of the evolution of the massive end of the stellar mass function have found suprisingly little change out to $z \sim 1$ (Maraston et al., 2013; Moustakas et al., 2013; Davidzon et al., 2013). The co-moving number density of galaxies with stellar masses greater than $10^{11} M_\odot$ has apparently remained constant over the past 9 Gyr, calling into question the late build-up of these systems through mergers and accretion. Our work has shown that a significant fraction of the mass of these systems may be "hiding" in low surface brightness outer components that are systematically missed by conventional photometric extraction software. Accurately quantifying the *evolution* of the stellar mass in these halos will be an important challenge for next generation deep imaging surveys.

Chapter 5

Conclusions and Outlook

In this thesis, we study the average properties of the stellar haloes of galaxies for a range of stellar masses in order to obtain important constraints on the physics of galaxy formation. We do so by stacking mosaics of a large number of face-on galaxies from the SDSS survey. This allows us to study the properties of the stellar halo out to a galactocentric distance of 70-100 kpc and down to a limiting magnitude of $\mu_r \sim 32 \, \mathrm{mag \, arcsec^{-2}}$. We parametrize the properties of the stellar halo and systematically study them as a function of stellar mass (from the MPA-JHU catalogue), halo mass (from the Yang et al. 2007 galaxy group catalogue and galaxy morphology. Further, we compare our observational constraints with the Illustris simulations. We summarize our main results below:

- The full two-dimensional surface intensity distribution of the galaxy stacks can only be fit through multi-component Sérsic models.

- Using stacks of mock images of galaxies from the Illustris simulations, we find that the outer light fraction derived from fitting double Sérsic models to the 2-D surface brightness distribution of galaxy stacks provides an upper limit (within 0.1 dex) of the mean accreted stellar mass fraction.

- We find that the outer light fraction is a function of stellar mass and galaxy type, increasing from 30% to 70% and from 2% to 25% for early and late type galaxies respectively over the mass range between $10^{10.0} M_\odot$ to $10^{11.4} M_\odot$.

- Above the characteristic mass ($\log M_{halo} \sim 12.5$), we find that the outer light fraction is a stronger function of halo mass than stellar mass.

- Below the characteristic mass, the outer light fraction is a strong function of a galaxy concentration (R_{90}/R_{50}). For galaxies with halo mass $\log M_{halo} \sim 12.0$, the outer light fraction ranges from 15% to 60% with increasing concentration.

- The outer slope of the surface brightness profile is an increasing function of halo mass. Above $\log M_{halo} > 13.7$, there is no relationship between the outer slope and halo mass. For galaxies $\log M_{halo} < 13.7$, the outer slope is a stronger function of

halo mass than stellar mass. However below the characteristic mass, the outer slope is a stronger function of the concentration of the galaxy than halo/stellar mass.

- The outer ellipticity profiles of the galaxy stacks is a stronger function of stellar mass than halo mass. The outer ellipticity is also a strong function of concentration of the galaxy. This implies that galaxies with higher concentrations and higher halo mass have elliptical stellar haloes aligned with the inner light distribution of the galaxy.

- The colour profile of high concentration galaxies reveals that the g-r colour of the stellar population in the stellar halo is bluer than in the main galaxy, and the colour of the stellar halo is redder for higher mass galaxies.

- We find that our observational constraints agree well with the Illustris simulations above the characteristic mass. However, the simulations fail to reproduce the data below the characteristic mass where the accreted mass fraction is an increasing function of stellar mass.

- SDSS `Model` magnitudes systematically understimate the contribution of the flux from the outer low surface brightness part of the galaxies. We find correction ranging from 0.05 to 0.32 mag for the highest stellar mass galaxies.

- We find that the flux corrections and the use of the MPA-JHU stellar masses have a significant impact on the massive end of the stellar mass function at $z = 0.1$, making the slope significantly shallower than that estimated by Li & White (2009), but steeper than derived by Bernardi et al. (2013). This corresponds to a mean comoving stellar mass density of galaxies with stellar masses $\log(M_*/M_\odot) \geq 11.0$ that is a factor of 3.36 larger than the estimate by Li & White (2009), but is 43% smaller than reported by Bernardi et al. (2013).

Above all, this thesis demonstrates the fact that not only is it possible to obtain observational constraints of the average properties of stellar haloes of galaxies over a range of stellar masses, but also that they can help us test and improve our models of galaxy formation.

In the spirit of this work, the next generation of large all-sky imaging surveys like DES and LSST would allow a systematically study the stellar haloes of galaxies as a function of stellar mass, galaxy type and environment. Additionally, their increased depth would allow us to probe the colour profiles of the stellar populations out to larger radii than what was previously possible with SDSS.

On the other hand, obtaining deep imaging of the stellar haloes of galaxies could help constrain the accreted stellar mass fraction of individual galaxies. The MATLAS (Mass Assembly of early-Type GaLAxies with their fine Structures) and the ATLAS3D surveys will soon provide deep imaging of nearby early-type galaxies (within 42 Mpc) and would allow us to study the distribution of stars in the outer most regions of the galaxy along with their fine structure (tidal tails, stellar stream, and shells) around them.

Perhaps, the greatest progress in recent years will come from metallicity and abundance constraints of stellar populations in the outer LSB regions of galaxies from integral field spectroscopic (IFS) surveys like MaNGA (Mapping Nearby Galaxies at APO) and SAMI (Sydney-AAO Multi- object Integral field spectrograph). Not only will large IFS surveys revolutionize the study of galaxy formation by offering a 3D perspective of galaxies, but they in combination with new stellar population synthesis (SPS) models (e.g. Conroy & van Dokkum, 2012) could also provide important constraints on their outer stellar populations. These observational constriants will inform our next generation of models of the stellar haloes of galaxies.

Appendix A

Low Surface Brightness

A.1 The Amount of Light Missed

The masking procedure we have employed is far from perfect. Contamination may arise from the incomplete masking of unresolved sources. An estimate of the amount of light missed as a function of environment can be made by creating mock galaxy images from an appropriate Schechter luminosity function for that environment. For the purpose of estimating how much of unresolved sources is not masked out in our field environment, we generate 1000 realistic mock galaxy r-band images resembling the field environment of our Sample by using a fixed single Sérsic model for the main central galaxy and the parameters of the r-band Schechter luminosity function of Blanton et al. (2003) for the galaxy environment. Each galaxy image was convolved with the SDSS r-band PSF. In addition, Poisson noise was added to each image.

    After subjecting these mocked images to our masking/stacking procedure outlined in the paper, we try to recover the surface brightness profile of the central galaxy. We find that we recover surprisingly well the surface brightness profile over a large range of the galaxy as seen in A.1. PSF effects come into play at the centre of the galaxy, while the profile in the faint outer parts depends on the accuracy of the background subtraction.

    Our recovery of surface brightness profile can be attributed to a number of factors: First of all, the relatively low density environment of field galaxies help in the masking procedure. Secondly, multiple runs of SExtractor help us to mask out most of the overlapping galaxies. Thirdly, the percentile cuts we have used in the stacking procedure helps us to deal with failures in the masking procedure especially close to the main galaxy.

A.2 Measurement of the Outer Slope

To measure the outer slope ($\mathbf{m}$) of the surface brightness profile, we consider a hierarchical Bayesian methodology that takes into consideration measurement errors and the intrinsic scatter in the slope σ (Kelly, 2007). Following Equation 2.2, we can write the likelihood
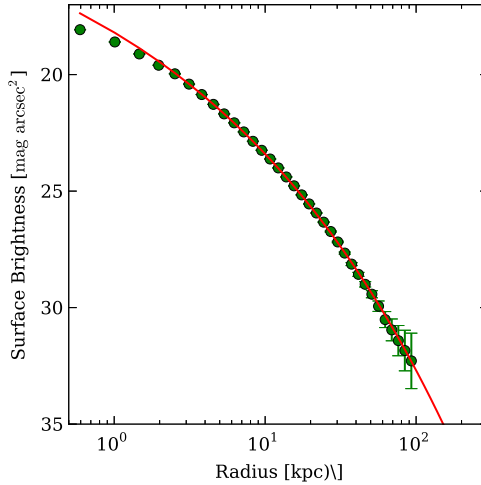
Figure A.1: Recovered Luminosity Profiles from the mock images. The red line is the initial model convolved with the r-band PSF.

for each measurement y_i with measurement error δy_i as:

$$p(y_i \mid \theta) = \frac{1}{\sqrt{2\pi(\delta y_i^2 + \sigma^2)}} \exp\left\{-\frac{1}{2}\frac{[y_i - E(y_i \mid \theta)]^2}{\delta y_i^2 + \sigma^2}\right\}, \qquad (A.1)$$

where $E(y_i \mid \theta) = 10^{m\log x_i + c}$.

Following Kelly (2007), we use uniform priors in m ($-10 : 10$), c ($-100 : 100$) and σ^2 ($10^{-8} : 1$). We calculate the posterior PDF of each parameter using MULTINEST. For the final parameters, we report the maximum of the posterior PDF. The uncertainty in the reported parameter is calculated from the variance of the posterior PDF.

A.3   The Influence of the PSF on the Colour Profiles

The g-r colour profiles in Figures 2.6 and 2.7 have been derived without convolving for the PSF. We have justified this on the basis of the small difference between the PSF in the g and r band as shown in Figure 2.5. In order to investigate the effect of the PSF on the colour profiles, we also derive the colour profile through a parametric method from the model fits as done by La Barbera et al. (2012) for early-type galaxies. We first fit models to both the g and r bands (as demonstrated in Section 2.5). In Figure A.2, we derive the g-r colour profiles directly from the models fits to the g and r band image stacks. These parametric colour profiles are devoid of the effects of the PSF. They display the same trends as the non-parametric colour profiles as derived in Section 2.4.3. There are small differences (within the error bars) in the colour profiles close to the center of the galaxy stack. These differences increase for higher stellar mass bin stacks. This is due to the fact that the models in Section 2.5 provide a poor fit at the center of the galaxy stacks because

of the high variance and the asymmetries present. This demonstrates that the g-r colour profiles derived in Section 2.4.3 are robust. This is also consistent with the conclusions of La Barbera et al. (2012) that the PSF does not affect the g-r colour profile a lot (Figure. 3 of La Barbera et al. 2012).
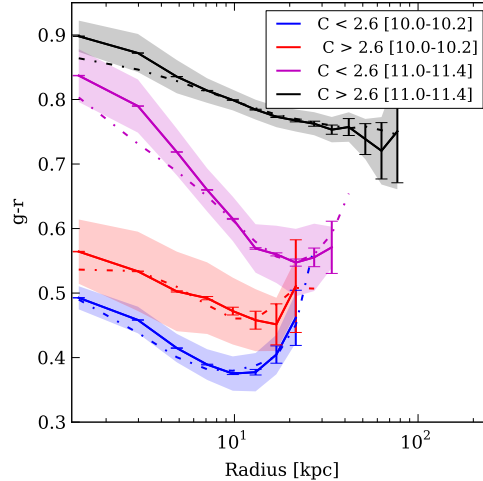

Figure A.2: The g-r colour profiles derived directly (solid lines) and through the parametric method (dot-dashed lines) for high and low concentration galaxies in the stellar mass bin range $10^{10.0} M_\odot < M_* < 10^{10.2} M_\odot$ and $10^{11.0} M_\odot < M_* < 10^{11.4} M_\odot$.

A.4   The Effect of Masking on the Stellar Halo

The effective masking of secondary sources (neighbouring and interlopping galaxies as well as field stars) in large mosaics created for the purpose of stacking is essential to distinguish LSB stellar halo light of the main galaxy from the light (both direct and scattered) of the secondary sources. This becomes particularly important for galaxies found in groups and cluster environment, small undetected neighbouring satellite galaxies can contribute significantly to the overall surface brightness distribution of the main galaxy.

In this work, we pay particular attention to mask out secondary sources and their scattered light. We detect secondary sources in the mosaic by employing `SExtractor` (Bertin & Arnouts, 1996) to detect all sources above a limiting surface brightness limit. We use a minimum detection area of 5 pixels, a Gaussian filter of 7 x 7 pixels (FWHM=4.0 pixels) for detection and a detection threshold of $1.5\,\sigma$ above the local background. The most significant parameter in `SExtractor` which affects the detection of sources in crowded fields at the centers of groups and clusters is the deblending contrast parameter (`DEBLEND_MINCONT`). At its minimum level of 0, even the faintest local peak in the surface brightness distribution is deblended as a separate object. At a maximum value of 1, no deblending will be authorised. The number of deblending thresholds was set to the optimal number of 32.

In order to mask out the scattered light of the detected secondary sources, we convolve our 'master' image (created by stacking the g, r and i-band mosaics) with a top hat kernel before deriving a segmentation map using `SExtractor`. The size of the top hat convolution kernel sets the radius around the detected sources which gets masked.

We optimize the value for the deblending contrast parameter and the size of the top-hat kernel by testing our masking procedure in an extreme environment: high redshift galaxies at the centers of clusters. For this, we consider a sub-sample of the `MaxBCG` catalogue (Koester et al., 2007) of 293 galaxies in the redshift range $0.2 \leq z \leq 0.3$ for which there are spectroscopic redshifts and which have N_{gal}^{R200} ¿ 26, where N_{gal}^{R200} given by the number of E/S0 ridgeline members brighter than $0.4\,L^*$. The galaxy images were aligned along the major axis, corrected for galactic extinction and transformed to redshift $z = 0.3$. Transformed mosaics whose average and cumulative intensity deviated more than $3\,\sigma$ from the median values were rejected. This leaves us with a sample of 282 galaxies. The images of the galaxies were stacked using the clipped-mean algorithm.

In Figure A.3, we explore the surface brightness distribution of the final stack of galaxies as a function of the deblending contrast parameter and the size of the top hat convolution kernel. In the left panel of Figure A.3, we explore various values of the deblending contrast parameter on the surface brightness profile of the stack used above using a fixed tophat kernel of size 12 pixels. The value of the contrast parameter makes a small difference in the surface brightness profile between 50 and 130 kpc for galaxies at redshift $z \sim 0.3$. In the right panel of Figure A.3, we explore the effect of using various size of the kernel for a fixed contrast parameter of 0.001: 0×0 (no kernel), 3×3, 6×6, 12×12 and 15×15 pixels. Deviations of the surface brightness profile occur at $\mu_r \sim 26 - 27\,\mathrm{mag\,arcsec}^{-2}$, the detection limit of SDSS. Sources detected at $\mu_r \sim 25 - 26\,\mathrm{mag\,arcsec}^{-2}$ contribute their scattered light around $\mu_r \sim 29\,\mathrm{mag\,arcsec}^{-2}$. Convergence is reached using a kernel of 12×12 pixels.

We conclude that the parameter that makes the most contribution to the masking of scattered light is the size of the top hat convolution kernel used to create the segmentation masks. It affects the surface brigthness profiles larger than 60 kpc, and has a maximum effect at distances greater than 100 kpc where it decreases the surface brightness distribution by as much as $1\,\mathrm{mag\,arcsec}^{-2}$. The second parameter which makes a much smaller contribution between 50 and 100 kpc is the deblending contrast parameter, and can cause a maximum decrease of $0.3\,\mathrm{mag\,arcsec}^{-2}$ in this radial range.

The effect of scattered light is more pronounced at higher redshifts because of the large radial extent of the PSF. In order to compare how our masking procedure fares with redshift, in the left panel of Figure A.4 we compare the above `MaxBCG` sample with two sub-samples of comparable richness at lower redshits from the Yang et al. (2007) group catalogue used in this work: massive central galaxies $(14.0 < \log(M_{halo}/M_\odot) < 15.5)$ in the redshift range $0.06 \leq z \leq 0.1$ and $0.1 \leq z \leq 0.2$. To take into consdieration the redshift dependance of the PSF broadening, we convolve the lower redshift stacks with the effective PSF transformed to $z \sim 0.3$. Although the surface brightness profiles of the three samples $< 100kpc$ are relatively the same, there are slight differences between the three samples beyond 100 kpc: The high redshift `MaxBCG` sample deviates around
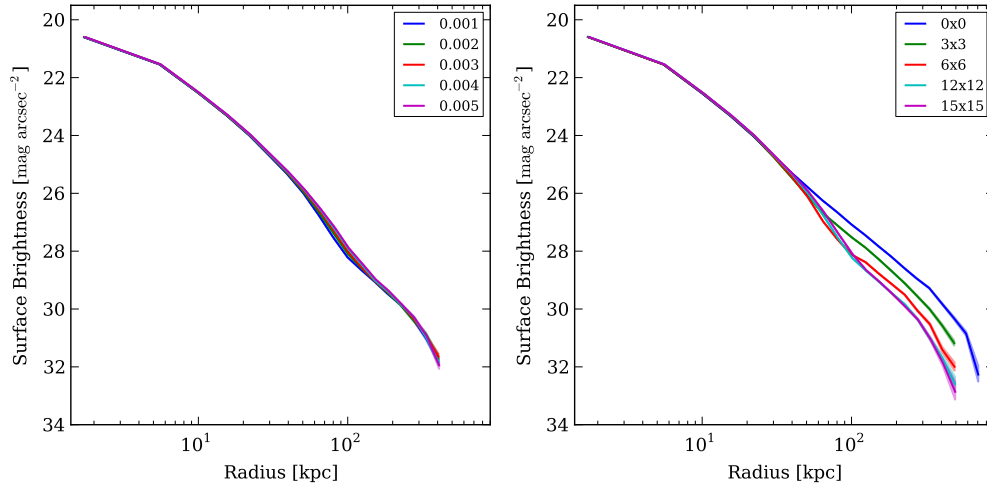
Figure A.3: *Left*: The surface brightness profile at $z \sim 0.3$ for various values of the contrast parameter used in the masking procedure along with a tophat kernel of size 12×12 pixels. *Right*: The surface brightness profile at $z \sim 0.3$ for various convolution kernels employed in the masking procedure along with a deblending contrast parameter of 0.001. The error bars in both panels indicate are the uncertainty due to background subtraction only.

($\mu_r \sim 29 \, \mathrm{mag \, arcsec^{-2}}$) from the other two. This difference could be attributed either to the difference in the effectiveness of the masking procedure or the intrinsic differences in the samples themselves. The masking parameters chosen above for redshift $z \sim 0.3$ are a conservative limit and are effective also at lower redshifts.

Failure to consider the scattered light can affect the estimation of the stellar halo and ICL of galaxies. Zibetti et al. (2005) explored the surface brightness profiles in the g,r and i bands of the ICL of galaxies from the the `MaxBCG` catalogue (Koester et al., 2007) using 693 clusters between $0.2 < z < 0.3$ selected from SDSS-DR1. These galaxies were selected such that $N_{gal} \geq 15$ and $N_{gal,3} \geq 5$, where N_{gal} is the number of red-sequence galaxies within $1 h^{-1} Mpc$ and $N_{gal,3}$ is the number within $0.33 h^{-1} Mpc$. We reprocess the galaxies chosen from the sample of Zibetti et al. (2005) using our masking algorithm transforming all the galaxies to $z = 0.3$. In right panel of Figure A.4, we compare our masked (median and clipped-mean) stacks with those of Zibetti et al. (2005). Beyond 50 kpc ($\mu_r \sim 26.5 \, \mathrm{mag \, arcsec^{-2}}$,), appreciable differences appear in the surface brightness profile.

A.5 Estimating Outer Light Fractions at various Redshifts

In this work, we estimate the outer light fraction from SDSS stacks transformed to the fiducial redshifts $z = 0.1$ and $z = 0.2$ for galaxies below and above $\log M_{halo} \sim 12.5$
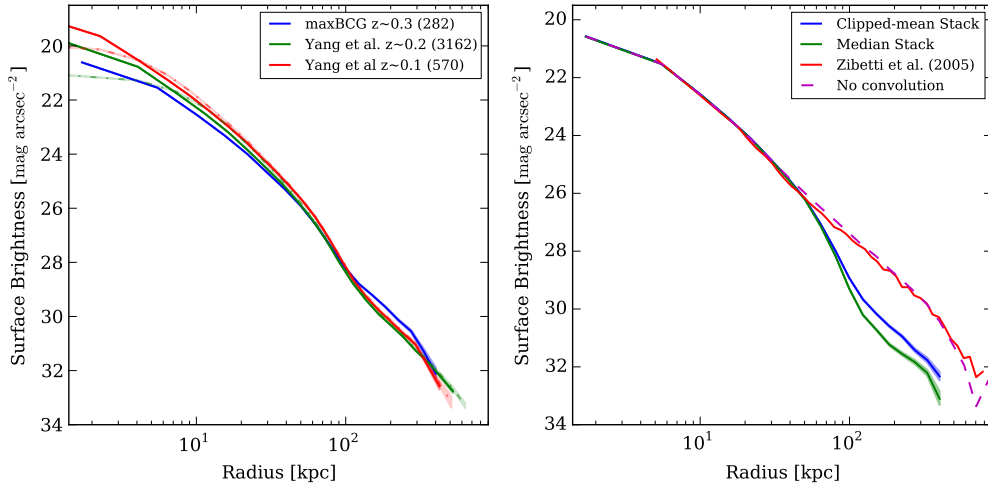
Figure A.4: a) The r-band surface brightness profiles of three samples at representative redshifts 0.1, 0.2 and 0.3. The number of galaxies in each stack is also indicated. The lighter dot-dashed lines are the surface brightness profiles of the lower redshift sample convolved with an effective PSF at $z \sim 0.3$. b) The surface brightness profiles of masked galaxies chosen from the sample of Zibetti et al. (rich BCGs in the redshift range $0.2 \leq z \leq 0.3$) with results from the corrected Zibetti et al. 2005 profiles in the r-band.

respectively. At these redshifts, the physical scales are $1\,\mathrm{pix} = 0.709\,\mathrm{kpc}$ and $1\,\mathrm{pix} = 1.26\,\mathrm{kpc}$ respectively. Moroever, stacks contain galaxies over a range of redshifts ($0.05 \leq z \leq 0.1$ and $0.05 \leq z \leq 0.2$). The effective seeing of the final stack is much smaller than the median seeing at the fiducial redshifts of the stacks. For stacks at the fiducial redshift $z = 0.1$, we can often resolve central structures of effective size ~ 1 kpc. This may bias our estimates of the outer light fraction for stacks transformed to the fiducial redshift $z = 0.1$. We recall that in fitting a double Sérsic model to the 2D surface brightness distribution, we use an effective PSF which takes into account the transformation of each galaxy in the stack to the fiducial redshift.

In order to make sure that the double Sérsic model fitting procedure resolves the insitu and accreted components instead of the inner resolved component for stacks transformed to the fiducial redshift $z = 0.1$, we ignore the central region in the fitting procedure by increasing the variance of the pixels in the central region within a radius of 2 pixels. We add the extra central residual flux to the insitu component. We illustrate this in Figure A.5 which shows the results of the fitting procedure for a galaxy stack ($11.8 \leq \log(M_{halo}) \leq 12.1$ & $10.0 \leq \log(M_*) \leq 10.46$) used later in the work. The estimated outer light fraction is 24%. Failing to ignore the central inner region (shaded cyan) results in resolving the central inner component (whose effective radius is shown by the horizontal dotted line) and an outer light fraction of 80%.

For stacks above $\log M_{halo} \sim 12.5$ transformed to fiducial redshift $z = 0.2$, the estimated outer light fraction is sensitive to the central pixels and the effective PSF of the final stack.
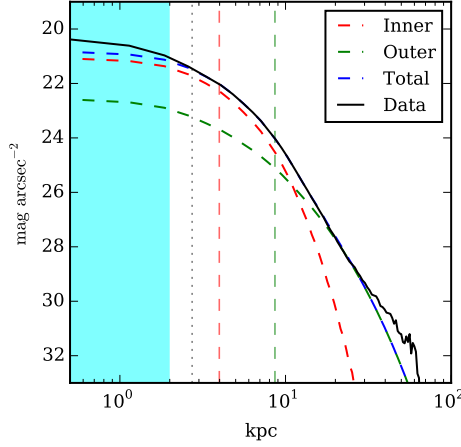
Figure A.5: The surface brightness profile of a galaxy stack ($11.8 \leq \log(M_{halo}) \leq 12.1$ & $10.0 \leq \log(M_*) \leq 10.46$) is shown in the solid black line. The red and green dashed lines show the inner and outer Sérsic component profiles. The blue dashed line shows the sum of the two components. The dashed red and green horizontal lines show the effective radii of the inner and outer components respectively. The cyan shaded region indicates the central region which we ignore in the fit by increasing the variance of the image. The dotted horizontal line shows the effective radius of the central structure if it was not ignored in the fitting procedure.

Hence, we do not down-weight the central pixels. We also note that the FWHM of the effective PSF is about $1\,\mathrm{pix} = 1.26\,\mathrm{kpc}$ and is smaller than the effective radius of the inner Sérsic component.

We find that the estimates of the outer light fraction from the two above methods are consistent with each other.

Appendix B

Comparison with Theoretical Models

Note: This chapter is part of a paper published in Monthly Notices of the Royal Astronomical Society *(Cooper et al., 2013).*

B.1 Comparison of Cooper et al. profiles with stacked SDSS data

In this Section, we compare the average galaxy surface density profiles from the models of Cooper et al. (2013) with our own profiles from our average SDSS stacks in bins of stellar mass (as given by the MPA-JHU Value-Added Catalogue[1]). These models have a free parameter f_{mb} which controls the fraction of the most bound particles tagged in the simulations. This parameter was chosen to reproduce the stellar mass half-mass radius relationship (See Fig 3 of Cooper et al. 2013). We compare our stacked profiles to models with $f_{\mathrm{mb}} = 1\%$, $f_{\mathrm{mb}} = 5\%$ and $f_{\mathrm{mb}} = 10\%$.

The resulting density profiles are shown as open circles in Fig. B.1, split into four bins of stellar mass, each of which is obtained from a stack of N_{DR9} galaxies as indicated. The panel labelled 'SDSS data only' summarises these four profiles, showing a clear shift in amplitude from the least to the most massive bin, out to the largest measured radius. Each panel assumes a constant r band mass-to-light ratio (the average of the MPA-JHU M/L_r values in the corresponding MPA-JHU mass bin, ranging from 2.3 to 2.8 from the first to last bin) but this result holds even if the same M/L_r is used for all panels, or if a colour-dependent M/L_r relation is used (Bell et al. 2003).

Each panel compares our SDSS stacks to the average profiles of simulated galaxies[2] binned by their Petrosian stellar mass, M_{pet} (blue, green and red lines for $f_{\mathrm{mb}} = 1\%, 5\%$ and 10%, respectively). We use M_{pet} rather than the true stellar mass $M_\star$ in order to reproduce

---

[1] http://www.mpa-garching.mpg.de/SDSS/DR7

[2] The observed and simulated profiles in Fig. B.1 should only be compared at $R \sim 5$ kpc. At smaller radii, the point spread function, which we have not deconvolved, dominates the observed profiles and numerical softening affects the simulated profiles.

approximately the bias introduced by SDSS `modelMag` magnitudes, from which the MPA-JHU masses are derived. It is important to note that M_{pet} is always an underestimate of $M_\star$.

Even though the trends in the simulated data are quite weak, for $f_{mb} = 1\%$ they are still clearly stronger than observed. For $f_{mb} = 5\%$, on the other hand, the agreement with observation is quite good, and a slightly smaller value of f_{mb} would agree even better.

This indicates that the Cooper et al. (2013) models provide a relatively good description of the average stellar mass surface density profiles of the stellar haloes of galaxies when binned in stellar mass.
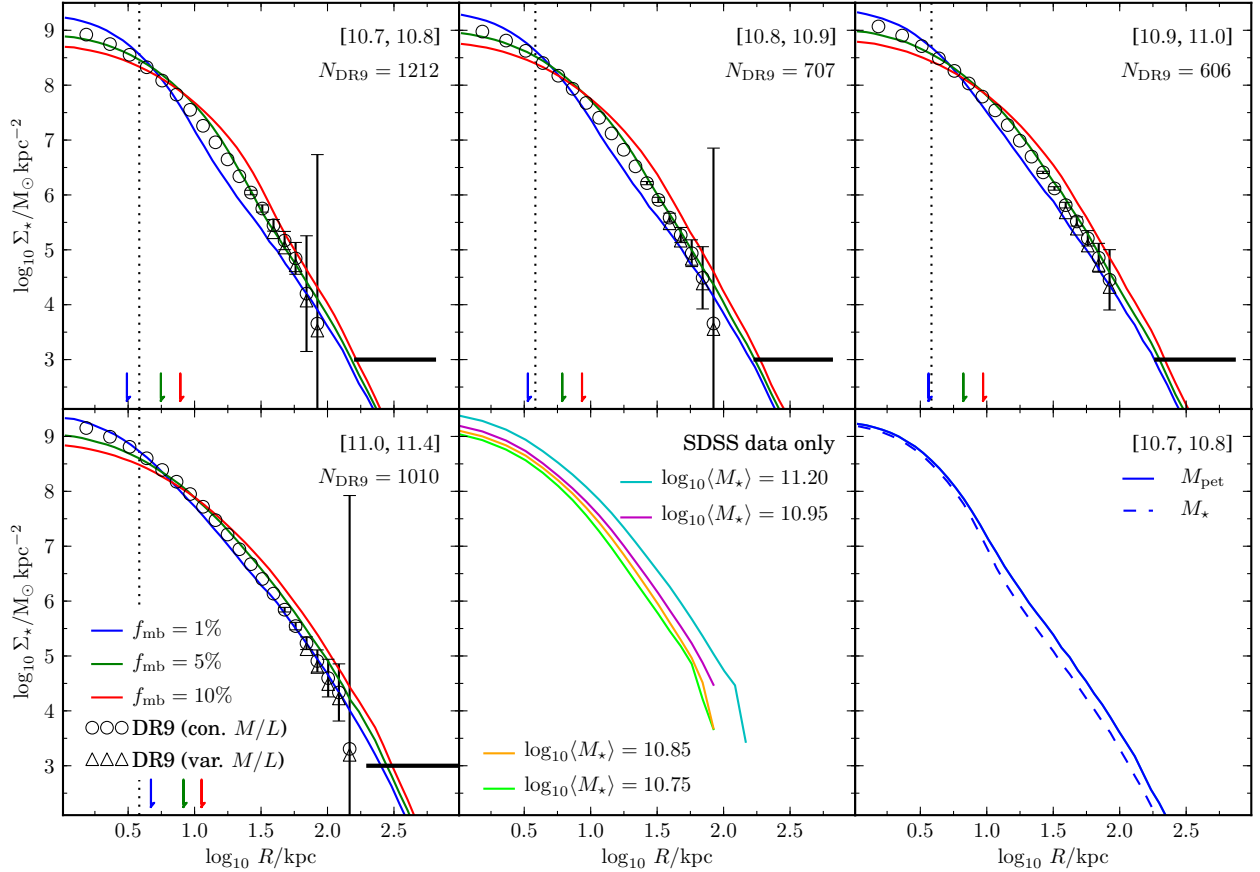
Figure B.1: **Comparison of models of Cooper et al. with SDSS stacks**: Symbols show the average stellar mass surface density profiles obtained from stacks of SDSS DR9 r band images, assuming a constant stellar mass to light ratio (open circles) and, where significantly different, a colour-dependent M/L (open triangles). Error bars approximate '1σ' of the distribution of uncertainty in the average profiles combining Poisson errors in flux measurement with the sample variance of the stack (N_{DR9} given in each panel shows the number of galaxies in the bin). Coloured lines (blue, green and red) show stacks made from Cooper et al. but here binning galaxies by their Petrosian mass $M_{\rm pet}$ (see text). The lower central panel shows the four SDSS profiles only (colours indicate the central mass of each bin). The lower right panel reproduces the $f_{\rm mb} = 1\%$ profile from the $[10.7, 10.8]$ panel (solid line) and compares it to the average profile of galaxies stacked in the same range of total stellar mass $M_{\star}$ (dashed line) rather than $M_{\rm pet}$.

Bibliography

Abadi M., Navarro J., Steinmetz, M., 2006, MNRAS, 365, 747

Arnold R., Gilmore G., 1992, MNRAS, 257, 225

Amorisco N., Martinez-Delgado D., Schedler J., 2015, arXiv:1504.03697

Amorisco N., 2015, arXiv:1511.08806

Bakos J., Trujillo I., Pohlen M., 2008, ApJ, 638, 103

Bailin J., Bell E., Valluri M., Stinson G. et al. 2014, ApJ, 783, 95

Baldry I. K, Driver S. P, Loveday J. et al., 2012, MNRAS, 421, 1621

Baldry I. K., Glazebrook K., Driver S. P., 2008, MNRAS, 388, 945

Belokurov V., Zucker D., Evans W., Gilmore G. et al., 2006, ApJ, 642, 137

Bell E. F., McIntosh D. H., Katz N., & Weinberg M. D. 2003, ApJS, 149, 289

Bell E. F., Zucker D., Belokurov V. et al. 2008, ApJ, 680, 295

Bender R., Burstein D., Faber S. M., 1992, MNRAS, 399, 462

Bergvall N., Zackrisson E., & Caldwell, B. 2010, MNRAS, 405, 2697

Bernardi M., Hyde J. B., Sheth R. K., Miller C. J. et al. 2007, AJ, 133, 1741

Bernardi M., Meert A., Sheth R. K., Vikram et al. 2013, MNRAS, 436, 697

Bertin E., & Arnouts S. 1996, AAPS, 117, 393

Bertin E., Mellier Y., Radovich M., et al. 2002, ASPC, 281, 228

Bird S., Flynn C., Harris W., Valtonen M., 2015, A&A, 575, 72.

Blanton M. R., Hogg D. W., Bahcall N. A., et al. 2003, ApJ, 592, 819

Blanton M. R., Schlegel, D. J., Strauss, M. J., et al. 2005, ApJ, 129, 2562

Blanton M. R., Eisenstein D., Hogg D.W., Schlegel D.J., Brinkmann, J. 2005, ApJ, 629, 143

Blanton M. R., Roweis S. 2007, AJ, 133, 734

Blanton M. R., Kazin E., Muna D., Weaver B. A., & Price-Whelan, A. 2011, AJ, 142, 31

Bonaca A., Geha M., et al. 2014, ApJ, 795, 94

Boylan-Kolchin M., Springel V., White S.D.M. et al. 2009, MNRAS, 398, 1150

Brainerd T., 2005, ApJ, 628, 101

Bullock J. S., Kravtsov A., Weinberg D., 2001, ApJ, 548, 33

Bullock J. S., Johnston K. V., 2005, ApJ, 635, 931

Burke C., Hilton M., Collins C., 2015, MNRAS, 449, 2353

Cappellari M., Emsellem E., Krajnovic D., et al. 2011, 413, 813

Cappellari M., Romanowsky A., Brodie J., Forbes D. et al. 2015, 804, 21

Chen Y., Kauffmann G., Heckman T. M., Tremonti C., et al. 2013, MNRAS, 429, 2643

Cole S., Noberg P., et al. 2001, MNRAS, 326, 1, 255

Conroy C., Wechsler R., Kravtsov A., 2007, ApJ, 668, 826

Conroy C., van Dokkum P., 2012, ApJ, 747, 69

Cooper A. P., Cole S., Frenk C. S., White S. D. M., Helly J., Benson A. J., De Lucia G., Helmi A., et al., 2010, MNRAS, 406, 74

Cooper A., Martnez-Delgado, D., Helly J., Frenk C. et al. 2011, ApJ, 743, 21

Cooper A. P., D'Souza R., Kauffmann G., et al. 2013, MNRAS, 434, 3348

Cooper A. P., Parr O., Lowing B., Cole S., Fenk C., 2015, MNRAS, 545, 3185

Courteau S., Widrow L. M., McDonald M., et al. 2011, ApJ, 739, 20

Croton D. J., Springel V., White S. D. M., De Lucia G., et al. 2006, MNRAS, 365, 11

Daddi E., Renzini A., Pirzkal N., et al. 2005, ApJ, 626, 680

Dalcanton J., Spergel D., Gunn J., et al. 1997, MNRAS, 114, 635

Davidzon I., Bolzonella M., Coupon J., Ilbert O., Arnouts S., et al. 2013, A&A, 558, 23

Deason A., Belokurov V., Evans N., 2011, MNRAS, 416, 2903

Debattista V., van den Bosch F., Roskar R., et al. 2015, MNRAS, 452, 4094

de Jong R. S. 2008, MNRAS, 388, 1521

de Vaucouleurs G., 1948, Ann d' Astrophys., 11, 247

de Vaucouleurs G., 1959, Handbuch Phys., 53, 275

Doinidis Steve P., Beers T. C., 1989, ApJ, 340, 57

D'Souza R., Kauffmann G., Wang J., Vegetti S. 2014, MNRAS, 443, 1433

D'Souza R., Vegetti S., Kauffmann G., 2015, MNRAS, 454, 4027

Duc P., Cuillandre J., Karabal E., Cappellari M., 2015, MNRAS, 446, 120

Eggen O., Lynden-Bell D., Sandage A., 1962, ApJ, 136, 748

Feroz F., Hobson M. P., Bridges M. 2008, MNRAS, 398, 1601

Feroz F., Hobson M. P., Cameron E., & Pettitt A. N. 2013, arXiv:1306.2144

Fisher D., Drory N, Fabricius M., 2009, ApJ, 697, 630

Font A., Johnston K., Bullock J., Robertson B., 2006, ApJ, 646, 886

Font A., McCarthy I., Crain R., Theuns T. et al. 2011, MNRAS, 416, 2802

Fremman K. C., 1970, AJ, 160, 811

Frenk C., White S.D.M., 1991, MNRAS

Fritz A., et al., 2014, A&A, 563, A92

Gilbert K., Guhathakurta P., Beaton R., et al. 2012, ApJ, 760, 76

Gonzalez-Perez V., Castander F. J., Kauffmann G. 2011, MNRAS, 411, 1151

Greene J., Murphy J., Comerford J., Gebhardt K., Adams J. 2012, ApJ, 750, 32

Greene J., Murphy J., Graves G. et al. 2013, ApJ, 776, 64

Greene J., Janish R., Ma C., 2015, ApJ, 807, 11

Guo Q., White S., Li C., Boylan-Kolchin M., 2010, MNRAS, 404, 1111

Harris W., 1976, AJ, 81,12

Helmi A., White S. D. M., 1999, MNRAS, 307, 495

Helmi A., White S. D. M., de Zeeuw P, Zhao H., 1999, Nature, 402, 53

Helmi A., White S. D. M., 2001, MNRAS, 323, 529

Helmi A., Navarro J.; Meza A. et al. 2003, ApJ, 592, 25

Helmi A., White S.D.M., Springel V.. 2003, ApJ, 339, 834

Helmi A., 2004, ApJ, 610, 97

Hernquist L., Quinn P., 1988, ApJ, 331, 682

Hilz M., Naab T., Ostriker J., Thomas J. et al. 2012, MNRAS, 425, 3119

Hilz M., Naab T., Ostriker J., 2013, MNRAS, 429, 2924

Hirschmann M., Naab T., Ostriker J., Forbes D. et al., 2015, MNRAS, 449, 528

Huang S, Ho L. C., Peng C. Y., et al. 2013, ApJ, 766, 47

Hubble E. P., 1936, Realm of the Nebulae. Yale Univ. Press, New Haven, CT

Ibata R. A., Gilmore G., Irwin M.J., 1994, Nature, 370, 194

Ibata R. A., Gilmore G., Irwin M.J., 1995, MNRAS, 277, 781

Ibata R. A., Irwin M.J., Geraint F., Stolte A., 2001, ApJ, 547, 133

Ibata R. A., Lewis G. F, Martin N., et al. 2013, ApJ, 765, 15

Ibata R. A., Lewis G. F, McConnachie A. W., et al. 2014, ApJ, 780, 128

Ivezi Z., Goldston J., Finlator K., Knapp G. et al., 2000, AJ, 120, 963

Johnston K., Spergel D., Hernquist L., 1995, ApJ, 451, 598

Johnston K., Majewski S., Siegel M., et al., 1995, AJ, 118, 1719

Juric M., Ivezi Z., Brooks et al., 2008, ApJ, 673, 874

Kauffmann G., White S.D.M., Guiderdoni B., 1993, MNRA, 264, 201

Kauffmann G., Heckman T. M., White S. D. M., et al. 2003, MNRAS, 341, 33

Kauffmann G., Heckman T. M., White S. D. M., et al. 2003, MNRAS, 341, 54

Kauffmann G., White S. D. M., Heckman T. M., et al. 2004, MNRAS, 353, 713

Kauffmann G., 2015, MNRAS, 454, 1840

Kelly B. C., 2007, ApJ, 665, 1489

Kelvin L.S., Driver S.P., Robotham A.S.G., Hill D. T. et al. 2012, MNRAS, 421, 1007

Koester B., McKay T., Annis J., Wechsler R., et al. 2007, ApJ, 660, 1

Kinman T., Wirtanen C., Janes K., 1966, ApJS, 13, 379

Kinman T., Mahaffey C., Wirtanen C., 1966, AJ, 87, 314

Kormendy J. 1977, ApJ, 217, 406

Kormendy J., Kennicutt R. C. Jr. 2004, ARA&A, 42, 603

Kormendy J., Fisher D. B., Cornell M. E., Bender R. 2009, ApJS, 182, 216

La Barbera F., Ferreras I., de Carvalho R., et al. 2012, MNRAS, 426, 2300

Lackner C. N., & Gunn J. E. 2012, MNRAS, 421, 2277

Lackner C. N., Cen R., Ostriker J. P., Joung M. R. 2012, MNRAS, 425, 641

Law D., Johnston K., Majewski S., 2005, ApJ, 619, 807

Lee D., Johnston K., Sen B., Jessop W., 2015, ApJ, 802, 48

Lidman C., Suherli J., Muzzin A., et al. 2012, MNRAS, 427, 550

Lidman C., Iacobuta G., Bauer A. E, et al. 2013, MNRAS, 433, 835

Lin H., Flaugher B. & The Dark Energy Survey Collaboration. 2009, BAAS, 41, 669

Lin Y., Brodwin M., Gonzalez A., Bode P. et al. 2013, ApJ, 771, 61

Li C., White S. D. M. 2009, MNRAS, 398, 4, 2177

LSST Science Collaborations et al., 2009, preprint (arXiv:0912.0201)

Majewski S., Munn J.; Hawley S., 1996, ApJ, 459, 73

Majewski S., Munn J.; Hawley S., 1996, ApJ, 459, 73

Majewski S.; Skrutskie M., Weinberg, M, Ostheimer, James C., 2003, MNRAS, 599, 1082

Maraston C., et al., 2013, MNRAS, 435, 2764

Martinez-Delgado D., Gabany R. J., Crawford K. et al. 2010, AJ, 140, 962

Martinez-Delgado D., Romanowsky A., Gabany J., Annibali F., et al. 2012, ApJ, 748, 24.

Martinez-Delgado D., D'Onghia E., Chonis T., Beaton R. et al. 2015, AJ, 150, 116.

Malin D.F., Carter D., 1983, ApJ, 274, 534

McCarthy I., Font A., Crain R. et al. 2012, MNRAS, 420, 2245

McConnachie A., Irwin M., Ibata R. et al. Nature, 461, 66

McGrath E. J., Stockton A., Canalizo G., Iye M., Maihara T., 2008, ApJ, 682, 303

McMillan P.J. 2011, MNRAS, 414, 2446

Meert A., Vikram V., Bernardi M., 2013, MNRAS, 433, 1344

Meert A., Vikram V., Bernardi M., 2015, MNRAS, 446, 3943

Mendel, J. T., Simard L., Palmer M., Ellison S.L., Patton D.R., 2014, ApJS, 210,3

Mihos J. C., Harding P., Feldmeier J., Morrison H. 2005, ApJL, 631, L41

Monachesi A., Bell E. F., Radburn-Smith D. J., Vlajić et al. 2013, MNRAS, 766, 106

Monachesi A., Bell E. F., Radburn-Smith D. J. et al. 2015, arXiv:1507.06657

Mosleh M., Williams R., Franx, M., 2013, ApJ, 777, 117

Moster B., Somerville R. S., Maulbetsch C., et al. 2010, ApJ, 710, 903

Moster B. P., Naab T., White S.D.M., 2013, 428, 3121

Moustakas J. et al., 2013, ApJ, 767, 50

Naab T., Khockfar S., Burket A., 2006, ApJ, 636, 81

Naab T., Johansson P., Ostriker J., Efstathiou G., 2007, ApJ, 658, 710

Naab T., Johansson P., Ostriker J., 2009, ApJ, 699, 178

Navarro-Gonzalez J., Ricciardelli E., Quilis V., Vazdekis A., 2013, MNRAS, 436, 3507

Newberg H., Yanny B., 2006, JPhCS, 47, 195

Oser L., Ostriker J. P., Naab T., Johansson P. H., Burkert A., 2010, ApJ, 725, 2312

Pastorello N., Forbes D., Usher C. et al. 2015, MNRAS, 451, 2625

Patel S., van Dokkum P., Franx M. et al. 2013, ApJ, 766, 15

Peng C. Y., Ho L. C., Impey C. D., & Rix, H.-W. 2010, AJ, 139, 2097

Pillepich A., Vogelsberger M., Deason A. et al. , 2014, MNRAS, 444, 237

Pohlen M., Trujillo I., 2006, A&A, 454, 749

Preston G., Beers T.; Shectman S., 1994, AJ, 108, 538

Purcell C. W., Bullock J. S., Zentner A. R. 2007, ApJ, 666, 20

Purcell C. W.; Bullock J. S.; Kazantzidis S., 2010, MNRAS, 404, 1711

Radburn-Smith D. J., de Jong R. S., Seth A. C., Bailin J. et al. 2011, ApJS, 195, 18

Ratnatunga K., Freeman K., 1985, ApJ, 291, 260

Rejkuba M., Harris W., Greggio L. et al. 2014, ApJ, 791, 2

Rodgers A., Harding P., Sadler E., 1981, ApJ, 244, 912

Rodgers A., Paltoglou G., 1984, ApJ, 283, 5

Sales L.V., Navarro J.F., Abadi M.G., Steinmetz M., 2007, MNRAS, 379, 1464

Sandin C. 2014, A& A,567, 97

Schaye J., Crain R., Bower R., Furlong M. et al. 2014, MNRAS, 446, 521

Schlegel D. J., Finkbeiner D. P., & Davis M. 1998, ApJ, 500, 525

Schweizer F., 1980, ApJ, 237, 303

Schweizer F., Seitzer P., 1992, AJ, 104, 1039

Searle L., Zinn R., 1978, 225, 357

Sérsic J. L. 1968, Atlas de Galaxias Australes (Cordoba: Observatorio Astronomico, Univ.
  Cordoba)

Sesar B., Juri M., Ivezi . 2011, ApJ, 2011, 731, 4

Simard L., Mendel J. T., Patton D. R. et al. 2011, ApJS, 196, 11

Springel V., 2010, MNRAS, 401, 791

Sommer-Larsen J., Christensen, P., 1987, MNRAS, 225, 499

Snyder G., Torrey P., Lotz J., Genel S. et al., 2015, MNRAS, 454, 1886

Strateva I., Ivezić Ž., Knapp G. R. 2001, AJ, 122, 1861

Suh H., Jeong H., Oh K. et al. 2010, ApJS, 187, 374

Tal T., & van Dokkum P. G. 2011, ApJ, 731, 89

Tal T., van Dokkum P. G., Nelan J. and Bezanson R. 2009, AJ, 138, 1417

Tortora C., Napolitano N. R., Cardone V. F., Capaccioli M., Jetzer Ph., Molinaro, R.
  2010, MNRAS, 407, 144

Trujillo I., Forster Schreiber N., Rudnick G., et al. 2006, ApJ, 650, 18

Trujillo I., Fliri J., arXiv:1510.04696

van Dokkum P., Whitaker K., Brammer G. et al. 2010, ApJ, 709, 1018

van Dokkum P. G., Abraham R., Merritt A. 2014, ApJL, 782, 24

Velazquez H., White S.D.M., 1995, MNRAS, 275, 23

Vogelsberger M., Genel S., Springel V. et al. 2014, MNRAS, 444, 1518

Von Der Linden A., Best P.N., Kauffmann G., White S.D.M., 2007, MNRAS, 379, 867

Vulcani B., Marchesini D., De Lucia G., et al. 2016, ApJ, 816, 86

Wang W., & White S. D. M. 2012, MNRAS, 424, 2574

Watkins L., Evans N. W., Belokurov V. et al. 2009, MNRAS, 398, 1757

White S.D.M., Rees M., 1978, MNRAS, 183, 341

Yang X., van den Bosch F. C., Mo H., et al. 2006, ApJ, 369, 1293

Yang X., Mo H. J., van den Bosch F. C., et al. 2007, ApJ, 671, 153

Yoon I., Weinberg M. D., Katz N. 2011, MNRAS, 414, 1625

Zibetti S., White S. D. M., & Brinkmann J. 2004, MNRAS, 347, 556

Zibetti S., White S. D. M., Schneider D. P., & Brinkmann J. 2005, MNRAS, 358, 949

Zhang Y., Miller C., McKay T., Rooney P. et al. 2016, ApJ, 816, 98

Acknowledgments

Many people have contributed to the success of this thesis. First and foremost, I would like to thank my supervisor Guinevere Kauffmann for introducing me to the topic of stellar haloes and for her guidance and patience in helping me through this thesis. I have learned a lot from her during these last three and a half years and am eternally grateful.

A special thanks to Simona Vegetti for being a good friend and for helping me often to sharpen my thoughts with regards to this thesis. I also would like to thank Jing Wang for guiding me through the initial steps of working with the photometry of galaxies. I also would like to thank Facundo Gomez and Antonela Monachesi for the great discussions on the topics of stellar haloes of galaxies. A special thanks to all the other postdocs here at MPA with whom I have interacted with, and who enriched me. I would also like to thank all the Directors and staff members of MPA for giving me the opportunity of working here.

I would also like to especially like to thank the secretaries of MPA, Maria Depner, Gabriele Kratschmann, Cornelia Rickl, Sonja Gruendl and Stella Veith for their ever ready willingness to lend a helping hand and their encouragement during my PhD. A special thanks to all in the Computer IT department, Bernt Christandl, Hans-Werner Paulsen and Andreas Weiss, without whose technical support, this work could not be accomplished.

I would like to thank Monika Soraisam, Nitya Harihan and Mei-Ling Huang for the good and lovely conversations we had during lunch. I would also like to thank all my friends who made my stay in Munich very enjoyable: Xun, Ines, Antonella and many others. A special thanks to Hannah Übler for helping me in translating the abstract of this thesis into German, as well as many "sermons" during my last three years here.

I would like to thank the English speaking Catholic community at the Kaulbachstrasse for making me feel at home here in Munich, and for grounding me in "reality".

A special thanks to the Jesuit community of "Berchmans Kolleg" and for their support during the years of the PhD. A special thanks especially to Carlos Ming, Devi Astudillo, Giampiero Basille and Michael Hainz among others. I would like to thank the Jesuits of the Vatican Observatory for their constant support and guidance.

Finally, I would like to thank my parents for the love, patience and understanding, and for always being there for me.